

INVESTIGATING FEEDBACK AND RELAXATION IN CLUSTERS OF
GALAXIES WITH THE CHANDRA X-RAY OBSERVATORY

By

Kenneth W. Cavagnolo

AN ABSTRACT OF A DISSERTATION

Submitted to
Michigan State University
in partial fulfillment of the requirements
for the degree of

DOCTOR OF PHILOSOPHY

Department of Physics and Astronomy

2008

Dr. Megan Donahue

ABSTRACT

INVESTIGATING FEEDBACK AND RELAXATION IN CLUSTERS OF GALAXIES WITH THE CHANDRA X-RAY OBSERVATORY

By

Kenneth W. Cavagnolo

Presented in this dissertation is an analysis of the X-ray emission from the intracluster medium (ICM) in clusters of galaxies observed with the *Chandra* X-ray Observatory. More specifically, cluster dynamic state is investigated via ICM temperature inhomogeneity, and ICM entropy is used to study physics of cluster cores.

If the hot ICM is nearly isothermal in the projected region of interest, the X-ray temperature inferred from a broadband (0.7-7.0 keV) spectrum should be identical to the X-ray temperature inferred from a hard-band (2.0-7.0 keV) spectrum. However, if unresolved cool lumps of gas are contributing soft X-ray emission, the temperature of a best-fit single-component thermal model will be cooler for the broadband spectrum than for the hard-band spectrum. Using this difference as a diagnostic, the ratio of best-fitting hard-band and broadband temperatures may indicate the presence of cooler gas even when the X-ray spectrum itself may not have sufficient signal-to-noise ratio (S/N) to resolve multiple temperature components.

In Chapter 2 we explore this band dependence of the inferred X-ray temperature of the ICM for 192 well-observed galaxy clusters selected from the *Chandra* X-ray Observatory's Data Archive. To test if band dependency is a diagnostic of cluster dynamic state, we extract X-ray spectra from core-excised annular regions for each cluster in the archival sample. We compare the X-ray temperatures inferred from single-temperature fits when the energy range of the fit is 0.7-7.0 keV (broad) and when the energy range is 2.0/(1+ z)-7.0 keV (hard). We find that the hard-band

Kenneth W. Cavagnolo

temperature is significantly higher, on average, than the broadband temperature. On further exploration, we find this temperature ratio is enhanced preferentially for clusters which are known merging systems. In addition, cool-core clusters tend to have best-fit hard-band temperatures that are in closer agreement with their best-fit broadband temperatures.

ICM Entropy is of great interest because it dictates ICM global properties and records the thermal history of a cluster. Entropy is therefore a useful quantity for studying the effects of feedback on the cluster environment and investigating the breakdown of cluster self-similarity. Radial entropy profiles of the ICM for a collection of 233 clusters taken from the *Chandra* X-ray Observatory's Data Archive are presented in Chapter 3. We find that most ICM entropy profiles are well-fit by a model which is a power-law at large radii and approaches a constant value at small radii: $K(r) = K_0 + K_{100}(r/100 \text{ kpc})^\alpha$, where K_0 quantifies the typical excess of core entropy above the best fitting power-law found at larger radii. We also show that the K_0 distributions of both the full archival sample and the primary *HIFLUGCS* sample of Reiprich (2001) are bimodal with a distinct gap beginning at $K_0 \approx 30 \text{ keV cm}^2$ and population peaks at $K_0 \sim 15 \text{ keV cm}^2$ and $K_0 \sim 150 \text{ keV cm}^2$. ~~All data, and results associated with this project have been made publicly available via a project web site.~~



Utilizing the results of the the *Chandra* X-ray Observatory archival study of intracluster entropy presented in Chapter 3, we show in Chapter 4 that H α and radio emission from the brightest cluster galaxy are much more pronounced when the cluster's core gas entropy is $\lesssim 30 \text{ keV cm}^2$. The prevalence of H α emission below this threshold indicates that it marks a dichotomy between clusters that can harbor multiphase gas and star formation in their cores and those that cannot. The fact that strong central radio emission also appears below this boundary suggests that active galactic nuclei feedback turns on when the ICM starts to condense, strengthening the

Kenneth W. Cavagnolo

case for AGN feedback as the mechanism that limits star formation in the Universe's most luminous galaxies.

This is to certify that the
dissertation entitled

Investigating Feedback and Relaxation in Clusters of Galaxies with the Chandra X-ray Observatory

presented by

Kenneth W. Cavagnolo

has been accepted towards fulfillment
of the requirements for the

Ph.D. degree in Astronomy & Astrophysics

Major Professor's Signature

Date

INVESTIGATING FEEDBACK AND RELAXATION IN CLUSTERS OF
GALAXIES WITH THE CHANDRA X-RAY OBSERVATORY

By

Kenneth W. Cavagnolo

AN ABSTRACT OF A DISSERTATION

Submitted to
Michigan State University
in partial fulfillment of the requirements
for the degree of

DOCTOR OF PHILOSOPHY

Department of Physics and Astronomy

2008

Dr. Megan Donahue

ABSTRACT



INVESTIGATING FEEDBACK AND RELAXATION IN CLUSTERS OF
GALAXIES WITH THE CHANDRA X-RAY OBSERVATORY

By

Kenneth W. Cavagnolo

Presented in this dissertation is an analysis of the X-ray emission from the intracluster medium (ICM) in clusters of galaxies observed with the *Chandra* X-ray Observatory. More specifically, cluster dynamic state is investigated via ICM temperature inhomogeneity, and ICM entropy is used to study physics of cluster cores.

If the hot ICM is nearly isothermal in the projected region of interest, the X-ray temperature inferred from a broadband (0.7-7.0 keV) spectrum should be identical to the X-ray temperature inferred from a hard-band (2.0-7.0 keV) spectrum. However, if unresolved cool lumps of gas are contributing soft X-ray emission, the temperature of a best-fit single-component thermal model will be cooler for the broadband spectrum than for the hard-band spectrum. Using this difference as a diagnostic, the ratio of best-fitting hard-band and broadband temperatures may indicate the presence of cooler gas even when the X-ray spectrum itself may not have sufficient signal-to-noise ratio (S/N) to resolve multiple temperature components.

In Chapter 2 we explore this band dependence of the inferred X-ray temperature of the ICM for 192 well-observed galaxy clusters selected from the *Chandra* X-ray Observatory's Data Archive. To test if band dependency is a diagnostic of cluster dynamic state, we extract X-ray spectra from core-excised annular regions for each cluster in the archival sample. We compare the X-ray temperatures inferred from single-temperature fits when the energy range of the fit is 0.7-7.0 keV (broad) and when the energy range is 2.0/(1+ z)-7.0 keV (hard). We find that the hard-band

Kenneth W. Cavagnolo

temperature is significantly higher, on average, than the broadband temperature. On further exploration, we find this temperature ratio is enhanced preferentially for clusters which are known merging systems. In addition, cool-core clusters tend to have best-fit hard-band temperatures that are in closer agreement with their best-fit broadband temperatures.

ICM Entropy is of great interest because it dictates ICM global properties and records the thermal history of a cluster. Entropy is therefore a useful quantity for studying the effects of feedback on the cluster environment and investigating the breakdown of cluster self-similarity. Radial entropy profiles of the ICM for a collection of 233 clusters taken from the *Chandra* X-ray Observatory's Data Archive are presented in Chapter 3. We find that most ICM entropy profiles are well-fit by a model which is a power-law at large radii and approaches a constant value at small radii: $K(r) = K_0 + K_{100}(r/100 \text{ kpc})^\alpha$, where K_0 quantifies the typical excess of core entropy above the best fitting power-law found at larger radii. We also show that the K_0 distributions of both the full archival sample and the primary *HIFLUGCS* sample of Reiprich (2001) are bimodal with a distinct gap beginning at $K_0 \approx 30 \text{ keV cm}^2$ and population peaks at $K_0 \sim 15 \text{ keV cm}^2$ and $K_0 \sim 150 \text{ keV cm}^2$. All data, and results associated with this project have been made publicly available via a project web site.

Utilizing the results of the the *Chandra* X-ray Observatory archival study of intracluster entropy presented in Chapter 3, we show in Chapter 4 that H α and radio emission from the brightest cluster galaxy are much more pronounced when the cluster's core gas entropy is $\lesssim 30 \text{ keV cm}^2$. The prevalence of H α emission below this threshold indicates that it marks a dichotomy between clusters that can harbor multiphase gas and star formation in their cores and those that cannot. The fact that strong central radio emission also appears below this boundary suggests that active galactic nuclei feedback turns on when the ICM starts to condense, strengthening the

Kenneth W. Cavagnolo
case for AGN feedback as the mechanism that limits star formation in the Universe's
most luminous galaxies.



INVESTIGATING FEEDBACK AND RELAXATION IN CLUSTERS OF
GALAXIES WITH THE CHANDRA X-RAY OBSERVATORY

By

Kenneth W. Cavagnolo

A DISSERTATION

Submitted to
Michigan State University
in partial fulfillment of the requirements
for the degree of

DOCTOR OF PHILOSOPHY

Department of Physics and Astronomy

2008

ABSTRACT



INVESTIGATING FEEDBACK AND RELAXATION IN CLUSTERS OF
GALAXIES WITH THE CHANDRA X-RAY OBSERVATORY

By

Kenneth W. Cavagnolo

Presented in this dissertation is an analysis of the X-ray emission from the intracluster medium (ICM) in clusters of galaxies observed with the *Chandra* X-ray Observatory. More specifically, cluster dynamic state is investigated via ICM temperature inhomogeneity, and ICM entropy is used to study physics of cluster cores.

If the hot ICM is nearly isothermal in the projected region of interest, the X-ray temperature inferred from a broadband (0.7-7.0 keV) spectrum should be identical to the X-ray temperature inferred from a hard-band (2.0-7.0 keV) spectrum. However, if unresolved cool lumps of gas are contributing soft X-ray emission, the temperature of a best-fit single-component thermal model will be cooler for the broadband spectrum than for the hard-band spectrum. Using this difference as a diagnostic, the ratio of best-fitting hard-band and broadband temperatures may indicate the presence of cooler gas even when the X-ray spectrum itself may not have sufficient signal-to-noise ratio (S/N) to resolve multiple temperature components.

In Chapter 2 we explore this band dependence of the inferred X-ray temperature of the ICM for 192 well-observed galaxy clusters selected from the *Chandra* X-ray Observatory's Data Archive. To test if band dependency is a diagnostic of cluster dynamic state, we extract X-ray spectra from core-excised annular regions for each cluster in the archival sample. We compare the X-ray temperatures inferred from single-temperature fits when the energy range of the fit is 0.7-7.0 keV (broad) and when the energy range is 2.0/(1+ z)-7.0 keV (hard). We find that the hard-band

temperature is significantly higher, on average, than the broadband temperature. On further exploration, we find this temperature ratio is enhanced preferentially for clusters which are known merging systems. In addition, cool-core clusters tend to have best-fit hard-band temperatures that are in closer agreement with their best-fit broadband temperatures.

ICM Entropy is of great interest because it dictates ICM global properties and records the thermal history of a cluster. Entropy is therefore a useful quantity for studying the effects of feedback on the cluster environment and investigating the breakdown of cluster self-similarity. Radial entropy profiles of the ICM for a collection of 233 clusters taken from the *Chandra* X-ray Observatory's Data Archive are presented in Chapter 3. We find that most ICM entropy profiles are well-fit by a model which is a power-law at large radii and approaches a constant value at small radii: $K(r) = K_0 + K_{100}(r/100 \text{ kpc})^\alpha$, where K_0 quantifies the typical excess of core entropy above the best fitting power-law found at larger radii. We also show that the K_0 distributions of both the full archival sample and the primary *HIFLUGCS* sample of Reiprich (2001) are bimodal with a distinct gap beginning at $K_0 \approx 30 \text{ keV cm}^2$ and population peaks at $K_0 \sim 15 \text{ keV cm}^2$ and $K_0 \sim 150 \text{ keV cm}^2$. All data, and results associated with this project have been made publicly available via a project web site.

Utilizing the results of the the *Chandra* X-ray Observatory archival study of intracluster entropy presented in Chapter 3, we show in Chapter 4 that H α and radio emission from the brightest cluster galaxy are much more pronounced when the cluster's core gas entropy is $\lesssim 30 \text{ keV cm}^2$. The prevalence of H α emission below this threshold indicates that it marks a dichotomy between clusters that can harbor multiphase gas and star formation in their cores and those that cannot. The fact that strong central radio emission also appears below this boundary suggests that active galactic nuclei feedback turns on when the ICM starts to condense, strengthening the

case for AGN feedback as the mechanism that limits star formation in the Universe's most luminous galaxies.

Copyright by
KENNETH W. CAVAGNOLO
2008

Dedicated to my mother: Miss Lorna Lorraine Cox.

ACKNOWLEDGMENTS

Thanks to Christopher Waters for the LATEX class used to format this thesis.

My deepest thanks to Megan Donahue and Mark Voit for their guidance, wisdom, patience, and without whom I would be in quantum computing. I can only say, “Thank you, Megan” for giving me the time and space to find my bearings after my mother’s passing, words are insufficient to express my gratitude. Ming Sun always listened, always had time for a question, and was never wrong. Jack Baldwin nurtured my painfully slow development as a research assistant, a more calming voice there has never been. On behalf of everyone that has never said so, “We love you, Shawna Prater. MSU Astronomy and Astrophysics cannot do business without you.” And of course, Debbie Simmons, without whom I would have been dropped from all courses and locked out of the building.

Many dissertations across many disciplines acknowledge many religious figures and a multitude of gods; but what about the Sun? Every time I feel the startling warmth of the Sun on my skin, it is an invigorating experience. To be bathed in photons millions of years old from an inconceivably large nuclear power plant over a hundred million kilometers away makes me feel connected to the Universe in a way that is surreal. To feel purposely cared for by an absentee whom’s existance and operation are fundamentally devoid of purpose is quite profound. Unknowingly, the Sun gave rise to a species of sentient dissadents. For that I say, “Thank you, Sun!”

To my wife: Our vows were fortelling, I will indeed require the course of an entire life to express my appreciation for the tenderness, care, love, and humor you gave during completion of this dissertation. You are, and always will be, my beloved.

PREFACE

Our Universe is predominantly an untold story. Within a larger, nested framework of complex mechanisms, humans evolved with minimal impact on the systems which support and nurture our existence. Yet, during the short era of global industrialization, we have compromised the effectiveness and function of the systems which formed the biodiversity which makes our planet such a wonderful place. As an acknowledgement of the appreciation our species has for the Earth, and as a show of our understanding for humanity's fleeting presence in the Earth's lifecycle, let us strive to utilize the pursuit of knowledge, through application of reason and logic, so that our actions benefit "all the children, of all species, for all of time" (McDonough & Braungart, 2002). Let us all exert effort such that the Earth and the Universe will be enriched by humanity, and that our actions – local, global, and possibly interplanetary – will leave the places we inhabit and visit nourished from our presence.

TABLE OF CONTENTS

List of Tables.....	xi
List of Figures.....	xii
List of Symbols.....	xiv
1 Introduction.....	1
1.1 Clusters of Galaxies	1
1.2 The Intracluster Medium	6
1.2.1 X-ray Emission	8
1.2.2 Entropy	14
1.3 The Incomplete Picture of Clusters	16
1.3.1 Breaking of Self-Similarity	16
1.3.2 The Cooling Flow Problem	20
1.4 Chandra X-Ray Observatory	26
1.4.1 Telescope and Instruments	26
1.4.2 X-ray Background and Calibration	31
2 Bandpass Dependence of X-ray Temperatures in Galaxy Clusters .	36
2.1 Introduction	36
2.2 Sample Selection	39
2.3 <i>Chandra</i> Data	42
2.3.1 Reprocessing and Reduction	42
2.3.2 X-ray Background	44
2.4 Spectral Extraction	47
2.5 Spectral Analysis	48
2.5.1 Fitting	48
2.5.2 Simulated Spectra	50
2.6 Results and Discussion	54
2.6.1 Temperature Ratios	54
2.6.2 Systematics	55
2.6.3 Using T_{HBR} as a Test of Relaxation	62
2.7 Summary and Conclusions	68
2.8 Acknowledgments	70
3 Intracluster Medium Entropy Profiles For A Chandra Archival Sample of Galaxy Clusters.....	73
3.1 Introduction	73
3.2 Data Collection	78
3.3 Data Analysis	80
3.3.1 Temperature Profiles	81

3.3.2	Deprojected Electron Density Profiles	84
3.3.3	β -model Fits	85
3.3.4	Entropy Profiles	86
3.3.5	Exclusion of Central Sources	90
3.4	Systematics	92
3.4.1	PSF Effects	92
3.4.2	Angular Resolution Effects	94
3.4.3	Profile Curvature and Number of Bins	96
3.4.4	Power-law Profiles	97
3.5	Results and Discussion	100
3.5.1	Non-Zero Core Entropy	101
3.5.2	Bimodality of Core Entropy Distribution	103
3.5.3	The <i>HIFLUGCS</i> Sub-Sample	106
3.5.4	Distribution of Core Cooling Times	108
3.5.5	Slope and Normalization of Power-law Components	114
3.6	Summary and Conclusions	114
3.7	Acknowledgements	117
3.8	Supplemental Cluster Notes	117
4	An Entropy Threshold for Strong Hα and Radio Emission in the Cores of Galaxy Clusters	124
4.1	Introduction	124
4.2	Data Analysis	126
4.2.1	X-ray	126
4.2.2	H α	127
4.2.3	Radio	128
4.3	H α Emission and Central Entropy	130
4.4	Radio Sources and Central Entropy	131
4.5	Summary	135
4.6	Acknowledgements	135
5	Summary	136
5.1	Energy Band Dependence of X-ray Temperatures	136
5.2	Chandra Archival Sample of Intracluster Entropy Profiles	137
5.3	An Entropy Threshold for Strong H α and Radio Emission in the Cores of Galaxy Clusters	139
	References	142

LIST OF TABLES

2.1	Summary of two-component simulations	54
2.2	Weighted averages for various apertures	55

LIST OF FIGURES

1.1 <i>Hubble</i> image of Abell 1689	2
1.2 Composite image of the Bullet Cluster	4
1.3 Synthetic spectral model of $kT_X = 2.0$ keV gas.	11
1.4 Synthetic spectral model of $kT_X = 8.0$ keV gas.	11
1.5 Figures illustrating of large scale structure formation.	18
1.6 <i>Chandra</i> X-ray Observatory spacecraft.	27
1.7 ACIS focal plane during observation.	29
1.8 Spectrum of Abell 1795.	30
1.9 <i>Chandra</i> effective area as a function of energy.	33
2.1 Redshift distribution of bolometric luminosities for T_{HBR} sample	41
2.2 Histogram of hard-particle count rate ratios for T_{HBR} sample	46
2.3 T_{HBR} vs. broadband temperature for T_{HBR} sample	56
2.4 Plot of several possible systematics for $R_{2500\text{--CORE}}$ apertures.	59
2.5 Plot of several possible systematics for $R_{5000\text{--CORE}}$ apertures.	60
2.6 T_{HBR} vs. best-fit metallicity	61
2.7 Number of cool and non-cool clusters as a function of T_{HBR}	64
2.8 Plot of T_{HBR} vs. broadband temperatures color-coded for different cluster types	67
3.1 Ratio of best-fit K_0 for temperature interpolation schemes.	88
3.2 Best-fit K_0 versus redshift.	95
3.3 Best-fit K_0 versus average curvature, κ_A	98

3.4	Best-fit K_0 versus number of fit bins.	98
3.5	Montage of entropy profiles for varying cuts in cluster temperature. . . .	102
3.6	Histogram and cumulative distribution of best-fit K_0 for full <i>ACCEPT</i> sample.	104
3.7	Histogram and cumulative distribution of best-fit K_0 for primary <i>HIFLUGCS</i> sample.	109
3.8	Best-fit K_0 versus average cluster temperature for the <i>HIFLUGCS</i> sample.	110
3.9	Histograms and cumulative distributions of cooling times.	113
3.10	Surface brightness profiles and best-fit β -models.	118
4.1	$\text{H}\alpha$ luminosity versus core entropy	132
4.2	BCG radio power versus core entropy	134

Images in this dissertation are presented in color.

LIST OF SYMBOLS

	Mpc Megaparsec: A unit of length representing one million parsecs. The parsec (pc) is a historical unit for measuring parallax and equals 30.857×10^{12} km.	1
<i>z</i>	Dimensionless redshift: As is common in most of astronomy, I adopt the definition of redshift using a dimensionless ratio of wavelengths, $z = (\lambda_{\text{observed}}/\lambda_{\text{rest}}) - 1$, where the wavelength shift occurs because of cosmic expansion.	1
H_0	Hubble constant: The current ratio of recessional velocity arising from expansion of the Universe to an object's distance from the observer, $v = H_0 D$. H_0 is currently measured to be $\sim 70 \text{ km s}^{-1} \text{ Mpc}^{-1}$. Inverted, the Hubble constant yields the present age of the Universe, $H_0^{-1} \approx 13.7$ billion years. $H(z)$ denotes the Hubble constant at a particular redshift, z .	1
ρ_c	Critical density: The density necessary for a universe which has spatially flat geometry and in which the expansion rate of spacetime balances gravitational attraction and prevents recollapse. In terms of relevant quantities $\rho_c = 3H(z)^2/8\pi G$, with units g cm^{-3} .	1
Ω_Λ	Cosmological constant energy density of the Universe: The ratio of energy density due to a cosmological constant to the critical density. Ω_Λ is currently measured to be ~ 0.7 .	1
Ω_M	Matter density of the Universe: The ratio of total matter density to the critical density. Ω_M is currently measured to be ~ 0.3 .	1
M_\odot	Mass of the Sun: One solar mass equals $1.9891 \times 10^{30} \text{ kg}$	3
Z_\odot	Metal abundance of the Sun: Individual elemental abundances can be found in Anders & Grevesse (1989).	9
N_H	Neutral hydrogen column density: The Galaxy is rich with neutral hydrogen which absorbs incoming extragalactic radiation. Photoelectric absorption models are used to quantify the attenuation, and typically take as input the column density (cm^{-2}) of neutral hydrogen in a particular direction. N_H is related to the number density, n_H (cm^{-3}), along the line of sight, dl , as $N_H = \int n_H dl$.	11

Λ	Cooling function: A function describing plasma emissivity for a given temperature and metal composition, and typically given in units of ergs cm ³ s ⁻¹	13
D_C	Comoving distance: The distance which would be measured between two objects today if those two points were moving away from each other with the expansion of the Universe.	17
D_A	Angular diameter distance: The ratio of an object's true transverse size to its angular size. For a nearly flat universe, D_A is a good approximation of the comoving distance, $D_A \approx D_C/(1+z)$	17
Ω_S	Solid angle: For a sphere of a given radius, for example the distance to an object D_C , the area of that object, A , on the sphere subtends an angle equal to $\Omega_S = A/D_C^2$. This is the solid angle.	17
V_C	Comoving volume: The volume in which the number density of slowly evolving objects locked into the local Hubble flow, like galaxy clusters, is constant with redshift. For a redshift elements dz and solid angle $d\Omega_S$ the comoving volume element is $dV_C = \frac{D_C[D_A(1+z)]^2}{\sqrt{\Omega_M(1+z)^3 + \Omega_k(1+z)^2 + \Omega_\Lambda}} d\Omega_S dz$ where Ω_k is curvature and is ≈ 0	17
T_{HBR}	Hard-band to broadband ratio: The ratio of temperatures in the energy bands 2.0-7.0 keV and 0.7-7.0 keV.	38

CHAPTER 1:

INTRODUCTION

1.1 CLUSTERS OF GALAXIES

Of the luminous matter in the Universe, stars and galaxies are often the most familiar to a sky gazer. Aside from the Moon and the occasional bright planet, stars are the most abundantly obvious patrons of the night sky. Viewed from a sufficiently dark location, the stars form a band of light interspersed with dust and gaseous clouds which define the Milky Way, our home galaxy. The Milky Way is only one of more than 30 galaxies in a gravitationally bound group of galaxies, named the Local Group, which includes the well-known, nearby galaxy Andromeda. But in cosmological terms, the Local Group is very small in comparison to immense structures containing thousands of galaxies. In a turn of wit, these structures are appropriately named clusters of galaxies, and are the focus of this dissertation.

Galaxy clusters are the most massive gravitationally bound structures to have yet formed in the Universe. As where galaxy groups have roughly 10-50 galaxies, galaxy clusters have hundreds to thousands of galaxies. When viewed through a telescope, a galaxy cluster appears as a tight distribution of mostly elliptical and S0 spiral galaxies within a radius of $\sim 1 - 5$ Mpc¹ of each other. Rich galaxy clusters are truly spectacular objects, as can be seen in Figure 1.1 which shows the *Hubble* Space Telescope's close-up of the strong lensing cluster Abell 1689.

¹Throughout this dissertation, a flat Λ CDM cosmology of $H_0 = 70 \text{ km s}^{-1} \text{ Mpc}^{-1}$, $\Omega_\Lambda = 0.7$, and $\Omega_M = 0.3$ is assumed. These values are taken from Spergel et al. (2007).

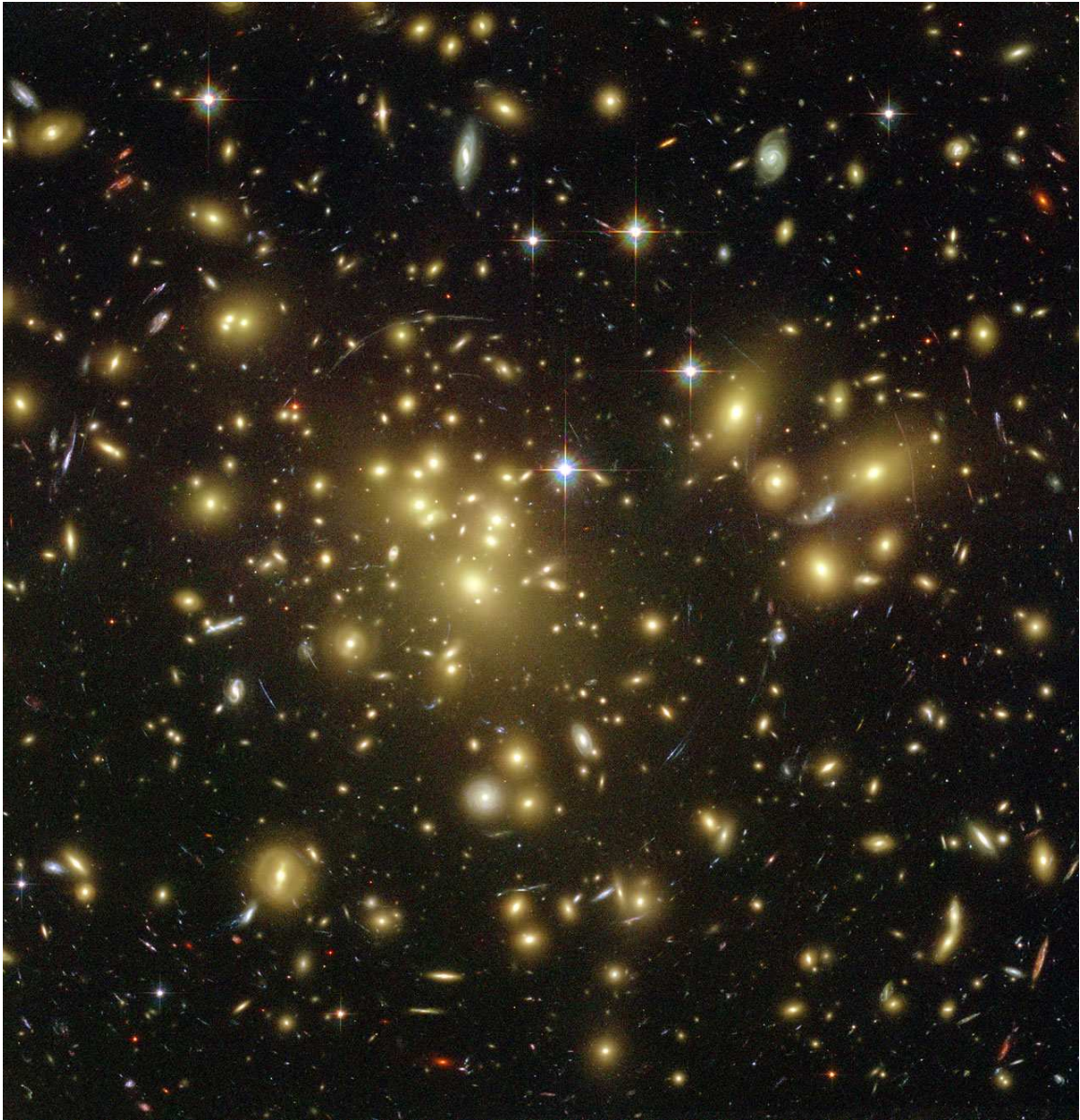


Figure 1.1 Optical image of the galaxy cluster Abell 1689 as observed with the ACS instrument on-board the *Hubble* Space Telescope. The fuzzy yellowish spheres are giant elliptical (gE) galaxies in the cluster, with the gE nearest the center of the image being the brightest cluster galaxy – ostensibly, the cluster “center”. Image taken from NASA’s Hubblesite.org. Image Credits: NASA, N. Benitez (JHU), T. Broadhurst (The Hebrew University), H. Ford (JHU), M. Clampin(STScI), G. Hartig (STScI), G. Illingworth (UCO/Lick Observatory), the ACS Science Team and ESA.

Galaxy clusters are deceptively named. As with most objects in the Universe, one of the most revealing characteristics of an object is its mass, and the mass of clusters of galaxies are not dominated by galaxies. With the proper vision, an observer would find clusters are dominated ($\gtrsim 70\%$) by dark matter with most ($\gtrsim 80\%$) of the baryonic mass² in the form of a hot ($kT \approx 2 - 15$ keV; 10-100 million degrees K), luminous (10^{43-46} ergs s $^{-1}$), diffuse ($10^{-1} - 10^{-4}$ cm $^{-3}$) intracluster medium (ICM) which is co-spatial with the galaxies but dwarfs them in mass (Blumenthal et al., 1984; David et al., 1990). For comparison, the ICM in the core region of a galaxy cluster is, on average, 10^{20} times less dense than typical Earth air, 10^5 times denser than the mean cosmic density, more than 2000 times hotter than the surface of the Sun, and shines as bright as 10^{35} 100 watt light bulbs.

Because of the ICM’s extreme temperature, the gas is mostly ionized, making it a plasma. For the temperature range of clusters, the ICM is most luminous at X-ray wavelengths of the electromagnetic spectrum. This makes observing galaxy clusters with X-ray telescopes, like NASA’s *Chandra* X-ray Observatory, a natural choice. Clusters have masses ranging over 10^{14-15} M $_{\odot}$ with velocity dispersions of $500 - 1500$ km s $^{-1}$. The ICM has also been enriched with metals³ to an average value of ~ 0.3 solar abundance. Shown in Figure 1.2 is an optical, X-ray, and gravitational lensing composite image of the galaxy cluster 1E0657-56. This cluster is undergoing an especially spectacular and rare merger in the plane of the sky which allows for the separate dominant components of a cluster – dark matter, the ICM, and galaxies – to be “seen” distinctly.

Knowing the characteristics of galaxy clusters is a small part of the discovery process, we must also wonder, why study clusters of galaxies? Galaxy clusters have two very important roles in the current research paradigm:

²Baryonic is a convenient term used to describe ordinary matter like atoms or molecules, while non-baryonic matter is more exotic like free electrons or dark matter particles.

³It is common practice in astronomy to classify “metals” as any element with more than two protons.

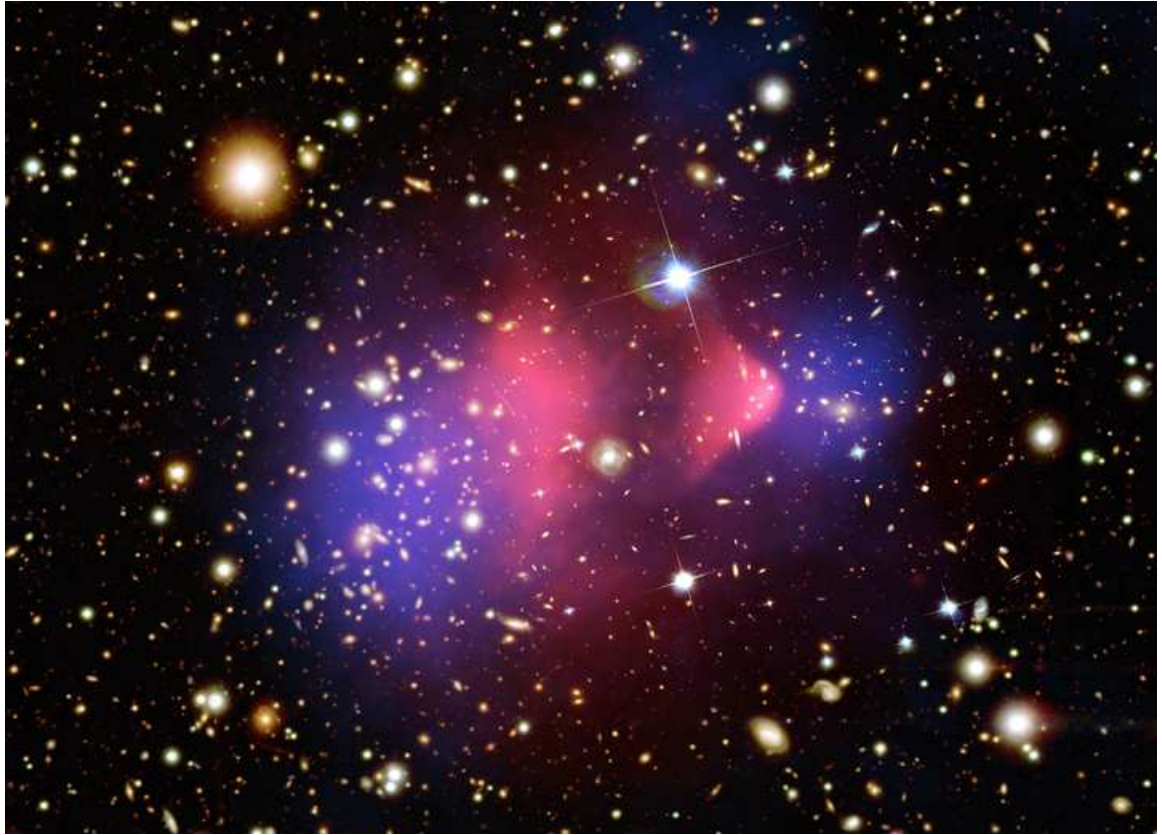


Figure 1.2 The galaxy cluster 1E0657-56, a.k.a. the Bullet Cluster. All of the primary components of a galaxy cluster can be seen in this image: the X-ray ICM (pink), dark matter (blue), and galaxies. The brilliant white object with diffraction spikes is a star. This cluster has become very famous because it is direct evidence for the existence of dark matter (Clowe et al., 2006). Image taken from NASA Press Release 06-297. Image credits: NASA/CXC/CfA/Markevitch et al. (2002) (X-ray); NASA/STScI/Magellan/U.Arizona/Clowe et al. (2006) (Optical); NASA/STScI/ESO WFI/Magellan/U.Arizona/Clowe et al. (2006) (Lensing).

1. Galaxy clusters represent a unique source of information about the Universe's underlying cosmological parameters, including the nature of dark matter and the dark energy equation of state. Large-scale structure growth is exponentially sensitive to some of these parameters, and by counting the number of clusters found in a comoving volume of space, specifically above a given mass threshold, clusters may be very useful in cosmological studies (Voit, 2005).
2. The cluster gravitational potential well is deep enough to retain all the matter which has fallen in over the age of the Universe. This slowly evolving “sealed box” therefore contains a comprehensive history of all the physical processes involved in galaxy formation and evolution, such as: stellar evolution, supernovae feedback, black hole activity in the form of active galactic nuclei, galaxy mergers, ram pressure stripping of in-falling galaxies and groups, *et cetera*. The time required for the ICM in the outskirts of a cluster to radiate away its thermal energy is longer than the age of the Universe, hence the ICM acts as a record-keeper of all the aforementioned activity. Therefore, by studying the ICM’s physical properties, the thermal history of the cluster can be partially recovered and utilized in developing a better understanding of cluster formation and evolution.

In this dissertation I touch upon both these points by studying the emergent X-ray emission of the ICM as observed with the *Chandra* X-ray Observatory.

While clusters have their specific uses in particular areas of astrophysics research, they also are interesting objects in their own right. A rich suite of physics are brought to bear when studying galaxy clusters. A full-blown, theoretical construction of a galaxy cluster requires, to name just a few: gravitation, fluid mechanics, thermodynamics, hydrodynamics, magnetohydrodynamics, and high-energy/particle/nuclear physics. Multiwavelength observations of galaxy clusters provide excellent datasets for testing the theoretical predictions from other areas of physics, and clusters are

also a unique laboratory for empirically establishing how different areas of physics interconnect. Just this aspect of clusters puts them in a special place among the objects in our Universe worth intense, time-consuming, (and sometimes expensive) scrutiny. At a minimum, galaxy clusters are most definitely worthy of being the focus of a humble dissertation from a fledgling astrophysicist.

As this is a dissertation focused around observational work, in Section §1.2 I provide a brief primer on the X-ray observable properties of clusters which are important to understanding this dissertation. Section §1.2.2 provides discussion of gas entropy, a physical property of the ICM which may be unfamiliar to many readers and is utilized heavily in Chapters 3 and 4. In Section §1.3, I more thoroughly discuss reasons for studying clusters of galaxies which are specific to this dissertation. Presented in Section §1.3.1 is discussion of why clusters of different masses are not simply scaled versions of one another, and in Section §1.3.2 the unresolved “cooling flow problem” is briefly summarized. The current chapter concludes with a brief description of the *Chandra* X-ray Observatory (CXO) and its instruments in Section §1.4. *Chandra* is the space-based telescope with which all of the data presented in this dissertation was collected.

1.2 THE INTRACLUSTER MEDIUM

In Section §1.1, the ICM was presented as a mostly ionized, hot, diffuse plasma which dominates the baryonic mass content of clusters. But where did it come from and what is the composition of this pervasive ICM? What are the mechanisms that result in the ICM’s X-ray luminescence? How do observations of the ICM get converted into physical properties of a cluster? In this section I briefly cover the answers to these questions in order to give the reader a better understanding of the ICM.

Galaxy clusters are built-up during the process of hierarchical merger of dark matter halos and the baryons gravitationally coupled to those halos (White & Rees,

1978). Owing to the inefficiency of galaxy formation and the processes of galactic mass ejection and ram pressure stripping, many of the baryons in these dark matter halos are in the form of diffuse gas and not locked up in galaxies. During the merger of dark matter halos, gravitational potential energy is converted to thermal energy and the diffuse gas is heated to the virial temperature of the cluster potential through processes like adiabatic compression and accretion shocks. The cluster virial temperature is calculated by equating the average kinetic energy of a gas particle to its thermal energy,

$$\frac{1}{2}\mu m\langle\sigma^2\rangle = \frac{3}{2}kT_{virial} \quad (1.1)$$

$$T_{virial} = \frac{\mu m\langle\sigma^2\rangle}{3k} \quad (1.2)$$

where μ is the mean molecular weight, k is the Boltzmann constant, T_{virial} is the virial temperature, m is the mass of a test particle, and $\langle\sigma\rangle$ is the average velocity of the test particle. In this equation, $\langle\sigma\rangle$ can be replaced with the line-of-sight galaxy velocity dispersion (an actual cluster observable) because all objects within the cluster potential (stars, galaxies, protons, *etc.*) are subject to the same dynamics and hence have comparable thermal and kinetic energies. The virial properties, including temperature, are fundamental characteristic of a cluster.

Galaxy clusters are the most massive objects presently in the Universe. The enormous mass means deep gravitational potential wells and hence very high virial temperatures. Most clusters lie in the temperature range $kT_{virial} = 1 - 15$ keV. At these energy scales, gases are collisionally ionized plasmas and will emit X-rays via thermal bremsstrahlung (discussed in Section §1.2.1). The ICM is not a pure ionized hydrogen gas, as a result, atomic line emission from heavy elements with bound electrons will also occur. The ICM is also optically thin at X-ray wavelengths, *e.g.* the ICM optical depth to X-rays is much smaller than unity, $\tau_\lambda \ll 1$, and hence the

X-rays emitted from clusters stream freely into the Universe. In the next section I briefly cover the processes which give rise to ICM X-ray emission and the observables which result. For a magnificently detailed treatise of this topic, see Sarazin (1986)⁴ and references therein.

1.2.1 X-RAY EMISSION

Detailed study of clusters proceeds mainly through spatial and spectral analysis of the ICM. By directly measuring the X-ray emission of the ICM, quantities such as temperature, density, and luminosity per unit volume can be inferred. Having this knowledge about the ICM provides an observational tool for indirectly measuring ICM dynamics, composition, and mass. In this way a complete picture of a cluster can be built-up and other processes such as BCG star formation, AGN feedback activity, or using ICM temperature inhomogeneity to probe cluster dynamic state can be investigated. In this section, I briefly cover how X-ray emission is produced in the ICM and how basic physical properties are then measured.

The main mode of interaction in a fully ionized plasma is the scattering of free electrons off heavy ions. During this process, charged particles are accelerated and thus emit radiation. The mechanism is known as ‘free-free’ emission (ff), or by the tongue-twisting thermal bremsstrahlung (German for “braking radiation”). It is also called bremsstrahlung cooling since the X-ray emission carries away large amounts of energy. The timescale for protons, ions, and electrons to reach equipartition is typically shorter than the age of a cluster (Sarazin, 2003), thus the gas particles populating the emitting plasma can be approximated as being at a uniform temperature with a Maxwell-Boltzmann velocity distribution,

$$f(\vec{v}) = 4\pi \left(\frac{m}{2\pi kT} \right)^{3/2} \vec{v}^2 \exp \left[\frac{-m\vec{v}^2}{2kT} \right] \quad (1.3)$$

⁴Also available at <http://nedwww.ipac.caltech.edu/level5/March02/Sarazin/TOC.html>

where m is mass, T is temperature, k is the Boltzmann constant, and velocity, \vec{v} , is defined as $\vec{v} = \sqrt{v_x^2 + v_y^2 + v_z^2}$. The power emitted per cubic centimeter per second (erg s⁻¹ cm⁻³) from this plasma can be written in the compact form

$$\epsilon^{ff} \equiv 1.4 \times 10^{-27} T^{1/2} n_e n_i Z^2 \bar{g}_B \quad (1.4)$$

where 1.4×10^{-27} is the condensed form of the cgs physical constants and geometric factors associated with integrating over the power per unit area per unit frequency, n_e and n_i are the electron and ion densities, Z is the number of protons of the bending charge, \bar{g}_B is the frequency averaged Gaunt factor (of order unity), and T is the global temperature determined from the spectral cut-off frequency (Rybicki & Lightman, 1986). Below the cut-off frequency, $\nu_c = kT/\hbar$, no photons are created because the energy supplied by charge acceleration is less than the minimum energy required for creation of a photon. Worth noting is that free-free emission is a two-body process and hence the emission goes as the gas density squared while having a weak dependence on the thermal energy, $\epsilon \propto \rho^2 T^{1/2}$ for $T \gtrsim 10^7$ K when the gas has solar abundances.

Superimposed on the thermal emission of the plasma are emission lines of heavy element contaminants such as C, Fe, Mg, N, Ne, O, S, and Si. The widths and relative strengths of these spectral lines are used to constrain the metallicity of the ICM, which is typically quantified using units relative to solar abundance, Z_\odot . On average, the ICM has a metallicity of $\sim 0.3 Z_\odot$, which is mostly stellar detritus (Mushotzky & Loewenstein, 1997; Allen & Fabian, 1998b; Fukazawa et al., 1998). In collisionally ionized plasmas with temperatures and metallicities comparable to the ICM, the dominant ion species is that of the ‘closed-shell’ helium-like ground state (K and L-shells) (Peterson & Fabian, 2006). The K and L shell transitions are extremely sensitive to temperature and electron densities, therefore providing an excellent diagnostic for constraining both of these quantities. The strongest K-shell

transition of the ICM can be seen from iron at $kT \sim 6.7$ keV. If signal-to-noise of the spectrum is of high enough quality, measuring a shift in the energy of this spectral line can be used to confirm or deduce the approximate redshift, and hence distance, of a cluster. The rich series of iron L-shell transitions occur at $0.2 \lesssim T \lesssim 2.0$ keV and are the best diagnostic for measuring metallicity. For the present generation of X-ray instruments, the L-shell lines are seen as a blend with a peak around ~ 1 keV.

Shown in Figs. 1.3 and 1.4 are the unredshifted synthetic spectral models generated with XSPEC (Arnaud, 1996) of a 2 keV and 8 keV gas. Both spectral models have a component added to mimic absorption by gas in the Milky Way, which is seen as attenuation of flux at $E \lesssim 0.4$ keV. For both spectral models the metal abundance is $0.3 Z_{\odot}$. These two spectral models differ by only a factor of four in temperature but note the extreme sensitivity of both the thermal bremsstrahlung exponential cut-off and emission line strengths to temperature.

Equation 1.4 says that observations of ICM X-ray emission will yield two quantities: temperature and density. The gas density can be inferred from the *emission integral*,

$$EI = \int n_e n_p \, dV \quad (1.5)$$

where n_e is the electron density, n_p is the density of hydrogen-like ions, and dV is the gas volume within a differential element. The emission integral is essentially the sum of the square of gas density for all the gas parcels in a defined region. Thus, the gas density within a projected volume can be obtained from the spectral analysis, but it can also be obtained from spatial analysis of the cluster emission, for example from cluster surface brightness.

The number of photons detected per unit area (projected on the plane of the sky) per second is given the name *surface brightness*. Assuming spherical symmetry, 2-dimensional surface brightness can be converted to 3-dimensional emission density. By dividing a cluster observation into concentric annuli originating from the cluster

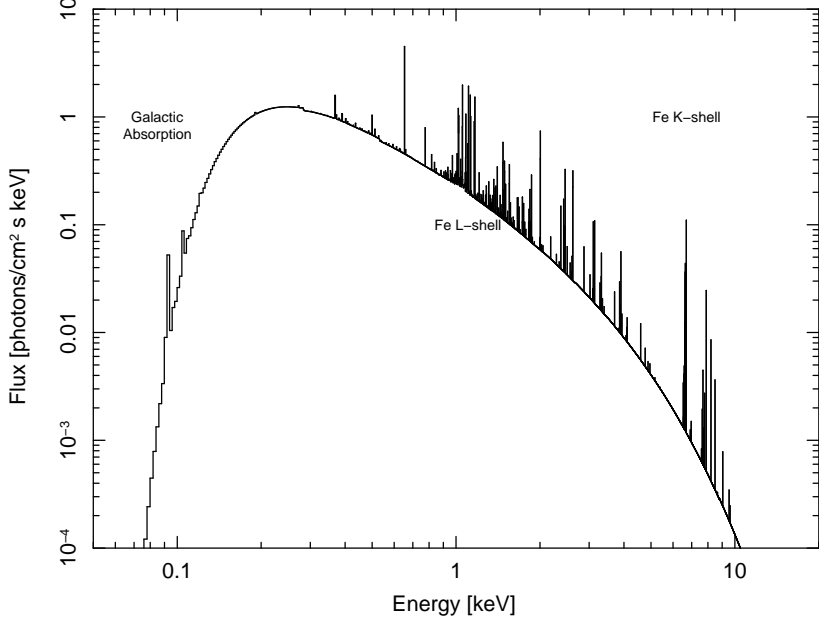


Figure 1.3 Synthetic absorbed thermal spectral model of a $N_H = 10^{20} \text{ cm}^{-2}$, $kT_X = 2.0 \text{ keV}$, $Z/Z_\odot = 0.3$, and zero redshift gas. Notice that the strength of the iron L-shell emission lines is much greater than the iron K-shell lines for this model.

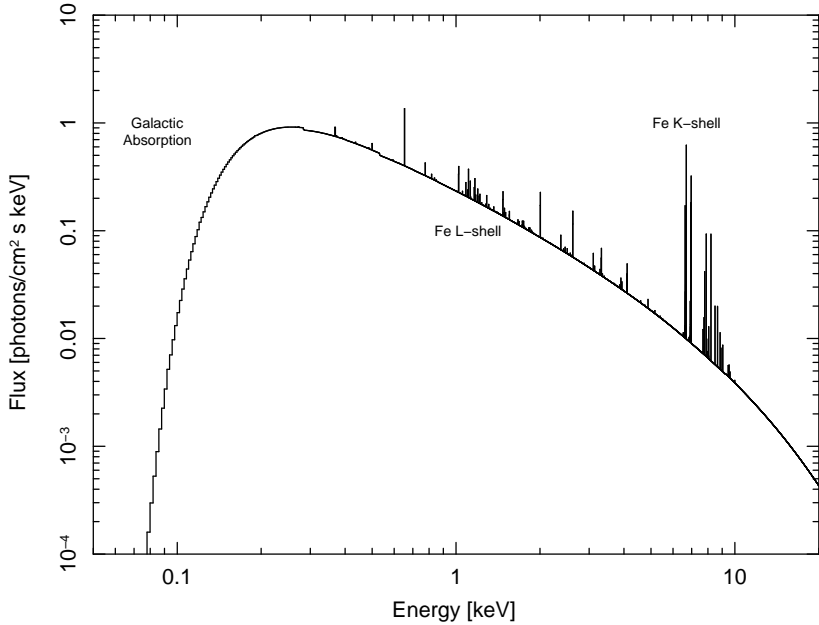


Figure 1.4 Same as Fig. 1.3 except for a $kT_X = 8.0 \text{ keV}$ gas. Notice that for this spectral model the iron L-shell emission lines are much weaker and the iron K-shell lines are much stronger than in the $kT_X = 2.0 \text{ keV}$ model. Also note that the exponential turnover of this model occurs at a higher energy.

center and subtracting off cluster emission at larger radii from emission at smaller radii, the amount of emission from a spherical shell can be reconstructed from the emission in an annular ring. For the spherical shell defined by radii r_i and r_{i+1} , Kriss et al. (1983) shows the relation between the emission density, $C_{i,i+1}$, to the observed surface brightness, $S_{m,m+1}$, of the ring with radii r_m and r_{m+1} , is

$$S_{m,m+1} = \frac{b}{A_{m,m+1}} \sum_{i=1}^m C_{i,i+1} [(V_{i,m+1} - V_{i+1,m+1}) - (V_{i,m} - V_{i+1,m})]. \quad (1.6)$$

where b is the solid angle subtended on the sky by the object, $A_{m,m+1}$ is the area of the ring, and the V terms are the volumes of various shells. This method of reconstructing the cluster emission is called *deprojection*. While assuming spherical symmetry is clearly imperfect, it is not baseless. The purpose of such an assumption is to attain angular averages of the volume density at various radii from an azimuthally averaged surface density. Systematic uncertainties associated with deprojection are discussed in Section §3.3.2.

In this dissertation the spectral model MEKAL (Mewe et al., 1985, 1986; Liedahl et al., 1995) is used for all of the spectral analysis. The MEKAL model normalization, η , is defined as

$$\eta = \frac{10^{-14}}{4\pi D_A^2(1+z)^2} EI \quad (1.7)$$

where z is cluster redshift, D_A is the angular diameter distance, and EI is the emission integral from eqn. 1.5. Recognizing that the count rate, $f(r)$, per volume is equivalent to the emission density, $C_{i,i+1} = f(r)/\int dV$, where dV can be a shell (deprojected) or the sheath of a round column seen edge-on (projected), combining eqns. 1.6 and 3.1 yields an expression for the electron gas density which is a function of direct observables,

$$n_e(r) = \sqrt{\frac{1.2C(r)\eta(r)4\pi[D_A(1+z)]^2}{f(r)10^{-14}}} \quad (1.8)$$

where 1.2 comes from the ionization ratio $n_e=1.2n_p$, $C(r)$ is the radial emission density derived from eqn. 1.6, η is the spectral normalization from eqn. 3.1, D_A is the angular diameter distance, z is redshift, and $f(r)$ is the spectroscopic count rate.

Simply by measuring surface brightness and analyzing spectra, the cluster temperature, metallicity, and density can be inferred. These quantities can then be used to derive pressure, $P = nkT$, where $n \approx 2n_e$. The total gas mass can be inferred using gas density as $M_{gas} = \int(4/3)\pi r^3 n_e$. By further assuming the ICM is in hydrostatic equilibrium, the total cluster mass within radius r is

$$M(r) = \frac{kT(r)}{\mu m G} \left[\frac{d(\log n_e)}{d(\log r)} + \frac{d(\log kT)}{d(\log r)} \right] \quad (1.9)$$

where all variables have their typical definitions. The rate at which the ICM is cooling can also be expressed in simple terms of density and temperature. Given a cooling function, Λ , which is sensitive to temperature and metal abundance (for the ICM $\Lambda(T, Z) \sim 10^{-23}$ ergs cm³ s⁻¹), the cooling rate is given by $r_{cool} = n^2\Lambda(T, Z)$. For some volume, V , the cooling time is then simply the time required for a gas parcel to radiate away its thermal energy,

$$t_{cool} V r_{cool} = \gamma N k T \quad (1.10)$$

$$t_{cool} = \frac{\gamma n k T}{n^2 \Lambda(T, Z)} \quad (1.11)$$

where γ is a constant specific to the type of cooling process (*e.g.* 3/2 for isochoric and 5/2 for isobaric). The cooling time of the ICM can be anywhere between 10^{6–10} yrs. Cooling time is a very important descriptor of the ICM because processes such as the formation of stars and line-emitting nebulae are sensitive to cooling time.

By “simply” pointing a high-resolution X-ray telescope, like *Chandra*, at a cluster and exposing long enough to attain good signal-to-noise, it is possible to derive a roster of fundamental cluster properties: temperature, density, pressure, mass, cooling time,

and even entropy. Entropy is a very interesting quantity which can be calculated using gas temperature and density and is most likely fundamentally connected to processes like AGN feedback and star formation (discussed in Chapters 3 and 4). In the following section I discuss how gas entropy is derived, why it is a useful quantity for understanding clusters, and how it will be utilized later in this dissertation.

1.2.2 ENTROPY

Entropy has both a macroscopic definition (the measure of available energy) and microscopic definition (the measure of randomness), with each being useful in many areas of science. Study of the ICM is a macro-scale endeavor, so the definition of entropy pertinent to discussion of the ICM is as a measure of the thermodynamic processes involving heat transfer. But the conventional macroscopic definition of entropy, $dS = dQ/T$, is not that useful in the context of studying astrophysical objects. Thus we must resort to a simpler, measurable surrogate for entropy, like the adiabat. The adiabatic equation of state for an ideal monatomic gas is $P = K\rho^\gamma$ where K is the adiabatic constant and γ is the ratio of specific heat capacities and has the value of 5/3 for a monatomic gas. Setting $P = \rho kT/\mu m_H$ and solving for K one finds

$$K = \frac{kT}{\mu m_H \rho^{2/3}}. \quad (1.12)$$

where μ is the mean molecular weight of the gas and m_H is the mass of the Hydrogen atom. The true thermodynamic specific entropy using this formulation is $s = k \ln K^{3/2} + s_0$, so neglecting constants and scaling, $s \propto K$ and K shall be called entropy in this dissertation. A further historical simplification can be made to recast eqn. 1.12 using the observables electron density, n_e , and X-ray temperature, T_X (in keV):

$$K = \frac{T_X}{n_e^{2/3}}. \quad (1.13)$$

Equation 1.13 is the definition of entropy used throughout this dissertation. With a simple functional form, “entropy” can be derived directly from X-ray observations. But why study the ICM in terms of entropy?

ICM temperature and density alone primarily reflect the shape and depth of the cluster dark matter potential (Voit et al., 2002). But it is the specific entropy of a gas parcel, $s = c_v \ln(T/\rho^{\gamma-1})$, which governs the density at a given pressure. In addition, the ICM is convectively stable when $ds/dr \geq 0$, thus, without perturbation, the ICM will convect until the lowest entropy gas is near the core and high entropy gas has buoyantly risen to large radii. ICM entropy can also only be changed by addition or subtraction of heat, thus the entropy of the ICM reflects most of the cluster thermal history⁵. Therefore, properties of the ICM can be viewed as a manifestation of the dark matter potential and cluster thermal history - which is encoded in the entropy structure. It is for these reasons that the study of ICM entropy has been the focus of both theoretical and observational study (David et al., 1996; Bower, 1997; Ponman et al., 1999; Lloyd-Davies et al., 2000; Tozzi & Norman, 2001; Voit et al., 2002; Ponman et al., 2003; Piffaretti et al., 2005; Pratt et al., 2006; Donahue et al., 2005, 2006; Morandi & Ettori, 2007; McCarthy et al., 2008).

Radiative cooling and convection of the ICM should result in an entropy distribution which is a power-law across most radii with the only departure occurring at radii smaller than 10% of the virial radius (Voit et al., 2002). Hence deviations away from a power-law entropy profile are indicative of prior heating and cooling and can be exploited to reveal the nature of, for example, AGN feedback. The implication of the intimate connection between entropy and non-gravitational processes being that *both* the breaking of self-similarity and the cooling flow problem (both discussed in Section §1.3) can be studied with ICM entropy.

In Chapter 3 and Chapter 4 I present the results of an exhaustive study of galaxy

⁵While the reduction of entropy seems to violate the second law of thermodynamics, recall that ultimately the Universe is the “isolated” system with which clusters interact.

cluster entropy profiles for a sample of over 230 galaxy clusters taken from the *Chandra* Data Archive. Analysis of these profiles has yielded important results which can be used to constrain models of cluster feedback, understand truncation of the high-mass end of the galaxy luminosity function, and what affect these processes have on the global properties of clusters. The size and scope of the entropy profile library presented in this dissertation is unprecedented in the current scientific literature, and we hope our library, while having provided immediate results, will have a long-lasting and broad utility for the research community. To this end, we have made all data and results available to the public via a project web site⁶.

1.3 THE INCOMPLETE PICTURE OF CLUSTERS

The literature on galaxy clusters is extensive. There has been a great deal already written about clusters (with much more eloquence), and I strongly suggest reading Mushotzky (1984); Kaiser (1986); Evrard (1990); Kaiser (1991); Sarazin (1986); Fabian (1994); Voit (2005); Peterson & Fabian (2006); Markevitch & Vikhlinin (2007); McNamara & Nulsen (2007), and references therein for a comprehensive review of the concepts and topics to be covered in this dissertation. The discussion of Sections §1.3.1 and §1.3.2 focuses on a few unresolved mysteries involving galaxy clusters: the breaking of self-similarity in relation to using clusters in cosmological studies and the cooling flow problem as it relates to galaxy formation.

1.3.1 BREAKING OF SELF-SIMILARITY

We now know the evolution of, and structure within, the Universe are a direct result of the influence from dark energy and dark matter. An all pervading repulsive dark energy has been posited to be responsible for the accelerating expansion of the Universe (Riess et al., 1998; Perlmutter et al., 1999; Riess et al., 2007). Dark matter

⁶<http://www.pa.msu.edu/astro/MC2/accept/>

is an unknown form of matter which interacts with itself and ordinary matter (both baryonic and non-baryonic) through gravitational forces. Up until the last ~ 5 billion years (Riess et al., 1998; Perlmutter et al., 1999; Riess et al., 2007), the influence of dark matter on the Universe has been greater than that of dark energy. The early dominance of dark matter is evident from the existence of large-scale structure like galaxy clusters.

An end result of the gravitational attraction between amalgamations of dark matter particles, called dark matter halos, is the merger of small halos into ever larger halos. Since dark matter far outweighs baryonic matter in the Universe, the baryons are coupled to the dark matter halos via gravity, and hence are dragged along during the halo merger process. Like raindrops falling in a pond that drains into a river which flows into the ocean, the process of smaller units merging to create larger units is found *ad infinitum* in the Universe and is given the name hierarchical structure formation. A useful visualization of the hierarchical structure formation process is shown in Fig. 1.5. Hierarchical formation begins with small objects like the first stars, continues on to galaxies, and culminates in the largest present objects, clusters of galaxies.

In a very simplistic redux, dark energy is attempting to push space apart while dark matter is attempting to pull matter together within that space. Were the balance and evolution of dark energy and dark matter weighted heavily toward one or the other it becomes clear that the amount of structure and its distribution will be different. Thus, the nature of dark matter and dark energy ultimately influence the number of clusters found at any given redshift (*e.g.* White et al., 1993) and hence cluster number counts are immensely powerful in determining cosmological parameters (*e.g.* Borgani et al., 2001).

Individual clusters do not yield the information necessary to study the underlying cosmogony. However, the number density of clusters above a given mass threshold

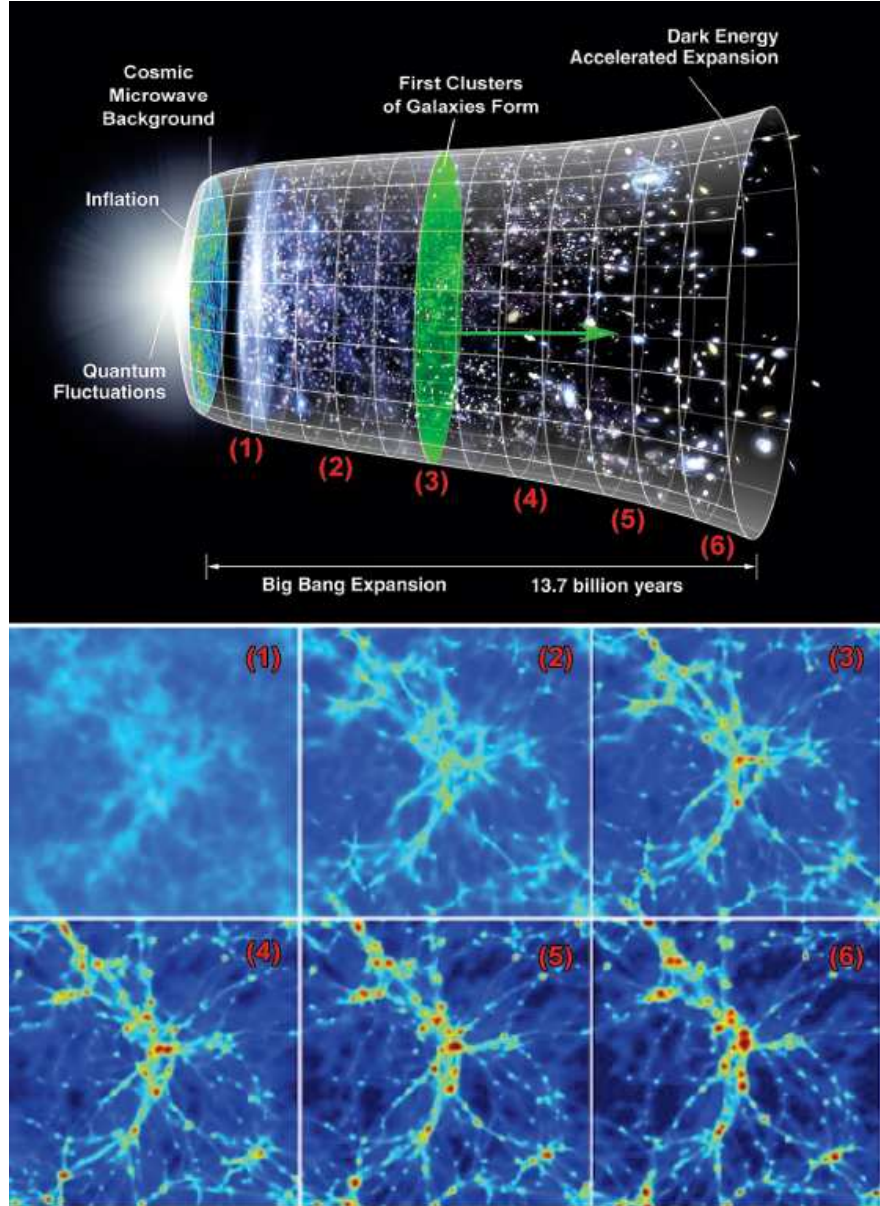


Figure 1.5 *Top panel*: Illustration of hierarchical structure formation. *Bottom panel*: Snapshots from the simulation of a galaxy cluster forming. Each pane is 10 Mpc on a side. Color coding represents gas density along the line of sight (deep red is highest, dark blue is lowest). Each snapshot is numbered on the illustration at the approximate epoch each stage of cluster collapse occurs. Notice that, at first (1-2), very small objects like the first stars and protogalaxies collapse and then these smaller objects slowly merge into much larger halos (3-5). The hierarchical merging process ultimately results in a massive galaxy cluster (6) which continues to grow as sub-clusters near the box edge creep toward the cluster main body. Illustration taken from NASA/WMAP Science Team and modified by author. Simulation snapshots taken from images distributed to the public by the Virgo Consortium on behalf of Dr. Craig Booth: <http://www.virgo.dur.ac.uk>

within a comoving volume element, *i.e.* the cluster mass function, is a useful quantity (Voit, 2005). But the cluster mass function is a powerful cosmological tool only if cluster masses can be accurately measured. With no direct method of measuring cluster mass, easily observable properties of clusters must be used as proxies to infer mass.

Reliable mass proxies, such as cluster temperature and luminosity, arise naturally from the theory that clusters are scaled versions of each other. This property is commonly referred to as self-similarity of mass-observables. More precisely, self-similarity presumes that when cluster-scale gravitational potential wells are scaled by the cluster-specific virial radius, the full cluster population has potential wells which are simply scaled versions of one another (Navarro et al., 1995, 1997). Self-similarity is also expected to yield low-scatter scaling relations between cluster properties such as luminosity and temperature (Kaiser, 1986, 1991; Evrard & Henry, 1991; Navarro et al., 1995, 1997; Eke et al., 1998; Frenk et al., 1999). Consequently, mass-observable relations, such as mass-temperature and mass-luminosity, derive from the fact that most clusters are virialized, meaning the cluster's energy is shared such that the virial theorem, $-2\langle T \rangle = \langle V \rangle$ where $\langle T \rangle$ is average kinetic energy and $\langle V \rangle$ is average potential energy, is a valid approximation. Both theoretical (Evrard et al., 1996; Bryan & Norman, 1998; Mohr et al., 1999; Bialek et al., 2001; Borgani et al., 2002) and observational (Mushotzky, 1984; Edge & Stewart, 1991; White et al., 1997; Allen & Fabian, 1998a; Markevitch et al., 1998; Arnaud & Evrard, 1999; Finoguenov et al., 2001) studies have shown cluster mass correlates well with X-ray temperature and luminosity, but that there is much larger ($\approx 20 - 30\%$) scatter and different slopes for these relations than expected. The breaking of self-similarity is attributed to non-gravitational processes such as ongoing mergers (eg Randall et al., 2002), heating via feedback (eg Cavaliere et al., 1999; Bower et al., 2001), or radiative cooling in the cluster core (eg Voit & Bryan, 2001; Voit et al., 2002).

To reduce the scatter in mass scaling-relations and to increase their utility for weighing clusters, how secondary processes alter temperature and luminosity must first be quantified. It was predicted that clusters with a high degree of spatial uniformity and symmetry (*e.g.* clusters with the least substructure in their dark matter and gas distributions) would be the most relaxed and have the smallest deviations from mean mass-observable relations. The utility of substructure in quantifying relaxation is prevalent in many natural systems, such as a placid lake or spherical gas cloud of uniform density and temperature. Structural analysis of cluster simulations, take for example the recent work of Jeltema et al. (2007) or Ventimiglia et al. (2008), have shown measures of substructure correlate well with cluster dynamical state. But spatial analysis is at the mercy of perspective. If equally robust aspect-independent measures of dynamical state could be found, then quantifying deviation from mean mass-scaling relations would be improved and the uncertainty of inferred cluster masses could be further reduced. Scatter reduction ultimately would lead to a more accurate cluster mass function, and by extension, the constraints on theories explaining dark matter and dark energy could grow tighter.

In Chapter 2, I present work investigating ICM temperature inhomogeneity, a feature of the ICM which has been proposed as a method for better understanding the dynamical state of a cluster (Mathiesen & Evrard, 2001). Temperature inhomogeneity has the advantage of being a spectroscopic quantity and therefore falls into the class of aspect-independent metrics which may be useful for reducing scatter in mass-observable relations. In a much larger context, this dissertation may contribute to the improvement of our understanding of the Universe’s make-up and evolution.

1.3.2 THE COOLING FLOW PROBLEM

For 50% – 66% of galaxy clusters, the densest and coolest ($kT_X \lesssim T_{virial}/2$) ICM gas is found in the central $\sim 10\%$ of the cluster gravitational potential well (Stewart

et al., 1984; Edge et al., 1992; White et al., 1997; Peres et al., 1998; Bauer et al., 2005). For the temperature regime of the ICM, radiative cooling time, t_{cool} (see eqn. 3.7), is more strongly dependent on density than temperature, $t_{\text{cool}} \propto T_g^{1/2} \rho^2$, where T_g is gas temperature and ρ is gas density. The energy lost via radiative cooling is seen as diffuse thermal X-ray emission from the ICM (Gursky et al., 1971; Mitchell et al., 1976; Serlemitsos et al., 1977). When thermal energy is radiated away from the ICM, the gas density must increase while gas temperature and internal pressure respond by decreasing. The cluster core gas densities ultimately reached through the cooling process are large enough such that the cooling time required for the gas to radiate away its thermal energy is much shorter than both the age of the Universe, *e.g.* $t_{\text{cool}} \ll H_0^{-1}$, and the age of the cluster (Cowie & Binney, 1977; Fabian & Nulsen, 1977). Without compensatory heating, it thus follows that the ICM in some cluster cores should cool and condense.

Gas within the cooling radius, r_{cool} , (defined as the radius at which $t_{\text{cool}} = H_0^{-1}$) is underpressured and cannot provide sufficient pressure support to prevent overlying gas layers from forming a subsonic flow of gas toward the bottom of the cluster gravitational potential. However, if when the flowing gas enters the central galaxy it has cooled to the point where the gas temperature equals the central galaxy virial temperature, then adiabatic compression⁷ from the galaxy's gravitational potential well can balance heat losses from radiative cooling. But, if the central galaxy's gravitational potential is flat, then the gas energy gained via gravitational effects can also be radiated away and catastrophic cooling can proceed.

The sequence of events described above was given the name “cooling flow” (Fabian & Nulsen, 1977; Cowie & Binney, 1977; Mathews & Bregman, 1978) and is the most simplistic explanation of what happens to the ICM when it is continuously cooling, spherically symmetric, and homogeneous (see Fabian, 1994; Peterson & Fabian,

⁷As the name indicates, no heat is exchanged during adiabatic compression; but gas temperature rises because the internal gas energy increases due to external work being done on the system.

2006; Donahue & Voit, 2004, for reviews of cool gas in cluster cores). The theoretical existence of cooling flows comes directly from X-ray observations, yet the strongest observational evidence for the existence of cooling flows will be seen when the gas cools below X-ray emitting temperatures and forms stars, molecular clouds, and emission line nebulae. Unfortunately, cooling flow models were first presented at a time when no direct, complementary observational evidence for cooling flows existed, highlighting the difficulty of confronting the models. Undeterred, the X-ray astrophysics community began referring to all clusters which had cores meeting the criterion $t_{\text{cool}} < H_0^{-1}$ as “cooling flow clusters,” a tragic twist of nomenclature fate which has plagued many scientific talks.

A mass deposition rate, \dot{M} , can be inferred for cooling flows based on X-ray observations: $\dot{M} \propto L_X(r < r_{\text{cool}})(kT_X)^{-1}$, where $L_X(r < r_{\text{cool}})$ is the X-ray luminosity within the cooling region, kT_X is the X-ray gas temperature, and \dot{M} typically has units of $M_\odot \text{ yr}^{-1}$. The quantity \dot{M} is useful in getting a handle on how much gas mass is expected to be flowing into a cluster core. Mass deposition rates have been estimated for many clusters and found to be in the range $100 - 1000 M_\odot \text{ yr}^{-1}$ (Fabian et al., 1984; White et al., 1997; Peres et al., 1998). Mass deposition rates can also be estimated using emission from individual spectral lines: $\dot{M} \propto L_X(r < r_{\text{cool}})\epsilon_f(T)$, where $L_X(r < r_{\text{cool}})$ is the X-ray luminosity within the cooling region and $\epsilon_f(T)$ is the emissivity fraction attributable to a particular emission line. The ICM soft X-ray emission lines of Fe XVII, O VIII, and Ne X at $E < 1.5 \text{ keV}$ for example, are especially useful in evaluating the properties of cooling flows. Early low-resolution spectroscopy found mass deposition rates consistent with those from X-ray observations (*e.g.* Canizares et al., 1982).

Not surprisingly, the largest, brightest, and most massive galaxy in a cluster, the brightest cluster galaxy (BCG), typically resides at the bottom of the cluster potential, right at the center of where a cooling flow would terminate. Real cooling flows

were not expected to be symmetric, laminar, continuous, or in thermodynamic equilibrium with the ambient medium. Under these conditions, gas parcels at lower temperatures and pressures experience thermal instability and are expected to rapidly develop and collapse to form gaseous molecular clouds and stars. The stellar and gaseous components of some BCGs clearly indicate some amount of cooling and mass deposition has occurred. But are the properties of the BCG population consistent with cooling flow model predictions? For example, BCGs should be supremely luminous and continually replenished with young, blue stellar populations since the epoch of a BCG's formation. One should then expect the cores of clusters suspected of hosting a cooling flow to have very bright, blue BCGs bathed in clouds of emission line nebulae. However, observations of cooling flow clusters reveal the true nature of the core to not match these expectations of extremely high star formation rates, at least not at the rate of $> 100 M_{\odot} \text{ yr}^{-1}$.

The optical properties of BCGs are well known and these massive galaxies are neither as blue or bright as would be expected from the extended periods of growth via cooling flows (Madau et al., 1996; Shaver et al., 1996; Cowie et al., 1996; Crawford et al., 1999). While attempts were made in the past to selectively channel the unobserved cool gas into optically dark objects, such as in low-mass, distributed star formation (*e.g.* Prestwich & Joy, 1991), methodical searches in the optical, infrared, UV, radio, and soft X-ray wavelengths ($kT_X \lesssim 2.0 \text{ keV}$) have revealed that the total mass of cooler gas associated with cooling flows is much less than expected (Hu et al., 1985; Heckman et al., 1989; McNamara et al., 1990; O'Dea et al., 1994b,a; Antonucci & Barvainis, 1994; McNamara & Jaffe, 1994; Voit & Donahue, 1995; Jaffe & Bremer, 1997; Falcke et al., 1998; Donahue et al., 2000; Edge & Frayer, 2003).

Confirming the suspicion that cooling flows are not cooling as advertised, high-resolution *XMM-Newton* RGS X-ray spectroscopy of clusters expected to host very massive cooling flows definitively proved that the ICM was not cooling to tempera-

tures less than 1/3 of the cluster virial temperature (Peterson et al., 2001; Tamura et al., 2001; Peterson et al., 2003). A cooling X-ray medium which has emission discontinuities at soft energies is not predicted by the simplest single-phase cooling flow models, and a troubling amount of fine-tuning (*e.g.* minimum temperatures, hidden soft emission) must be added to agree with observations. Modifications such as preferential absorption of soft X-rays in the core region (*e.g.* Allen et al., 1993) or turbulent mixing of a multi-phase cooling flow (*e.g.* Fabian et al., 2002) have been successful in matching observations, but these models lack the universality needed to explain why *all* cooling flows are not as massive as expected.

All of the observational evidence has resulted in a two-component “cooling flow problem”: (1) spectroscopy of soft X-ray emission from cooling flow clusters is inconsistent with theoretical predictions, and (2) multiwavelength observations reveal a lack of cooled gas mass or stars to account for the enormous theoretical mass deposition rates implied by simple cooling flow models. So why and how is the cooling of gas below $T_{virial}/3$ suppressed? As is the case with most questions, the best answer thus far is simple: the cooling flow rates were wrong, with many researchers suggesting the ICM has been intermittently heated. But what feedback mechanisms are responsible for hindering cooling in cluster cores? How do these mechanisms operate? What observational constraints can we find to determine which combination of feedback mechanism hypotheses are correct? The answers to these questions have implications for both cluster evolution and massive galaxy formation.

The cores of clusters are active places, so finding heating mechanisms is not too difficult. The prime suspect, and best proposed solution to the cooling flow problem thus far, invokes some combination of supernovae and outbursts from the active galactic nucleus (AGN) in the BCG (Binney & Tabor, 1995; Bower, 1997; Loewenstein, 2000; Voit & Bryan, 2001; Churazov et al., 2002; Brüggen & Kaiser, 2002; Brüggen et al., 2002; Nath & Roychowdhury, 2002; Ruszkowski & Begelman, 2002; Alexander,

2002; Omma et al., 2004; McCarthy et al., 2004; Roychowdhury et al., 2004; Hoeft & Brüggen, 2004; Dalla Vecchia et al., 2004; Soker & Pizzolato, 2005; Pizzolato & Soker, 2005; Voit & Donahue, 2005; Brighenti & Mathews, 2006; Mathews et al., 2006). However, there are some big problems: (1) AGN tend to deposit their energy along preferred axes, while cooling in clusters proceeds in a nearly spherically symmetric distribution in the core; (2) depositing AGN outburst energy at radii nearest the AGN is difficult and the how this mechanism works is not understood; (3) there is a serious scale mismatch in heating and cooling processes which has hampered the development of a self-regulating feedback loop involving AGN. Radiative cooling proceeds as the square of gas density, whereas heating is proportional to volume. Hence, modeling feedback with a small source object, $r \sim 1$ pc, that is capable of compensating for radiative cooling losses over an $\approx 10^6$ kpc³ volume, where the radial density can change by four orders of magnitude, is quite difficult. Dr. Donahue once framed this problem as, “trying to heat the whole of Europe with something the size of a button.”

The basic model of how AGN feedback works is that first gas accretes onto a supermassive black hole at the center of the BCG, resulting in the acceleration and ejection of very high energy particles back into the cluster environment. The energy released in an AGN outburst is of order 10^{58-61} ergs. Under the right conditions, and via poorly understood mechanisms, energy output by the AGN is transferred to the ICM and thermalized, thereby heating the gas. The details of how this process operates is beyond the scope of this dissertation (see McNamara & Nulsen, 2007, for a recent review). However, in this dissertation I do investigate some observable properties of clusters which are directly impacted by feedback mechanisms.

Utilizing the quantity ICM entropy, I present results in Chapter 3 which show that radial ICM entropy distributions for a large sample of clusters have been altered in ways which are consistent with AGN feedback models. Entropy and its connection

to AGN feedback is discussed in Subsection 1.2.2 of this chapter. In Chapter 4 I also present observational results which support the hypothesis of Voit et al. (2008) that electron thermal conduction may be an important mechanism in distributing AGN feedback energy. Hence, this dissertation, in small part, seeks to add to the understanding of how feedback functions in clusters, and thus how to resolve the cooling flow problem. The resolution of which will lead to better models of galaxy formation and cluster evolution.

1.4 CHANDRA X-RAY OBSERVATORY

In this section I briefly describe what makes the *Chandra* X-ray Observatory (*Chandra* or CXO for short) a ground-breaking and unique telescope ideally suited for the work carried out in this dissertation. In depth details of the telescope, instruments, and spacecraft can be found at the CXO web sites^{8,9} or in Weisskopf et al. (2000). Much of what is discussed in the following sections can also be found with more detail in “The Chandra Proposers’ Observatory Guide.”¹⁰

1.4.1 TELESCOPE AND INSTRUMENTS

The mean free path of an X-ray photon in a gas with the density of the Earth’s atmosphere is very short. Oxygen and nitrogen in the atmosphere photoelectrically absorb X-ray photons resulting in 100% attenuation and make X-ray astronomy impossible from the Earth’s surface. Many long-standing theories in astrophysics predict a wide variety of astronomical objects as X-ray emitters. Therefore, astronomers and engineers have been sending X-ray telescopes into the upper atmosphere and space for over 30 years now.

The most recent American X-ray mission to fly is the *Chandra* X-ray Obser-

⁸<http://chandra.harvard.edu/>

⁹<http://cxc.harvard.edu/>

¹⁰<http://cxc.harvard.edu/proposer/POG/>

vatory. It is one of NASA's Great Observatories along with *Compton* (γ -rays), *Hubble* (primarily optical), and *Spitzer* (infrared). *Chandra* was built by Northrop-Grumman and is operated by the National Aeronautics and Space Agency. *Chandra* was launched in July 1999 and resides in a highly elliptical orbit with an apogee of $\sim 140,000$ km and a perigee of $\sim 16,000$ km. One orbit takes ≈ 64 hours to complete. The telescope has four nested iridium-coated paraboloid-hyperboloid mirrors with a focal length of ~ 10 m. An illustration of the *Chandra* spacecraft is shown in Figure 1.6.

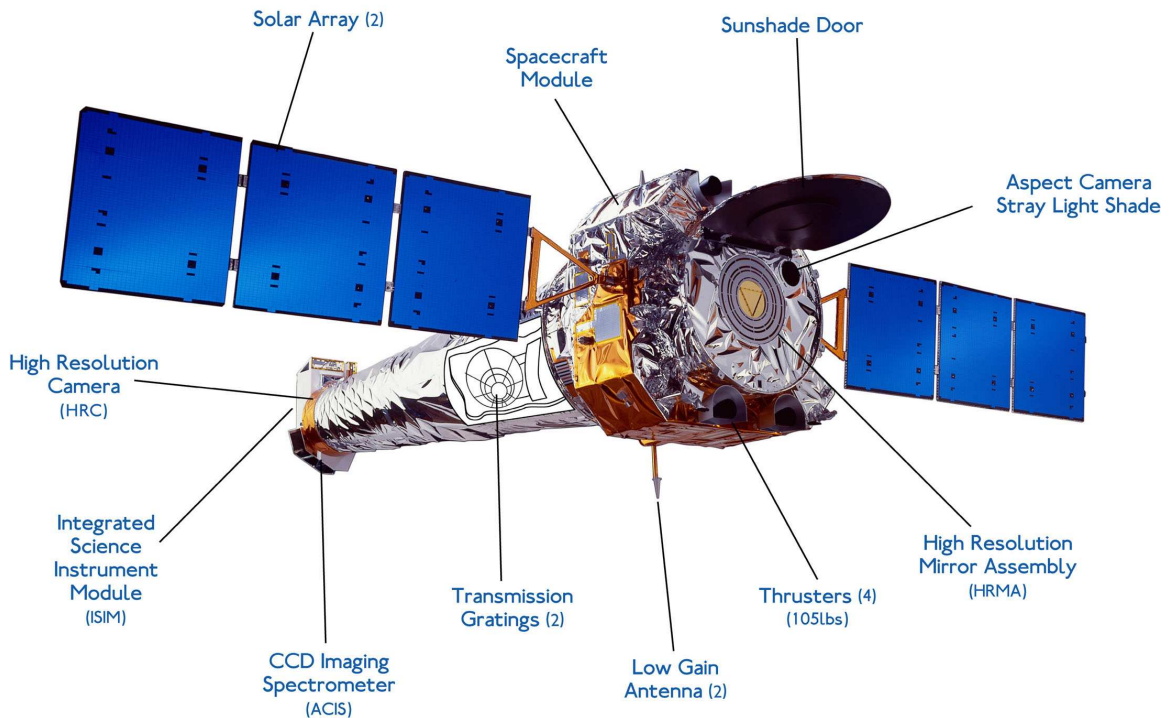


Figure 1.6 An artist's rendition of the *Chandra* spacecraft. *Chandra* is the largest (~ 17 m long; ~ 4 m wide) and most massive ($\sim 23K$ kg) payload ever taken into space by NASA's Space Shuttle Program. The planned lifetime of the mission was 5 years, and the 10 year anniversary party is already planned. Illustration taken from Chandra X-ray Center.

All data presented in this dissertation was collected with the Advanced CCD Imaging Spectrometer (ACIS) instrument¹¹. ACIS is quite an amazing and unique

¹¹<http://acis.mit.edu/acis>

instrument in that it is an imager and medium-resolution spectrometer at the same time. When an observation is taken with ACIS, the data collected contains spatial and spectral information since the location and energy of incoming photons are recorded. The dual nature of ACIS allows the data to be analyzed by spatially dividing up a cluster image and then extracting spectra for these subregions of the image, a technique which is used heavily in this dissertation.

The observing elements of ACIS are $10\ 1024 \times 1024$ CCDs: six linearly arranged CCDs (ACIS-S array) and four CCDs arranged in a 2×2 mosaic (ACIS-I array). The ACIS focal plane is currently kept at a temperature of ~ -120 °C. During an observation, the spacecraft is dithered along a Lissajous curve so parts of the sky which fall in the chip gaps are also observed. Dithering also ensures pixel variations of the CCD response are removed.

The high spatial and energy resolution of *Chandra* and its instruments are ideal for studying clusters of galaxies. The telescope on-board *Chandra* achieves on-axis spatial resolutions of $\lesssim 0.5''/\text{pixel}$ but it is the pixel size of the ACIS instrument ($\sim 0.492''$) which sets the resolution limit for observations. ACIS also has an extraordinary energy resolution of $\Delta E/E \sim 100$. Below energies of ~ 0.3 keV and above energies of ~ 10 keV the ACIS effective area is ostensibly zero. The ACIS effective area also peaks in the energy range $E \sim 0.7 - 2.0$ keV. As shown in Figs. 1.3 and 1.4, a sizeable portion of galaxy cluster emission occurs in the same energy range where the ACIS effective area peaks. The energy resolution of ACIS also allows individual emission line blends to be resolved in cluster spectra. These aspects make *Chandra* a perfect choice for studying clusters and the ICM in detail. Shown in Fig. 1.7 are raw observations of Abell 1795 with the aim-points on ACIS-I (top panel) and ACIS-S (bottom panel). In Fig. 1.8 is a spectrum for the entire cluster extracted from the ACIS-I observation.

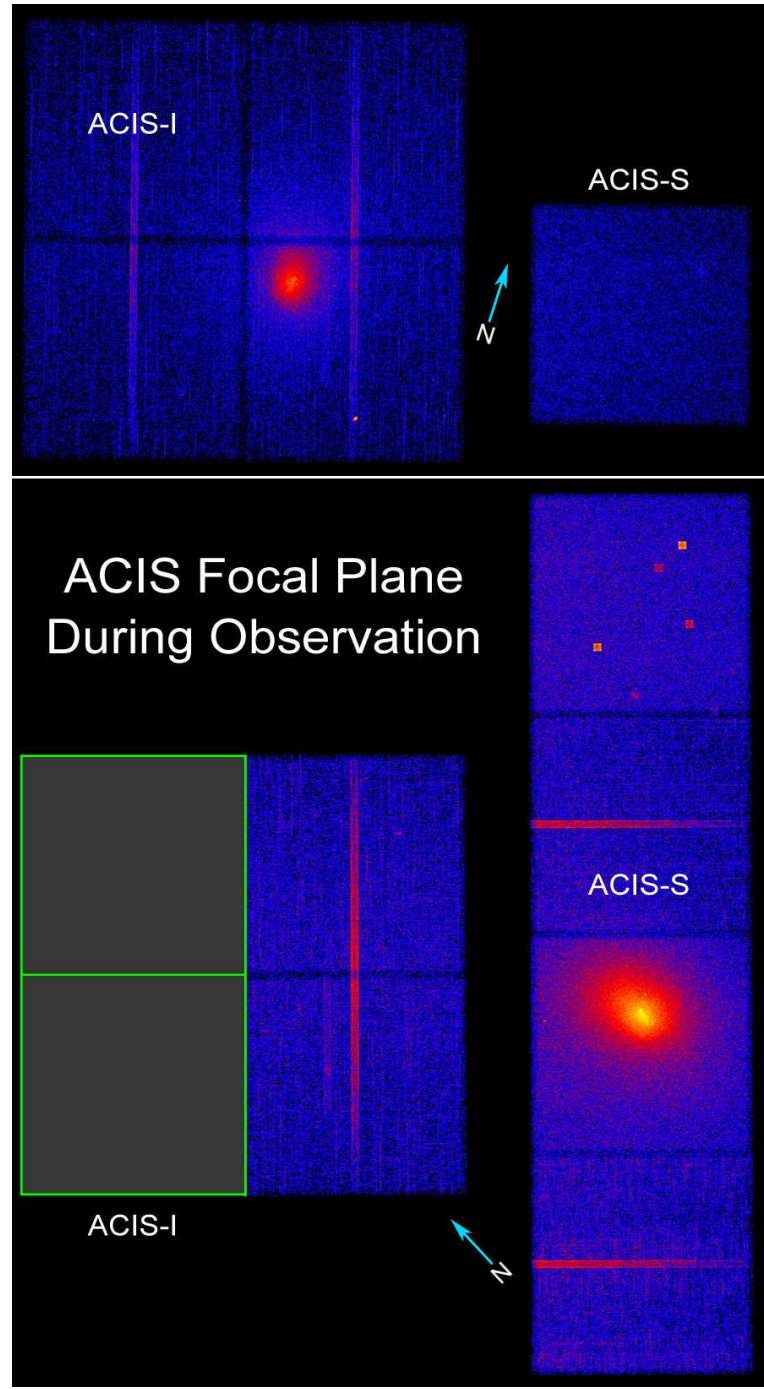


Figure 1.7 In both panels celestial North is indicated by the blue arrow. *Top panel:* ACIS-I aimed observation of Abell 1795. The image has been binned by a factor of four so the whole field could be shown. *Bottom panel:* ACIS-S aimed observation of Abell 1795. Again, the image is binned by a factor of four to show the whole field. For reference, the green boxes mark the ACIS-I chips which were off during this observation.

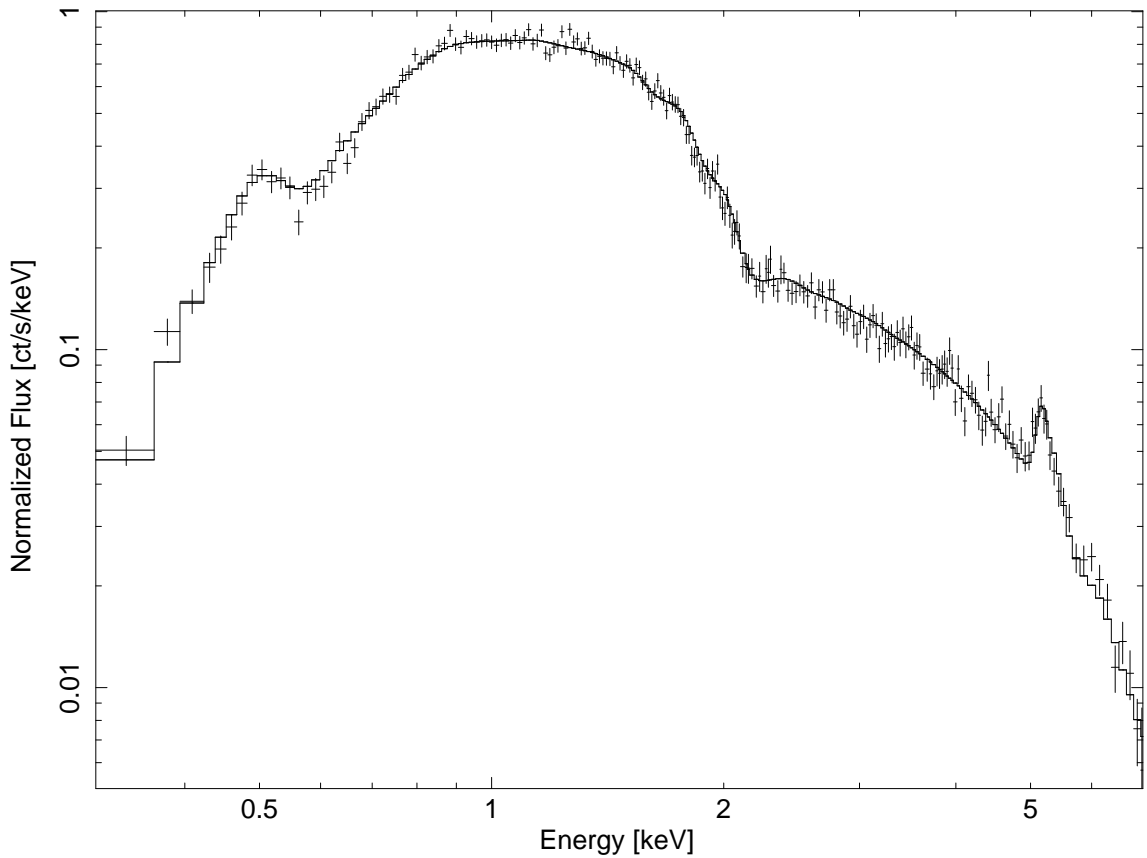


Figure 1.8 Global spectrum of the cluster Abell 1795 with the best-fit single-component absorbed thermal spectral model overplotted (solid line). Comparing this spectrum with those of Figs. 1.3 and 1.4, the effects of finite energy resolution and convolving the spectral model with instrument responses are apparent. Individual spectral lines are now blends, and the spectral shape for $E < 1.0$ keV has changed because of diminishing effective area.

1.4.2 X-RAY BACKGROUND AND CALIBRATION

Chandra is a magnificent piece of engineering, but it is not perfect: observations are contaminated by background, the instruments do not operate at full capacity, and the observatory has a finite lifetime. In this section I briefly discuss these areas and how they might affect past, current, and future scientific study with *Chandra*.

COSMIC X-RAY BACKGROUND (CXB)

Chandra is in a very high Earth orbit and is constantly bathed in high-energy, charged particles originating from the cosmos which interact with the CCDs (the eyes) and the materials housing the instruments (the skull). The CXB is composed of a soft ($E < 2$ keV) component attributable to extragalactic emission, local discrete sources, and spatially varying diffuse Galactic emission. There are also small contributions from the “local bubble” (Snowden, 2004) and charge exchange within the solar system (Wargelin et al., 2004). The possibility of emission from unresolved point sources and other unknown CXB components also exists. In most parts of the sky the soft CXB is not a large contributor to the total background and can be modeled using a combination of power-law and thermal spectral models and then subtracted out of the data.

The CXB also has a hard ($E > 2$ keV) component which arises from mostly extragalactic sources such as quasars and is well modeled as a power-law. The spectral shape of the hard particle background has been quite stable (up until mid-2005) and thus subtracting off the emission by normalizing between observed and expected count rates in a carefully chosen energy band makes removal of the hard component straightforward.

Occasionally there are also very strong X-ray flares. These flares are quite easy to detect in observations because, for a judiciously chosen energy band/time bin combination, the count rate as a function of observation time exhibits a dramatic

spike during flaring. The time intervals containing flare episodes can be excluded from the analysis rendering them harmless. Harmless that is provided the flare was not too long and some of the observing time allotment is usable.

INSTRUMENTAL EFFECTS AND SOURCES OF UNCERTAINTY

There are a number of instrumental effects which must be considered when analyzing data taken with *Chandra*. The geometric area of the telescope's mirrors does not represent the “usable” area of the mirrors. The true *effective area* of *Chandra* has been defined by the CXC as the product of mirror geometric area, reflectivity, off-axis vignetting, quantum efficiency of the detectors, energy resolution of the detectors, and grating efficiency (gratings were not in use during any of the observations used in this dissertation). To varying degrees, all of these components depend on energy and a few of them also have a spatial dependence. Discussion of the effective area is a lengthy and involved topic. A more concise understanding of the effective area can be attained from visualization, hence the effective area as a function of energy is shown in Figure 1.9.

The ACIS instrument is also subject to dead/bad pixels, damage done by interaction with very high-energy cosmic rays, imperfect read-out as a function of CCD location, and a hydrocarbon contaminate which has been building up since launch (Marshall et al., 2004).

Observations are also at the mercy of uncertainty sources. The data reduction software provided by the CXC (CIAO) and our own reduction pipeline (CORP, discussed in Appendix ??) takes into consideration:

1. Instrumental effects and calibration
2. $\approx 3\%$ error in absolute ACIS flux calibration
3. Statistical errors in the sky and background count rates

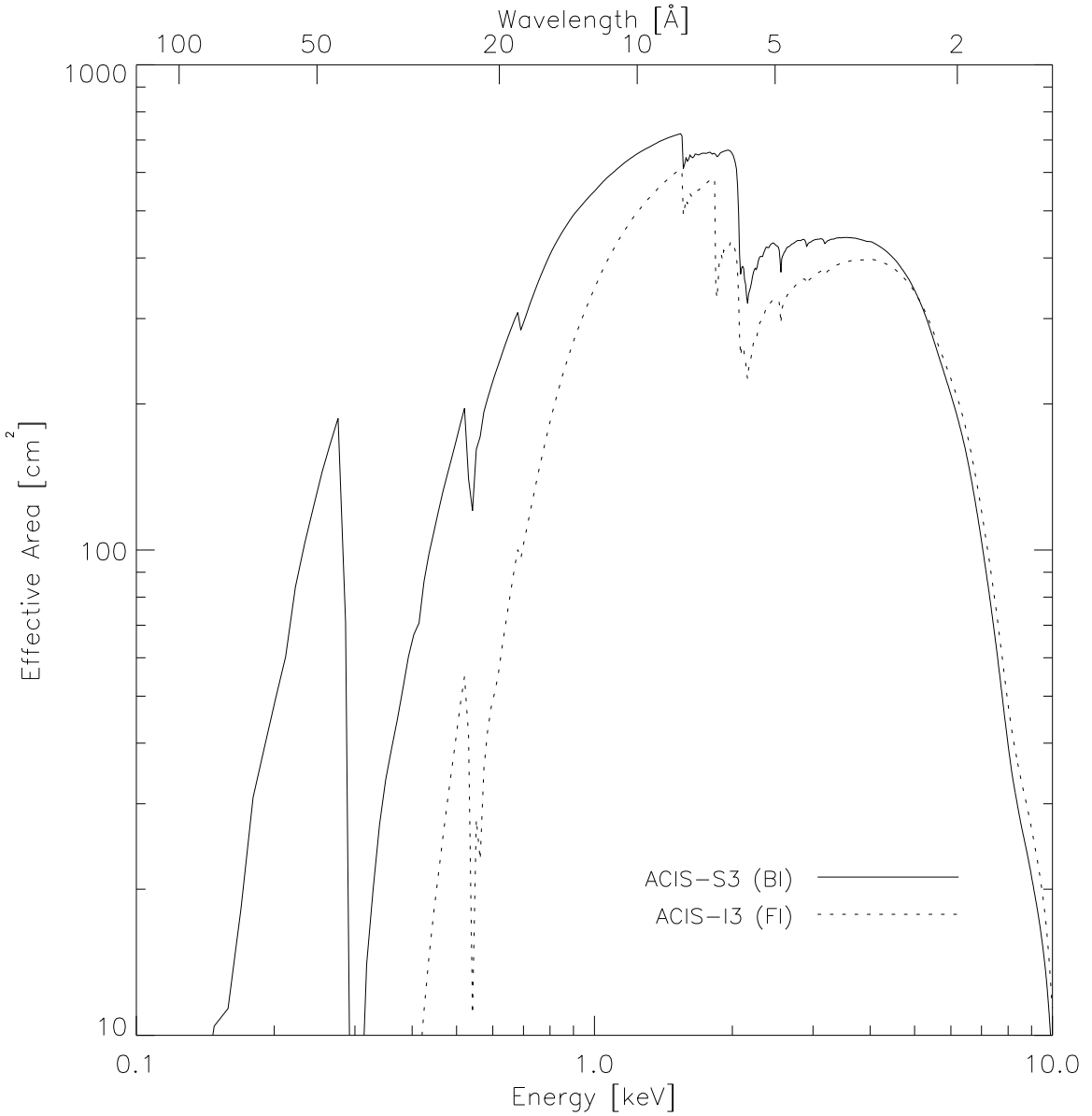


Figure 1.9 *Chandra* effective area as a function of energy. The effective area results from the product of mirror geometric area, reflectivity, off-axis vignetting, quantum efficiency of the detectors, energy resolution of the detectors, and grating efficiency. Note the ACIS peak sensitivity is in the energy range where the majority of ICM occurs, $E = 0.1 - 2.0$ keV. Figure taken from Chandra X-ray Center.

4. Errors due to uncertainty in the background normalization
5. Error due to the $\approx 2\%$ systematic uncertainty in the background spectral shape
6. Cosmic variance
7. Unresolved source intensity
8. Scattering of source flux

The list provided above is not comprehensive, but highlights the largest sources of uncertainty: counting statistics, instrument calibration, and background. In each section of this dissertation where data analysis is discussed, the uncertainty and error analysis is discussed in the context of the science objectives.

The *Chandra* mission was scheduled for a minimum five year mission with the expectation that it would go longer. Nearing the ten year anniversary of launch, it is therefore useful to wonder how *Chandra* might be operating in years to come and what the future holds for collecting data with *Chandra* five and even ten years from now. The “life expectancy” of *Chandra* can be broken down into the categories: spacecraft health, orbit stability, instrument performance, and observation constraint evolution. Given the continued progress of understanding *Chandra*’s calibration, the relative stability of the X-ray background, and the overall health of the telescope as of last review, it has been suggested that *Chandra* will survive at least a 15 year mission, *e.g.* a decommissioning ~ 2014 (Bucher, 2007, 2008).

Chapter Two

Cavagnolo, Kenneth W., Donahue, Megan, Voit, G. Mark, Sun, Ming (2008). Bandpass Dependence of X-ray Temperatures in Galaxy Clusters. The Astrophysical Journal. 682:821-830.

CHAPTER 2:

BANDPASS DEPENDENCE OF X-RAY

TEMPERATURES IN GALAXY

CLUSTERS

2.1 INTRODUCTION

The normalization, shape, and evolution of the cluster mass function are useful for measuring cosmological parameters (*e.g.* Evrard, 1989; Wang & Steinhardt, 1998; Haiman et al., 2001; Wang et al., 2004b). In particular, the evolution of large scale structure formation provides a complementary and distinct constraint on cosmological parameters to those tests which constrain them geometrically, such as supernovae (Riess et al., 1998, 2007) and baryon acoustic oscillations (Eisenstein et al., 2005). However, clusters are a useful cosmological tool only if we can infer cluster masses from observable properties such as X-ray luminosity, X-ray temperature, lensing shear, optical luminosity, or galaxy velocity dispersion. Empirically, the correlation of mass to these observable properties is well-established (see Voit, 2005, for a review). But, there is non-negligible scatter in mass-observable scaling relations which must be accounted for if clusters are to serve as high-precision mass proxies necessary for using clusters to study cosmological parameters such as the dark energy equation of state. However, if we could identify a “second parameter” – possibly reflecting the degree of relaxation in the cluster – we could improve the utility of clusters as cosmological probes by parameterizing and reducing the scatter in mass-observable

scaling relations.

Toward this end, we desire to quantify the dynamical state of a cluster beyond simply identifying which clusters appear relaxed and those which do not. Most clusters are likely to have a dynamical state which is somewhere in between (O’Hara et al., 2006; Kravtsov et al., 2006; Ventimiglia et al., 2008). The degree to which a cluster is virialized must first be quantified within simulations that correctly predict the observable properties of the cluster. Then, predictions for quantifying cluster virialization may be tested, and possibly calibrated, with observations of an unbiased sample of clusters (*e.g.* REXCESS sample of Böhringer et al., 2007).

One study that examined how relaxation might affect the observable properties of clusters was conducted by (Mathiesen & Evrard, 2001, hereafter ME01) using the ensemble of simulations by Mohr & Evrard (1997). ME01 found that most clusters which had experienced a recent merger were cooler than the cluster mass-observable scaling relations predicted. They attributed this to the presence of cool, spectroscopically unresolved accreting subclusters which introduce energy into the ICM and have a long timescale for dissipation. The consequence was an under-prediction of cluster binding masses of 15 – 30% (Mathiesen & Evrard, 2001). It is important to note that the simulations of Mohr & Evrard (1997) included only gravitational processes. The intervening years have proven that radiative cooling is tremendously important in shaping the global properties of clusters (*e.g.* McCarthy et al., 2004; Poole et al., 2006; Nagai et al., 2007). Therefore, the magnitude of the effect seen by ME01 could be somewhat different if radiative processes are included.

One empirical observational method of quantifying the degree of cluster relaxation involves using ICM substructure and employs the power in ratios of X-ray surface brightness moments (Buote & Tsai, 1995, 1996; Jeltema et al., 2005). Although an excellent tool, power ratios suffer from being aspect-dependent (Jeltema et al., 2007; Ventimiglia et al., 2008). The work of ME01 suggested a complementary measure

of substructure which does not depend on projected perspective. In their analysis, they found hard-band (2.0-9.0 keV) temperatures were $\sim 20\%$ hotter than broadband (0.5-9.0 keV) temperatures. Their interpretation was that the cooler broadband temperature is the result of unresolved accreting cool subclusters which are contributing significant amounts of line emission to the soft band ($E < 2$ keV). This effect has been studied and confirmed by Mazzotta et al. (2004) and Vikhlinin (2006) using simulated *Chandra* and *XMM-Newton* spectra.

ME01 suggested that this temperature skewing, and consequently the fingerprint of mergers, could be detected utilizing the energy resolution and soft-band sensitivity of *Chandra*. They proposed selecting a large sample of clusters covering a broad dynamical range, fitting a single-component temperature to the hard-band and broadband, and then checking for a net skew above unity in the hard-band to broadband temperature ratio. In this chapter we present the findings of just such a temperature-ratio test using *Chandra* archival data. We find the hard-band temperature exceeds the broadband temperature, on average, by $\sim 16\%$ in multiple flux-limited samples of X-ray clusters from the *Chandra* archive. This mean excess is weaker than the 20% predicted by ME01, but is significant at the 12σ level nonetheless. Hereafter, we refer to the hard-band to broadband temperature ratio as T_{HBR} . We also find that non-cool core systems and mergers tend to have higher values of T_{HBR} . Our findings suggest that T_{HBR} is an indicator of a cluster's temporal proximity to the most recent merger event.

This chapter proceeds in the following manner: In §2.2 we outline sample-selection criteria and *Chandra* observations selected under these criteria. Data reduction and handling of the X-ray background is discussed in §2.3. Spectral extraction is discussed in §2.4, while fitting and simulated spectra are discussed in §2.5. Results and discussion of our analysis are presented in §2.6. A summary of our work is presented in §2.7. For this work we have assumed a flat Λ CDM Universe with cosmology $\Omega_M = 0.3$,

$\Omega_\Lambda = 0.7$, and $H_0 = 70 \text{ km s}^{-1} \text{ Mpc}^{-1}$. All quoted uncertainties are at the 1.6σ level (90% confidence).

2.2 SAMPLE SELECTION

Our sample was selected from observations publicly available in the *Chandra* X-ray Telescope's Data Archive (CDA). Our initial selection pass came from the *ROSAT* Brightest Cluster Sample (Ebeling et al., 1998), RBC Extended Sample (Ebeling et al., 2000), and *ROSAT* Brightest 55 Sample (Edge et al., 1990; Peres et al., 1998). The portion of our sample at $z \gtrsim 0.4$ can also be found in a combination of the *Einstein* Extended Medium Sensitivity Survey (Gioia et al., 1990), North Ecliptic Pole Survey (Henry et al., 2006), *ROSAT* Deep Cluster Survey (Rosati et al., 1995), *ROSAT* Serendipitous Survey (Vikhlinin et al., 1998), and Massive Cluster Survey (Ebeling et al., 2001). We later extended our sample to include clusters found in the REFLEX Survey (Böhringer et al., 2004). Once we had a master list of possible targets, we cross-referenced this list with the CDA and gathered observations where a minimum of R_{5000} (defined below) is fully within the CCD field of view.

R_{Δ_c} is defined as the radius at which the average cluster density is Δ_c times the critical density of the Universe, $\rho_c = 3H(z)^2/8\pi G$. For our calculations of R_{Δ_c} we adopt the relation from Arnaud et al. (2002):

$$\begin{aligned} R_{\Delta_c} &= 2.71 \text{ Mpc } \beta_T^{1/2} \Delta_z^{-1/2} (1+z)^{-3/2} \left(\frac{kT_X}{10 \text{ keV}} \right)^{1/2} \\ \Delta_z &= \frac{\Delta_c \Omega_M}{18\pi^2 \Omega_z} \\ \Omega_z &= \frac{\Omega_M (1+z)^3}{[\Omega_M (1+z)^3] + [(1-\Omega_M - \Omega_\Lambda)(1+z)^2] + \Omega_\Lambda} \end{aligned} \quad (2.1)$$

where R_{Δ_c} is in units of h_{70}^{-1} , Δ_c is the assumed density contrast of the cluster at R_{Δ_c} , and β_T is a numerically determined, cosmology-independent ($\lesssim \pm 20\%$) normalization

for the virial relation $GM/2R = \beta_T kT_{virial}$. We use $\beta_T = 1.05$ taken from Evrard et al. (1996).

The result of our CDA search was a total of 374 observations of which we used 244 for 202 clusters. The clusters making up our sample cover a redshift range of $z = 0.045 - 1.24$, a temperature range of $T_X = 2.6 - 19.2$ keV, and bolometric luminosities of $L_{bol} = 0.12 - 100.4 \times 10^{44}$ ergs s $^{-1}$. The bolometric ($E = 0.1 - 100$ keV) luminosities for our sample clusters plotted as a function of redshift are shown in Figure 2.1. These L_{bol} values are calculated from our best-fit spectral models and are limited to the region of the spectral extraction (from $R = 70$ kpc to $R = R_{2500}$, or R_{5000} in the cases in which no R_{2500} fit was possible). Basic properties of our sample are listed in Table ??.

For the sole purpose of defining extraction regions based on fixed overdensities as discussed in §2.4, fiducial temperatures (measured with *ASCA*) and redshifts were taken from Horner (2001) (all redshifts confirmed with NED¹). We show below that the *ASCA* temperatures are sufficiently close to the *Chandra* temperatures such that R_{Δ_c} is reliably estimated to within 20%. Note that R_{Δ_c} is proportional to $T^{1/2}$, so that a 20% error in the temperature leads to only a 10% error in R_{Δ_c} , which in turn has no detectable effect on our final results. For clusters not listed in Horner (2001), we used a literature search to find previously measured temperatures. If no published value could be located, we measured the global temperature by recursively extracting a spectrum in the region $0.1 < r < 0.2R_{500}$ fitting a temperature and recalculating R_{500} . This process was repeated until three consecutive iterations produced R_{500} values which differed by $\leq 1\sigma$. This method of temperature determination has been employed in other studies, see Sanderson et al. (2006) and Henry et al. (2006) as examples.

¹<http://nedwww.ipac.caltech.edu/>

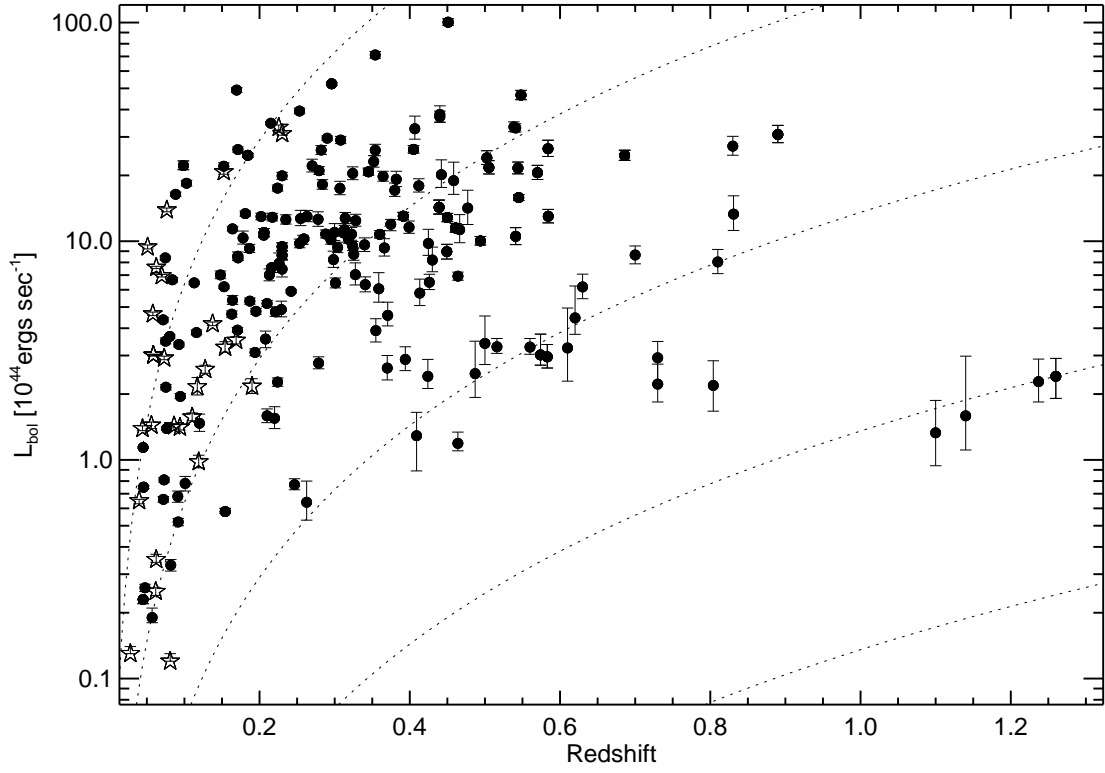


Figure 2.1 Bolometric luminosity ($E = 0.1 - 100$ keV) plotted as a function of redshift for the 202 clusters which make up the initial sample. L_{bol} values are limited to the region of spectral extraction, $R = R_{2500\text{--CORE}}$. For clusters without $R_{2500\text{--CORE}}$ fits, $R = R_{5000\text{--CORE}}$ fits were used and are denoted in the figure by empty stars. Dotted lines represent constant fluxes of 3.0×10^{-15} , 10^{-14} , 10^{-13} , and 10^{-12} $\text{ergs s}^{-1} \text{ cm}^{-2}$.

2.3 *Chandra* DATA

2.3.1 REPROCESSING AND REDUCTION

All data sets were reduced using the *Chandra*} Interactive Analysis of Observations package (CIAO) and accompanying Calibration Database (CALDB). Using CIAO 3.3.0.1 and CALDB 3.2.2, standard data analysis was followed for each observation to apply the most up-to-date time-dependent gain correction and when appropriate, charge transfer inefficiency correction (Townsley et al., 2000).

Point sources were identified in an exposure-corrected events file using the adaptive wavelet tool WAVDETECT (Freeman et al., 2002). A 2σ region surrounding each point source was automatically output by WAVDETECT to define an exclusion mask. All point sources were then visually confirmed and we added regions for point sources which were missed by WAVDETECT and deleted regions for spuriously detected “sources.” Spurious sources are typically faint CCD features (chip gaps and chip edges) not fully removed after dividing by the exposure map. This process resulted in an events file (at “level 2”) that has been cleaned of point sources.

To check for contamination from background flares or periods of excessively high background, light curve analysis was performed using Maxim Markevitch’s contributed CIAO script LC_CLEAN.SL². Periods with count rates $\geq 3\sigma$ and/or a factor ≥ 1.2 of the mean background level of the observation were removed from the good time interval file. As prescribed by Markevitch’s cookbook³, ACIS front-illuminated (FI) chips were analyzed in the 0.3 – 12.0 keV range, and the 2.5 – 7.0 keV energy range for the ACIS back-illuminated (BI) chips.

When a FI and BI chip were both active during an observation, we compared light curves from both chips to detect long duration, soft-flares which can go undetected on the FI chips but show up on the BI chips. While rare, this class of flare must

²<http://cxc.harvard.edu/contrib/maxim/acisbg/>

³<http://cxc.harvard.edu/contrib/maxim/acisbg/COOKBOOK>

be filtered out of the data, as it introduces a spectral component which artificially increases the best-fit temperature via a high energy tail. We find evidence for a long duration soft flare in the observations of Abell 1758 (David & Kempner, 2004), CL J2302.8+0844, and IRAS 09104+4109. These flares were handled by removing the time period of the flare from the GTI file.

Defining the cluster “center” is essential for the later purpose of excluding cool cores from our spectral analysis (see §2.4). To determine the cluster center, we calculated the centroid of the flare cleaned, point-source free level-2 events file filtered to include only photons in the 0.7 – 7.0 keV range. Before centroiding, the events file was exposure-corrected and “holes” created by excluding point sources were filled using interpolated values taken from a narrow annular region just outside the hole (holes are not filled during spectral extraction discussed in §2.4). Prior to centroiding, we defined the emission peak by heavily binning the image, finding the peak value within a circular region extending from the peak to the chip edge (defined by the radius R_{max}), reducing R_{max} by 5%, reducing the binning by a factor of 2, and finding the peak again. This process was repeated until the image was unbinned (binning factor of 1). We then returned to an unbinned image with an aperture centered on the emission peak with a radius R_{max} and found the centroid using CIAO’s DMSTAT. The centroid, (x_c, y_c) , for a distribution of N good pixels with coordinates (x_i, y_j) and values $f(x_i, y_j)$ is defined as:

$$\begin{aligned} Q &= \sum_{i,j=1}^N f(x_i, y_i) \\ x_c &= \frac{\sum_{i,j=1}^N x_i \cdot f(x_i, y_i)}{Q} \\ y_c &= \frac{\sum_{i,j=1}^N y_i \cdot f(x_i, y_i)}{Q}. \end{aligned} \tag{2.2}$$

If the centroid was within 70 kpc of the emission peak, the emission peak was

selected as the center, otherwise the centroid was used as the center. This selection was made to ensure all “peaky” cool cores coincided with the cluster center, thus maximizing their exclusion later in our analysis. All cluster centers were additionally verified by eye.

2.3.2 X-RAY BACKGROUND

Because we measured a global cluster temperature, specifically looking for a temperature ratio shift in energy bands which can be contaminated by the high-energy particle background or the soft local background, it was important to carefully analyze the background and subtract it from our source spectra. Below we outline three steps taken in handling the background: customization of blank-sky backgrounds, re-normalization of these backgrounds for variation of hard-particle count rates, and fitting of soft background residuals.

We used the blank-sky observations of the X-ray background from Markevitch et al. (2001) and supplied within the CXC CALDB. First, we compared the flux from the diffuse soft X-ray background of the *ROSAT* All-Sky Survey (*RASS*) combined bands *R*12, *R*45, and *R*67 to the 0.7-2.0 keV flux in each extraction aperture for each observation. *RASS* combined bands give fluxes for energy ranges of 0.12-0.28, 0.47-1.21, and 0.76-2.04 keV respectively corresponding to *R*12, *R*45, and *R*67. For the purpose of simplifying subsequent analysis, we discarded observations with an *R*45 flux $\geq 10\%$ of the total cluster X-ray flux.

The appropriate blank-sky dataset for each observation was selected from the CALDB, reprocessed exactly as the observation was, and then reprojected using the aspect solutions provided with each observation. For observations on the ACIS-I array, we reprojected blank-sky backgrounds for chips I0-I3 plus chips S2 and/or S3. For ACIS-S observations, we created blank-sky backgrounds for the target chip, plus chips I2 and/or I3. The additional off aim-point chips were included only if

they were active during the observation and had available blank-sky data sets for the observation time period. Off aim-point chips were cleaned for point sources and diffuse sources using the method outlined in §2.3.1.

The additional off aim-point chips were included in data reduction since they contain data which is farther from the cluster center and are therefore more useful in analyzing the observation background. For observations which did not have a matching off aim-point blank-sky background, a source-free region of the active chips is located and used for background normalization. To normalize the hard particle component we measured fluxes for identical regions in the blank-sky field and target field in the 9.5-12.0 keV range. The effective area of the ACIS arrays above 9.5 keV is approximately zero, and thus the collected photons there are exclusively from the particle background.

A histogram of the ratios of the 9.5-12.0 keV count rate from an observation's off aim-point chip to that of the observation specific blank-sky background are presented in Figure 2.2. The majority of the observations are in agreement to $\lesssim 20\%$ of the blank-sky background rate, which is small enough to not affect our analysis. Even so, we re-normalized all blank-sky backgrounds to match the observed background.

Normalization brings the observation background and blank-sky background into agreement for $E > 2$ keV, but even after normalization, typically, there may exist a soft excess/deficit associated with the spatially varying soft Galactic background. Following the technique detailed in Vikhlinin et al. (2005), we constructed and fit soft residuals for this component. For each observation we subtracted a spectrum of the blank-sky field from a spectrum of the off aim-point field to create a soft residual. The residual was fit with a solar abundance, zero-redshift MEKAL model (Mewe et al., 1985, 1986; Liedahl et al., 1995) in which the normalization was allowed to be negative. The resulting best-fit temperatures for all of the soft residuals identified here were between 0.2-1.0 keV, which is in agreement with results of Vikhlinin et al.

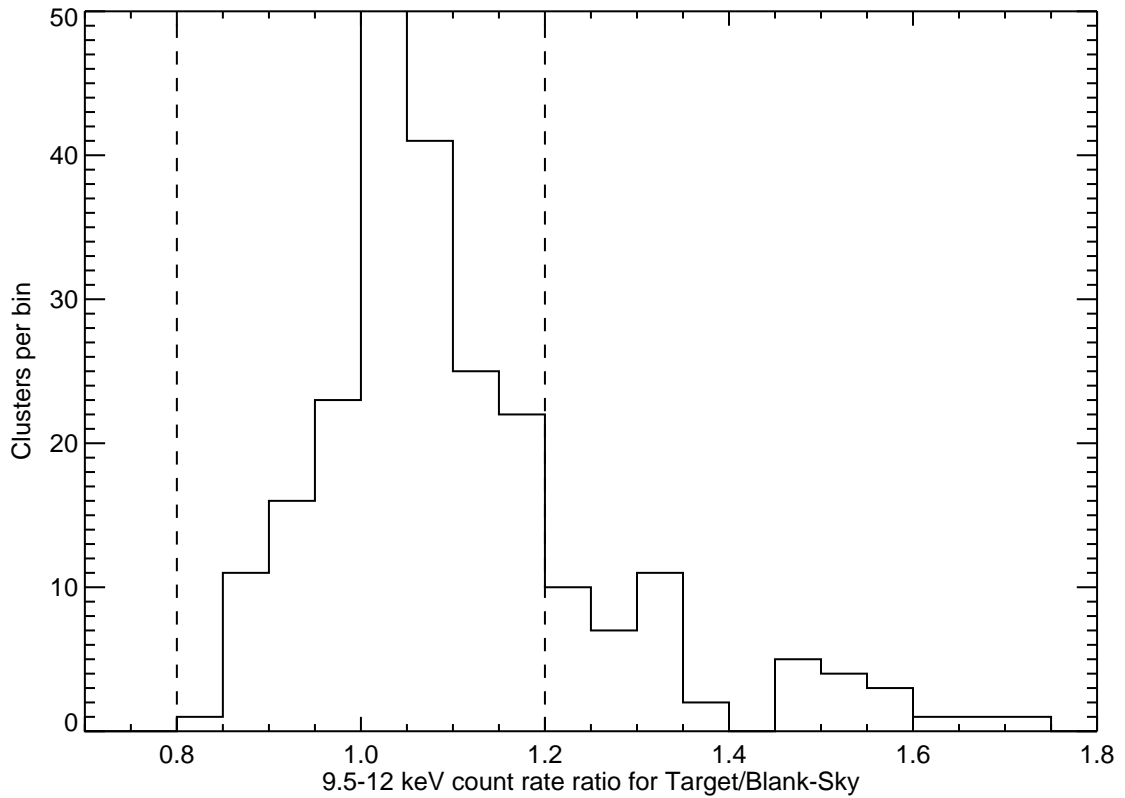


Figure 2.2 Ratio of target field and blank-sky field count rates in the 9.5-12.0 keV band for all 244 observations in our initial sample. Vertical dashed lines represent $\pm 20\%$ of unity. Despite the good agreement between the blank-sky background and observation count rates for most observations, all backgrounds are normalized.

(2005). The model normalization of this background component was then scaled to the cluster sky area. The re-scaled component was included as a fixed background component during fitting of a cluster’s spectra.

2.4 SPECTRAL EXTRACTION

The simulated spectra calculated by ME01 were analyzed in a broad energy band of $0.5 - 9.0$ keV and a hard energy band of $2.0_{\text{rest}} - 9.0$ keV, but to make a reliable comparison with *Chandra* data we used narrower energy ranges of $0.7-7.0$ keV for the broad energy band and $2.0_{\text{rest}} - 7.0$ keV for the hard energy band. We excluded data below 0.7 keV to avoid the effective area and quantum efficiency variations of the ACIS detectors, and excluded energies above 7.0 keV in which diffuse source emission is dominated by the background and where *Chandra*’s effective area is small. We also accounted for cosmic redshift by shifting the lower energy boundary of the hard-band from 2.0 keV to $2.0/(1+z)$ keV (henceforth, the 2.0 keV cut is in the rest frame).

ME01 calculated the relation between $T_{0.5-9.0}$ and $T_{2.0-9.0}$ using apertures of R_{200} and R_{500} in size. While it is trivial to calculate a temperature out to R_{200} or R_{500} for a simulation, such a measurement at these scales is extremely difficult with *Chandra* observations (see Vikhlinin et al. (2005) for a detailed example). Thus, we chose to extract spectra from regions with radius R_{5000} , and R_{2500} when possible. Clusters analyzed only within R_{5000} are denoted in Table ?? by a double dagger (\ddagger).

The cores of some clusters are dominated by gas at $\lesssim T_{\text{virial}}/2$ which can greatly affect the global best-fit temperature; therefore, we excised the central 70 kpc of each aperture. These excised apertures are denoted by “-CORE” in the text. Recent work by Maughan (2007) has shown excising $0.15 R_{500}$ rather than a static 70 kpc reduces scatter in mass-observable scaling relations. However, our smaller excised region seems sufficient for this investigation because for cool core clusters the average radial temperature at $r > 70$ kpc is approximately isothermal (Vikhlinin et al., 2005).

Indeed, we find that cool core clusters have smaller than average T_{HBB} when the 70 kpc region has been excised (§2.6.3).

Although some clusters are not circular in projection, but rather are elliptical or asymmetric, we found that assuming spherical symmetry and extracting spectra from a circular annulus did not significantly change the best-fit values. For another such example see Bauer et al. (2005).

After defining annular apertures, we extracted source spectra from the target cluster and background spectra from the corresponding normalized blank-sky dataset. By standard CIAO means we created weighted effective area functions (WARFs) and redistribution matrices (WRMFs) for each cluster using a flux-weighted map (WMAP) across the entire extraction region. The WMAP was calculated over the energy range 0.3-2.0 keV to weight calibrations that vary as a function of position on the chip. The CCD characteristics which affect the analysis of extended sources, such as energy dependent vignetting, are contained within these files. Each spectrum was then binned to contain a minimum of 25 counts per channel.

2.5 SPECTRAL ANALYSIS

2.5.1 FITTING

Spectra were fit with XSPEC 11.3.2ag (Arnaud, 1996) using a single-temperature MEKAL model in combination with the photoelectric absorption model WABS (Morrison & McCammon, 1983) to account for Galactic absorption. Galactic absorption values, N_H , are taken from Dickey & Lockman (1990). The potentially free parameters of the absorbed thermal model are N_H , X-ray temperature (T_X), metal abundance normalized to solar (elemental ratios taken from Anders & Grevesse, 1989), and a normalization proportional to the integrated emission measure of the cluster. Results from the fitting are presented in Tables ?? and ???. No systematic error is

added during fitting, and thus all quoted errors are statistical only. The statistic used during fitting was χ^2 (XSPEC statistics package CHI). Every cluster analyzed was found to have greater than 1500 background-subtracted source counts in the spectrum.

For some clusters, more than one observation was available in the archive. We utilized the power of the combined exposure time by first extracting independent spectra, WARFs, WRMFs, normalized background spectra, and soft residuals for each observation. Then, these independent spectra were read into XSPEC simultaneously and fit with one spectral model which had all parameters, except normalization, tied among the spectra. The simultaneous fit is what is reported for these clusters, denoted by a star (\star), in Tables ?? and ??.

Additional statistical error was introduced into the fits because of uncertainty associated with the soft local background component discussed in §2.3.2. To estimate the sensitivity of our best-fit temperatures to this uncertainty, we used the differences between T_X for a model using the best-fit soft background normalization and T_X for models using $\pm 1\sigma$ of the soft background normalization. The statistical uncertainty of the original fit and the additional uncertainty inferred from the range of normalizations to the soft X-ray background component were then added in quadrature to produce a final error. In all cases this additional background error on the temperature was less than 10% of the total statistical error, and therefore represents a minor inflation of the error budget.

When comparing fits with fixed Galactic column density with those where it was a free parameter, we found that neither the goodness of fit per free parameter nor the best-fit T_X were significantly different. Thus, N_H was fixed at the Galactic value with the exception of three cases: Abell 399 (Sakelliou & Ponman, 2004), Abell 520, and Hercules A. For these three clusters N_H is a free parameter. In all fits, the metal abundance was a free parameter.

After fitting we rejected several data sets as their best-fit $T_{2.0-7.0}$ had no upper bound in the 90% confidence interval and thus were insufficient for our analysis. All fits for the clusters Abell 781, Abell 1682, CL J1213+0253, CL J1641+4001, IRAS 09104+4109, Lynx E, MACS J1824.3+4309, MS 0302.7+1658, and RX J1053+5735 were rejected. We also removed Abell 2550 from our sample after finding it to be an anomalously cool ($T_X \sim 2$ keV) “cluster”. In fact, Abell 2550 is a line-of-sight set of groups, as discussed by Martini et al. (2004). After these rejections, we are left with a final sample of 192 clusters which have R_{2500} -CORE fits and 166 clusters which have R_{5000} -CORE fits.

2.5.2 SIMULATED SPECTRA

To quantify the effect a second, cooler gas component would have on the fit of a single-component spectral model, we created an ensemble of simulated spectra for each real spectrum in our entire sample using XSPEC. With these simulated spectra we sought to answer the question: Given the count level in each observation of our sample, how bright must a second temperature component be for it to affect the observed temperature ratio? Put another way, we asked at what flux ratio a second gas phase produces a temperature ratio, T_{HBR} , of greater than unity with 90% confidence.

We began by adding the observation-specific background to a convolved, absorbed thermal model with two temperature components observed for a time period equal to the actual observation’s exposure time and adding Poisson noise. For each realization of an observation’s simulated spectrum, we defined the primary component to have the best-fit temperature and metallicity of the R_{2500} -CORE 0.7-7.0 keV fit, or R_{5000} -CORE if no R_{2500} -CORE fit was performed. We then incremented the secondary component temperature over the values 0.5, 0.75, 1.0, 2.0, and 3.0 keV. The metallicity of the secondary component was fixed and set equal to the metallicity of

the primary component.

We adjusted the normalization of the simulated two-component spectra to achieve equivalent count rates to those in the real spectra. The sum of normalizations can be expressed as $N = N_1 + \xi N_2$. We set the secondary component normalization to $N_2 = \xi N_{bf}$ where N_{bf} is the best-fit normalization of the appropriate 0.7-7.0 keV fit and ξ is a preset factor taking the values 0.4, 0.3, 0.2, 0.15, 0.1, and 0.05. The primary component normalization, N_1 , was determined through an iterative process to make real and simulated spectral count rates match. The parameter ξ therefore represents the fractional contribution of the cooler component to the overall count rate.

There are many systematics at work in the full ensemble of observation specific simulated spectra, such as redshift, column density, and metal abundance. Thus as a further check of spectral sensitivity to the presence of a second gas phase, we simulated additional spectra for the case of an idealized observation. We followed a similar procedure to that outlined above, but in this instance we used a finer temperature and ξ grid of $T_2 = 0.5 \rightarrow 3.0$ in steps of 0.25 keV, and $\xi = 0.02 \rightarrow 0.4$ in steps of 0.02. The input spectral model was $N_H = 3.0 \times 10^{20} \text{ cm}^{-2}$, $T_1 = 5 \text{ keV}$, $Z/Z_\odot = 0.3$ and $z = 0.1$. We also varied the exposure times such that the total number of counts in the 0.7-7.0 keV band was 15K, 30K, 60K, or 120K. For these spectra we used the on-axis sample response files provided to Cycle 10 proposers⁴. Poisson noise is added, but no background is considered.

We also simulated a control sample of single-temperature models. The control sample is simply a simulated version of the best-fit model. This control provides us with a statistical test of how often the actual hard-component temperature might differ from a broadband temperature fit if calibration effects are under control. Fits for the control sample are shown in the far right panels of Figure 2.3.

⁴http://cxc.harvard.edu/caldb/prop_plan/imaging/index.html

For each observation, we have 65 total simulated spectra: 35 single-temperature control spectra and 30 two-component simulated spectra (5 secondary temperatures, each with six different ξ). Our resulting ensemble of simulated spectra contains 12,765 spectra. After generating all the spectra we followed the same fitting routine detailed in §2.5.1.

With the ensemble of simulated spectra we then asked the question: for each T_2 and ΔT_X (defined as the difference between the primary and secondary temperature components) what is the minimum value of ξ , called ξ_{min} , that produces $T_{HBR} \geq 1.1$ at 90% confidence? From our analysis of these simulated spectra we have found these important results:

1. In the control sample, a single-temperature model rarely ($\sim 2\%$ of the time) gives a significantly different $T_{0.7-7.0}$ and $T_{2.0-7.0}$. The weighted average (Fig. 2.3, right panels) for the control sample is 1.002 ± 0.001 and the standard deviation is ± 0.044 . The T_{HBR} distribution for the control sample appears to have an intrinsic width which is likely associated with statistical noise of fitting in XSPEC (Dupke, private communication). This result indicates that our remaining set of observations is statistically sound, *e.g.* our finding that T_{HBR} significantly differs from 1.0 cannot result from statistical fluctuations alone.
2. Shown in Table 2.1 are the contributions a second cooler component must make in the case of the idealized spectra in order to produce $T_{HBR} \geq 1.1$ at 90% confidence. In general, the contribution of cooler gas must be $> 10\%$ for $T_2 < 2$ keV to produce T_{HBR} as large as 1.1. The increase in percentages at $T_2 < 1.0$ keV is owing to the energy band we consider (0.7-7.0 keV) as gas cooler than 0.7 keV must be brighter than at 1.0 keV in order to make an equivalent contribution to the soft end of the spectrum at 0.7 keV.
3. In the full ensemble of observation-specific simulated spectra, we find a great

deal of statistical scatter in ξ_{min} at any given ΔT_X . This was expected as the full ensemble is a superposition of spectra with a broad range of total counts, N_H , redshifts, abundance, and backgrounds. But using the idealized simulated spectra as a guide, we find for those spectra with $N_{\text{counts}} \gtrsim 15000$, producing $T_{HBR} \geq 1.1$ at 90% confidence again requires the cooler gas to be contributing $> 10\%$ of the emission. These results are also summarized in Table 2.1. The good agreement between the idealized and observation-specific simulated spectra indicates that while many more factors are in play for the observation-specific spectra, they do not degrade our ability to reliably measure $T_{HBR} > 1.1$. The trend here of a common soft component sufficient to change the temperature measurement in a single-temperature model is statistical, a result that comes from an aggregate view of the sample rather than any individual fit.

4. As redshift increases, gas cooler than 1.0 keV is slowly redshifted out of the observable X-ray band. As expected, we find from our simulated spectra that for $z \geq 0.6$, T_{HBR} is no longer statistically distinguishable from unity. In addition, the $T_{2.0-7.0}$ lower boundary nears convergence with the $T_{0.7-7.0}$ lower boundary as z increases, and for $z = 0.6$, the hard-band lower limit is 1.25 keV, while at the highest redshift considered, $z = 1.2$, the hard-band lower limit is only 0.91 keV. For the 14 clusters with $z \geq 0.6$ in our real sample we are most likely underestimating the actual amount of temperature inhomogeneity. We have tested the effect of excluding these clusters on our results, and find a negligible change in the overall skew of T_{HBR} to greater than unity.

Table 2.1: Summary of two-component simulations

T_2 keV	ξ_{min}	T_2 keV	ξ_{min}
Idealized Spectra		Observation-Specific Spectra	
0.50	$\geq 12\% \pm 4\%$	0.50	$\geq 14.5\% \pm 0.1\%$
0.75	$\geq 12\% \pm 4\%$	0.75	$\geq 11.7\% \pm 0.1\%$
1.00	$\geq 8\% \pm 3\%$	1.00	$\geq 11.6\% \pm 0.1\%$
1.25	$\geq 17\% \pm 3\%$
1.50	$\geq 23\% \pm 5\%$
1.75	$\geq 28\% \pm 4\%$
2.00	none	2.00	$\geq 25.5\% \pm 0.1\%$
3.00	none	3.00	$\geq 28.9\% \pm 0.1\%$

Table 2.1 summarizes the results of the two temperature component spectra simulations for the ideal and observation-specific cases (see §2.5.2 for details). The parameter ξ_{min} represents the minimum fractional contribution of the cooler component, T_2 , to the overall count rate in order to produce $T_{HBR} \geq 1.1$ at 90% confidence. The results for the observation-specific spectra are for spectra with $N_{counts} > 15,000$.

2.6 RESULTS AND DISCUSSION

2.6.1 TEMPERATURE RATIOS

For each cluster we have measured a ratio of the hard-band to broadband temperature defined as $T_{HBR} = T_{2.0-7.0}/T_{0.7-7.0}$. We find that the mean T_{HBR} for our entire sample is greater than unity at more than 12σ significance. The weighted mean values for our sample are shown in Table 2.2. Quoted errors in Table 2.2 are standard deviation of the mean calculated using an unbiased estimator for weighted samples. Simulated sample has been culled to include only $T_2=0.75$ keV. Presented in Figure 2.3 are the binned weighted means and raw T_{HBR} values for $R_{2500-}\text{CORE}$, $R_{5000-}\text{CORE}$, and the simulated control sample. The peculiar points with $T_{HBR} < 1$ are all statistically consistent with unity. The presence of clusters with $T_{HBR} =$

1 suggests that systematic calibration uncertainties are not the sole reason for deviations of T_{HBR} from 1. We also find that the temperature ratio does not depend on the best-fit broadband temperature, and that the observed dispersion of T_{HBR} is greater than the predicted dispersion arising from systematic uncertainties.

The uncertainty associated with each value of T_{HBR} is dominated by the larger error in $T_{2.0-7.0}$, and on average, $\Delta T_{2.0-7.0} \approx 2.3\Delta T_{0.7-7.0}$. This error interval discrepancy naturally results from excluding the bulk of a cluster’s emission which occurs below 2 keV. While choosing a temperature-sensitive cut-off energy for the hard-band (other than 2.0 keV) might maintain a more consistent error budget across our sample, we do not find any systematic trend in T_{HBR} or the associated errors with cluster temperature.

Table 2.2: Weighted averages for various apertures

Aperture	[0.7-7.0]	[2.0-7.0]	T_{HBR}	[0.7-7.0]	[2.0-7.0]	T_{HBR}
	keV	keV		keV	keV	
Aperture	Without Core				With Core	
R ₂₅₀₀	4.93±0.03	6.24±0.07	1.16±0.01	4.47±0.02	5.45±0.05	1.13±0.01
R ₅₀₀₀	4.75±0.02	5.97±0.07	1.14±0.01	4.27±0.02	5.29±0.05	1.14±0.01
Simulated	3.853±0.004	4.457±0.009	1.131±0.002
Control	4.208±0.003	4.468±0.006	1.002±0.001

2.6.2 SYSTEMATICS

In this study we have found the average value of T_{HBR} is significantly greater than one and that $\sigma_{HBR} > \sigma_{control}$, with the latter result being robust against systematic uncertainties. As predicted by ME01, both of these results are expected to arise naturally from the hierarchical formation of clusters. But systematic uncertainty related to *Chandra* instrumentation or other sources could shift the average value of T_{HBR} one would get from “perfect” data. In this section we consider some additional sources of uncertainty.

5A First, the disagreement between *XMM-Newton*

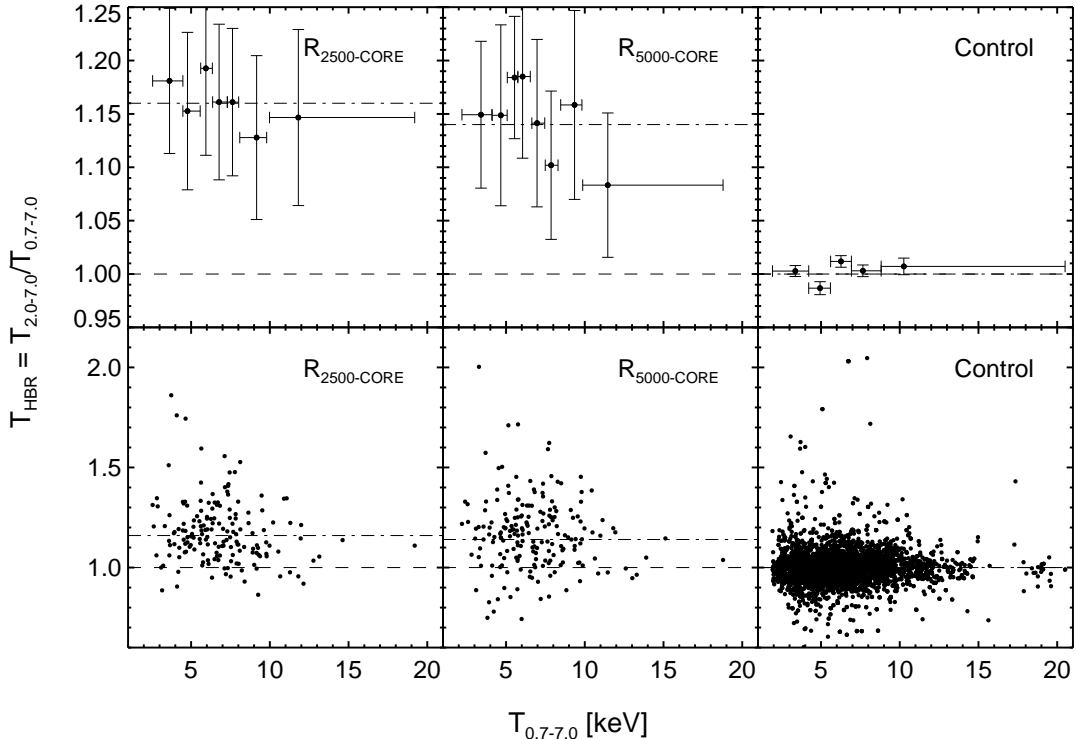


Figure 2.3 Best-fit temperatures for the hard-band, $T_{2.0-7.0}$, divided by the broadband, $T_{0.7-7.0}$, and plotted against the broadband temperature. For binned data, each bin contains 25 clusters, with the exception of the highest temperature bins which contain 16 and 17 for $R_{2500\text{-CORE}}$ and $R_{5000\text{-CORE}}$, respectively. The simulated data bins contain 1000 clusters with the last bin having 780 clusters. The line of equality is shown as a dashed line and the weighted mean for the full sample is shown as a dashed-dotted line. Error bars are omitted in the unbinned data for clarity. Note the net skewing of T_{HBR} to greater than unity for both apertures with no such trend existing in the simulated data. The dispersion of T_{HBR} for the real data is also much larger than the dispersion of the simulated data.

and *Chandra* cluster temperatures has been noted in several independent studies, i.e. Vikhlinin et al. (2005) and Snowden et al. (2008). But the source of this discrepancy is not well understood and efforts to perform cross-calibration between *XMM-Newton* and *Chandra* have thus far not been conclusive. One possible explanation is poor calibration of *Chandra* at soft X-ray energies which may arise from a hydrocarbon contaminant on the High Resolution Mirror Assembly (HRMA) similar in nature to the contaminant on the ACIS detectors (Marshall et al., 2004). We have assessed this possibility by looking for systematic trends in T_{HBR} with time or temperature, as such a contaminant would most likely have a temperature and/or time dependence.

As noted in §2.6.1 and seen in Figure 2.3, we find no systematic trend with temperature either for the full sample or for a sub-sample of single-observation clusters with $> 75\%$ of the observed flux attributable to the source (higher S/N observations will be more affected by calibration uncertainty). Plotted in the lower-left pane of Figures 2.4 and 2.5 is T_{HBR} versus time for single observation clusters (clusters with multiple observations are fit simultaneously and any time effect would be washed out) where the spectral flux is $> 75\%$ from the source. We find no significant systematic trend in T_{HBR} with time, which suggests that if T_{HBR} is affected by any contamination of *Chandra*'s HRMA, then the contaminant is most likely not changing with time. Our conclusion on this matter is that the soft calibration uncertainty is not playing a dominant role in our results.

Aside from instrumental and calibration effects, some other possible sources of systematic error are S/N, redshift selection, Galactic absorption, and metallicity. Also presented in Figures 2.4 and 2.5 are three of these parameters versus T_{HBR} for $R_{2500-{\rm CORE}}$ and $R_{5000-{\rm CORE}}$, respectively. The trend in T_{HBR} with redshift is expected as the $2.0/(1+z)$ keV hard-band lower boundary nears convergence with the 0.7 keV broadband lower boundary at $z \approx 1.85$. We find no systematic trends of T_{HBR} with S/N or Galactic absorption, which might occur if the skew in T_{HBR}

were a consequence of poor count statistics, inaccurate Galactic absorption, or very poor calibration. In addition, the ratio of T_{HBR} for $R_{2500\text{--CORE}}$ to $R_{5000\text{--CORE}}$ for every cluster in our sample does not significantly deviate from unity. Our results are robust to changes in aperture size.

Also shown in Figures 2.4 and 2.5 are the ratios of *ASCA* temperatures taken from Horner (2001) to *Chandra* temperatures derived in this work. The spurious point below 0.5 with very large error bars is MS 2053.7-0449, which has a poorly constrained *ASCA* temperature of $10.03^{+8.73}_{-3.52}$. Our value of ~ 3.5 keV for this cluster is in agreement with the recent work of Maughan et al. (2008). Not all our sample clusters have an *ASCA* temperature, but a sufficient number (53) are available to make this comparison reliable. Apertures used in the extraction of *ASCA* spectra had no core region removed and were substantially larger than R_{2500} . *ASCA* spectra were also fit over a broader energy range (0.6-10 keV) than we use here. Nonetheless, our temperatures are in good agreement with those from *ASCA*, but we do note a trend of comparatively hotter *Chandra* temperatures for $T_{Chandra} > 10$ keV. For both apertures, the clusters with $T_{Chandra} > 10$ keV are Abell 1758, Abell 2163, Abell 2255, and RX J1347.5-1145. Based on this trend, we test excluding the hottest clusters ($T_{Chandra} > 10$ keV where *ASCA* and *Chandra* disagree) from our sample. The mean temperature ratio for $R_{2500\text{--CORE}}$ remains 1.16 and the error of the mean increases from ± 0.014 to ± 0.015 , while for $R_{5000\text{--CORE}}$ T_{HBR} increases by a negligible 0.9% to 1.15 ± 0.014 . Our results are not being influenced by the inclusion of hot clusters.

The temperature range of the clusters we have analyzed ($T_X \sim 3 - 20$ keV) is broad enough that the effect of metal abundance on the inferred spectral temperature is clearly not negligible. In Figure 2.6 we have plotted T_{HBR} versus abundance in solar units. Despite covering a factor of seven in temperature and metal abundances ranging from $Z/Z_\odot \approx 0$ to solar, we find no trend in T_{HBR} with metallicity. The

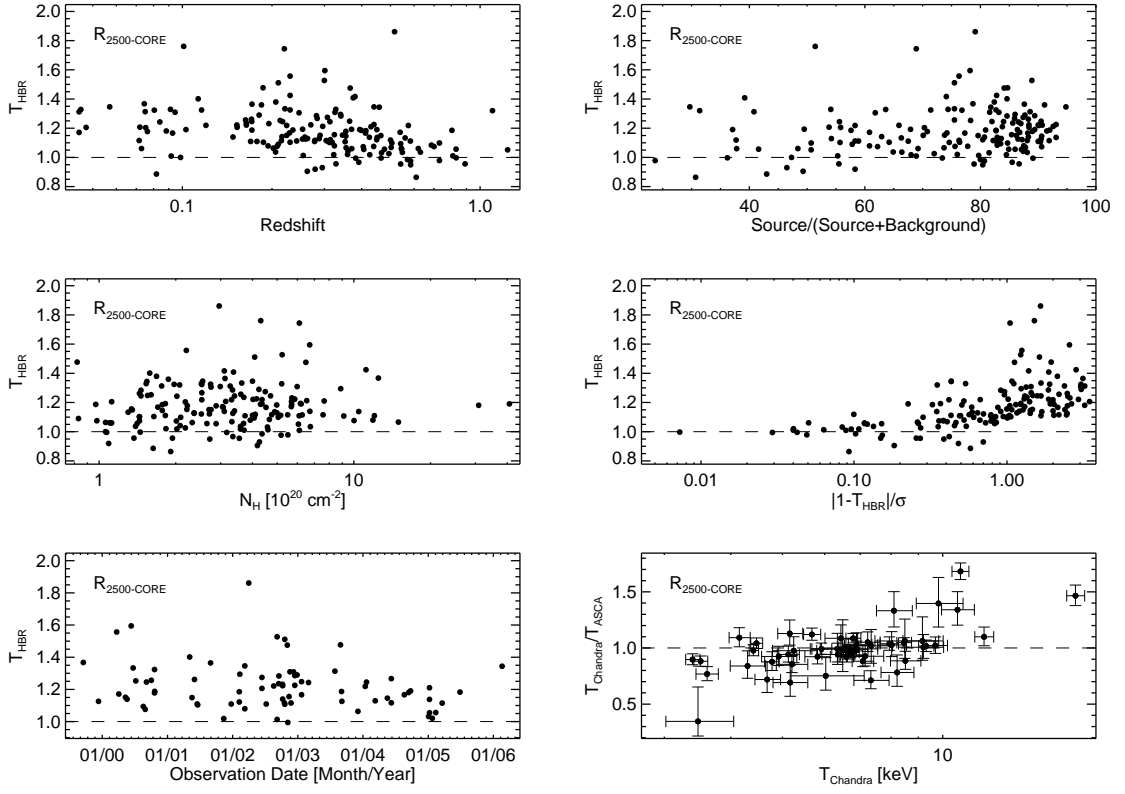


Figure 2.4 A few possible sources of systematic uncertainty vs. T_{HBR} calculated for the R_{2500} -CORE apertures (192 clusters). Error bars have been omitted in several plots for clarity. The line of equality is shown as a dashed line in all panels. (**Top left:**) T_{HBR} vs. redshift for the entire sample. The trend in T_{HBR} with redshift is expected as the $T_{2.0-7.0}$ lower boundary nears convergence with the $T_{0.7-7.0}$ lower boundary at $z \approx 1.85$. Weighted values of T_{HBR} are consistent with unity starting at $z \sim 0.6$. (**Top right:**) T_{HBR} vs. percentage of spectrum flux which is attributed to the source. We find no trend with signal-to-noise which suggests calibration uncertainty not is playing a major role in our results. (**Middle left:**) T_{HBR} vs. Galactic column density. We find no trend in absorption which would result if N_H values are inaccurate or if we had improperly accounted for local soft contamination. (**Middle right:**) T_{HBR} vs. the deviation from unity in units of measurement uncertainty. Recall that we have used 90% confidence (1.6σ) for our analysis. (**Bottom left:**) T_{HBR} plotted vs. observation start date. The plotted points are culled from the full sample and represent only clusters which have a single observation and where the spectral flux is $> 75\%$ from the source. We note no systematic trend with time. (**Bottom right:**) Ratio of *Chandra* temperatures derived in this work to *ASCA* temperatures taken from Horner (2001). We note a trend of comparatively hotter *Chandra* temperatures for clusters > 10 keV, otherwise our derived temperatures are in good agreement with those of *ASCA*.

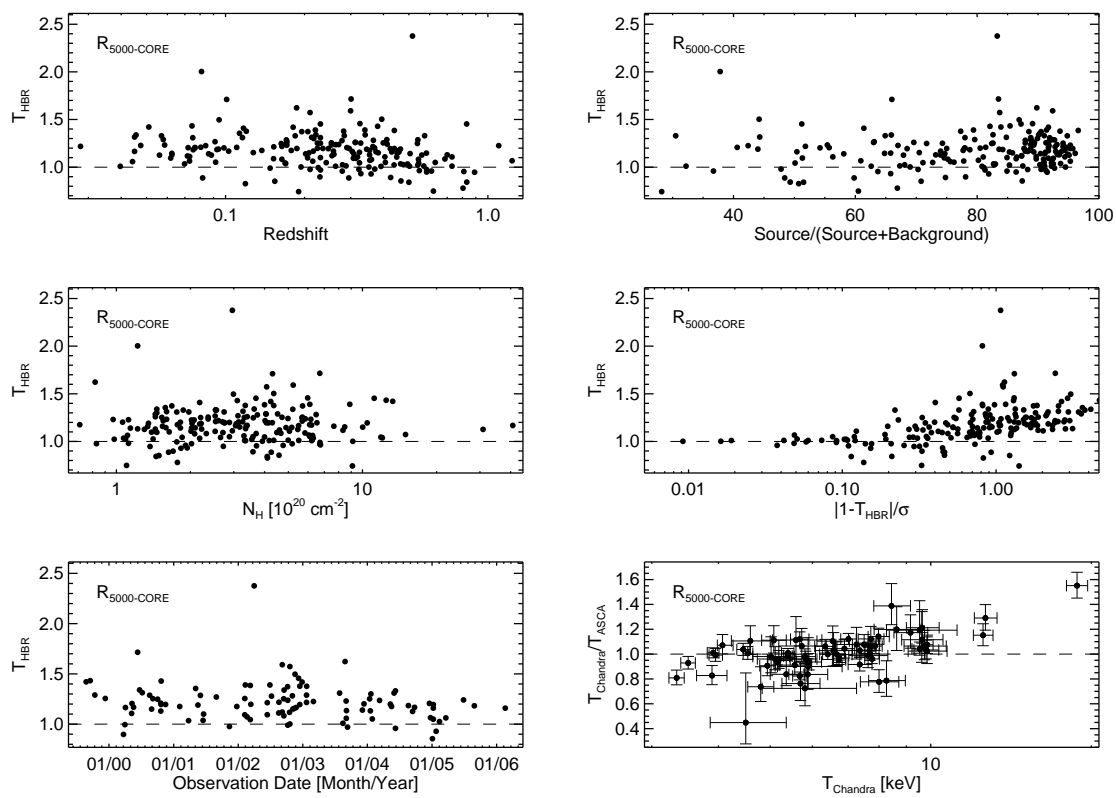


Figure 2.5 Same as Fig. 2.4 except using the $R_{5000\text{-CORE}}$ apertures (166 clusters).

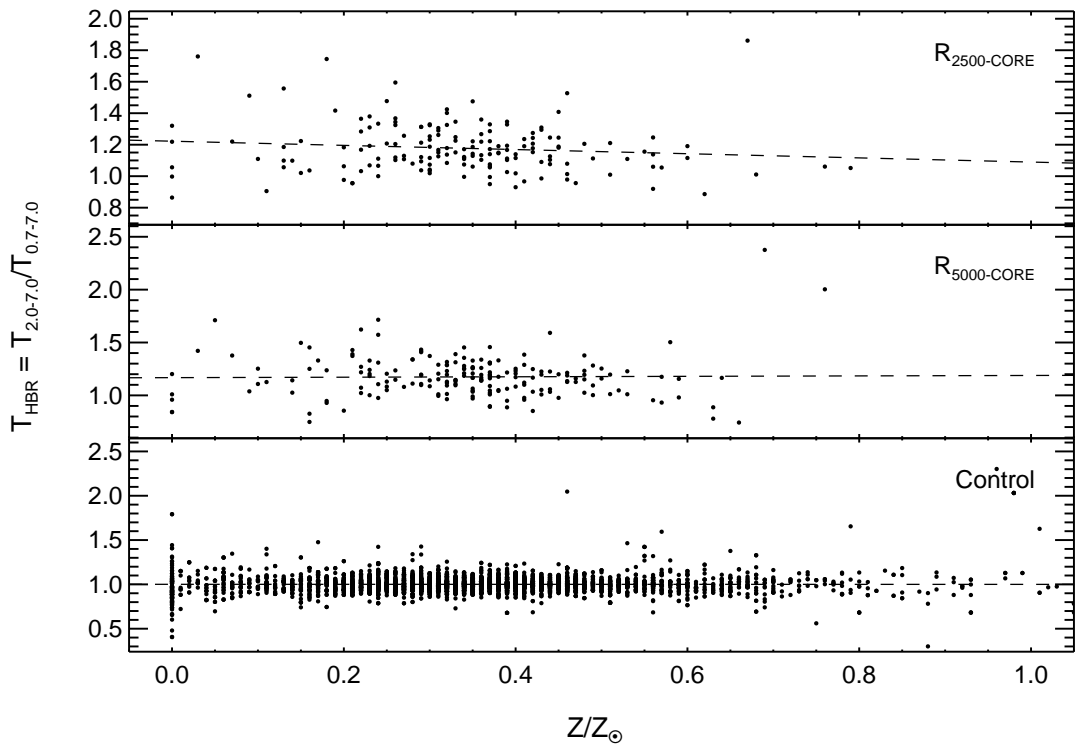


Figure 2.6 T_{HBR} as a function of metal abundance for $R_{2500\text{-CORE}}$, $R_{5000\text{-CORE}}$, and the control sample (see discussion of control sample in §2.5.2). Error bars are omitted for clarity. The dashed-line represents the linear best-fit using the bivariate correlated error and intrinsic scatter (BCES) method of Akritas & Bershady (1996) which takes into consideration errors on both T_{HBR} and abundance when performing the fit. We note no trend in T_{HBR} with metallicity (the apparent trend in the top panel is not significant) and also note the low dispersion in the control sample relative to the observations. The striation of abundance arises from our use of two decimal places in recording the best-fit values from XSPEC.

slight trend in the R_{2500} -CORE aperture (Fig. 2.6, top) is insignificant, while there is no trend at all in the control sample or R_{5000} -CORE aperture.

2.6.3 USING T_{HBR} AS A TEST OF RELAXATION

COOL CORE VERSUS NON-COOL CORE

As discussed in 2.1, ME01 gives us reason to believe the observed skewing of T_{HBR} to greater than unity is related to the dynamical state of a cluster. It has also been suggested that the process of cluster formation and relaxation may robustly result in the formation of a cool core (Ota et al., 2006; Burns et al., 2008). Depending on classification criteria, completeness, and possible selection biases, studies of flux-limited surveys have placed the prevalence of cool cores at 34% – 60% (White et al., 1997; Peres et al., 1998; Bauer et al., 2005; Chen et al., 2007). It has thus become rather common to divide up the cluster population into two distinct classes, cool core (CC) and non-cool core (NCC), for the purpose of discussing their different formation or merger histories. We thus sought to identify which clusters in our sample have cool cores, which do not, and if the presence or absence of a cool core is correlated with T_{HBR} . It is very important to recall that we excluded the core during spectral extraction and analysis.

To classify the core of each cluster, we extracted a spectrum for the 50 kpc region surrounding the cluster center and then defined a temperature decrement,

$$T_{\text{dec}} = T_{50}/T_{\text{cluster}} \quad (2.3)$$

where T_{50} is the temperature of the inner 50 kpc and T_{cluster} is either the R_{2500} -CORE or R_{5000} -CORE temperature. If T_{dec} was 2σ less than unity, we defined the cluster as having a CC, otherwise the cluster was defined as NCC. We find CCs in 35% of our sample and when we lessen the significance needed for CC classification from 2σ

to 1σ , we find 46% of our sample clusters have CCs. It is important to note that the frequency of CCs in our study is consistent with other more detailed studies of CC/NCC populations.

When fitting for T_{50} , we altered the method outlined in §2.5.1 to use the XSPEC modified Cash statistic (Cash, 1979), CSTAT, on ungrouped spectra. This choice was made because the distribution of counts per bin in low count spectra is not Gaussian but instead Poisson. As a result, the best-fit temperature using χ^2 is typically cooler (Nousek & Shue, 1989; Balestra et al., 2007). We have explored this systematic in *all* of our fits and found it to be significant only in the lowest count spectra of the inner 50 kpc apertures discussed here. But, for consistency, we fit all inner 50 kpc spectra using the modified Cash statistic.

With each cluster core classified, we then took cuts in T_{HBR} and asked how many CC and NCC clusters were above these cuts. Figure 2.7 shows the normalized number of CC and NCC clusters as a function of cuts in T_{HBR} . If T_{HBR} were insensitive to the state of the cluster core, we expect, for normally distributed T_{HBR} values, to see the number of CC and NCC clusters decreasing in the same way. However, the number of CC clusters falls off more rapidly than the number of NCC clusters. If the presence of a CC is indicative of a cluster’s advancement towards complete virialization, then the significantly steeper decline in the percent of CC clusters versus NCC as a function of increasing T_{HBR} indicates higher values of T_{HBR} are associated with a less relaxed state. This result is insensitive to our choice of significance level in the core classification, i.e. the result is the same whether using 1σ or 2σ significance when considering T_{dec} .

Because of the CC/NCC definition we selected, our identification of CCs and NCCs was only as robust as the errors on T_{50} allowed. One can thus ask the question, did our definition bias us towards finding more NCCs than CCs? To explore this question we simulated 20 spectra for each observation following the method outlined

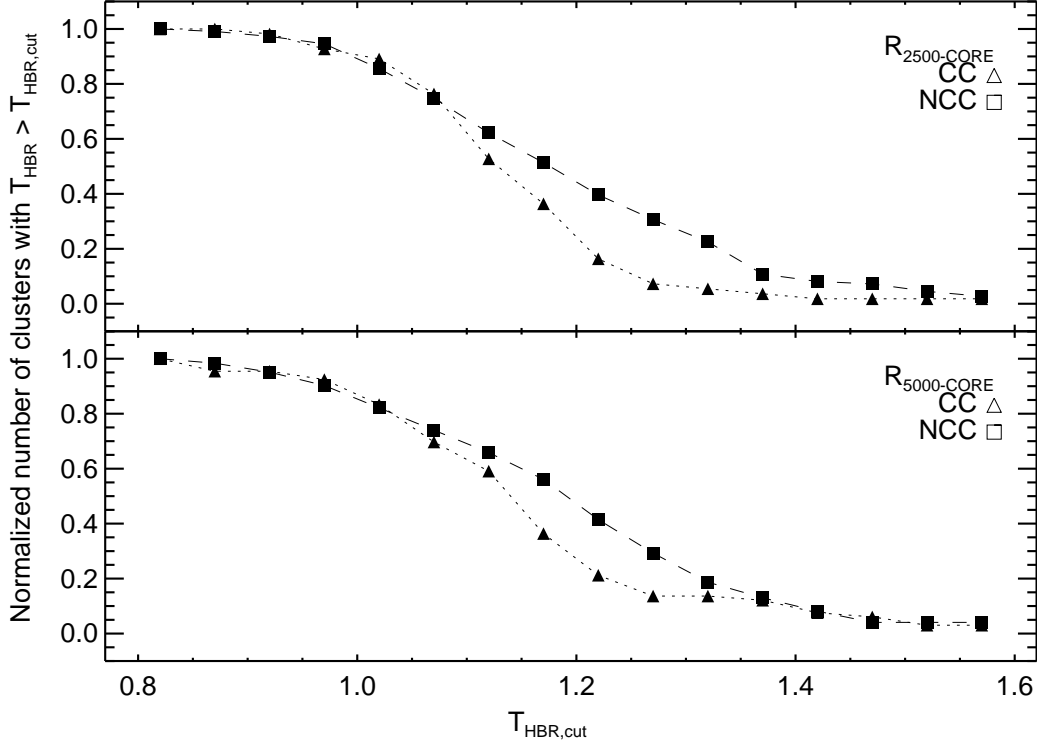


Figure 2.7 Normalized number of CC and NCC clusters as a function of cuts in T_{HBR} . There are 192 clusters plotted in the top panel and 166 in the bottom panel. We have defined a cluster as having a CC when the temperature for the 50 kpc region around the cluster center divided by the temperature for $R_{2500-\text{CORE}}$, or $R_{5000-\text{CORE}}$, was less than one at the 2σ level. We then take cuts in T_{HBR} at the 1σ level and ask how many CC and NCC clusters are above these cuts. The number of CC clusters falls off more rapidly than NCC clusters in this classification scheme suggesting higher values of T_{HBR} prefer less relaxed systems which do not have cool cores. This result is insensitive to our choice of significance level in both the core classification and T_{HBR} cuts.

in §2.5.2 for the control sample but using the inner 50 kpc spectral best-fit values as input. For each simulated spectrum, we calculated a temperature decrement (eq. 2.3) and re-classified the cluster as having a CC or NCC. Using the new set of mock classifications we assigned a reliability factor, ψ , to each real classification, which is simply the fraction of mock classifications which agree with the real classification. A value of $\psi = 1.0$ indicates complete agreement, with $\psi = 0.0$ indicating no agreement. When we removed clusters with $\psi < 0.9$ and repeated the analysis above, we found no significant change in the trend of a steeper decrease in the relative number of CC versus NCC clusters as a function of T_{HBR} .

Recall that the coolest ICM gas is being redshifted out of the observable band as z increases and becomes a significant effect at $z \geq 0.6$ (§2.5.2). Thus, we are likely not detecting “weak” CCs in the highest redshift clusters of our sample and consequently these cores are classified as NCCs and are artificially increasing the NCC population. When we excluded the 14 clusters at $z \geq 0.6$ from this portion of our analysis and repeated the calculations, we found no significant change in the results.

MERGERS VERSUS NONMERGERS

Looking for a correlation between cluster relaxation and a skewing in T_{HBR} was the primary catalyst of this work. The result that increasing values of T_{HBR} are more likely to be associated with clusters harboring non-cool cores gives weight to that hypothesis. But, the simplest relation to investigate is if T_{HBR} is preferentially higher in merger systems. Thus, we now discuss clusters with the highest significant values of T_{HBR} and attempt to establish, via literature based results, the dynamic state of these systems.

The subsample of clusters on which we focus have a $T_{HBR} > 1.1$ at 90% confidence for both their $R_{2500\text{--CORE}}$ and $R_{5000\text{--CORE}}$ apertures. These clusters are listed in Table ?? and are sorted by the lower limit of T_{HBR} . Shown in Figure 2.8 is a plot

of T_{HBR} versus $T_{0.7-7.0}$ for all the clusters in our sample. The clusters discussed in this section are shown as green triangles and black stars. The clusters with only a R_{5000} -CORE analysis are listed separately at the bottom of the table. All 33 clusters listed have a core classification of $\psi > 0.9$ (see §2.6.3). The choice of the $T_{HBR} > 1.1$ threshold was arbitrary and intended to limit the number of clusters to which we pay individual attention, but which is still representative of mid- to high- T_{HBR} values. Only two clusters – Abell 697 and MACS J2049.9-3217 – do not have a $T_{HBR} > 1.1$ in one aperture and not the other. In both cases although, this was the result of the lower boundary narrowly missing the cut, but both clusters still have T_{HBR} significantly greater than unity.

For those clusters which have been individually studied, they are listed as mergers based on the conclusions of the literature authors (cited in Table ??). Many different techniques were used to determine if a system is a merger: bimodal galaxy velocity distributions, morphologies, highly asymmetric temperature distributions, ICM substructure correlated with subclusters, or disagreement of X-ray and lensing masses. From Table ?? we can see clusters exhibiting the highest significant values of T_{HBR} tend to be ongoing or recent mergers. At the 2σ level, we find increasing values of T_{HBR} favor merger systems with NCCs over relaxed, CC clusters. It appears mergers have left a spectroscopic imprint on the ICM which was predicted by ME01 and which we observe in our sample.

Of the 33 clusters with T_{HBR} significantly > 1.1 , only 7 have CCs. Three of those – MKW3S, 3C 28.0, and RX J1720.1+2638 – have their apertures centered on the bright, dense cores in confirmed mergers. Two more clusters – Abell 2384 and RX J1525+0958 – while not confirmed mergers, have morphologies which are consistent with powerful ongoing mergers. Abell 2384 has a long gas tail extending toward a gaseous clump which we assume has recently passed through the cluster. RXJ1525 has a core shaped like a rounded arrowhead and is reminiscent of the bow shock

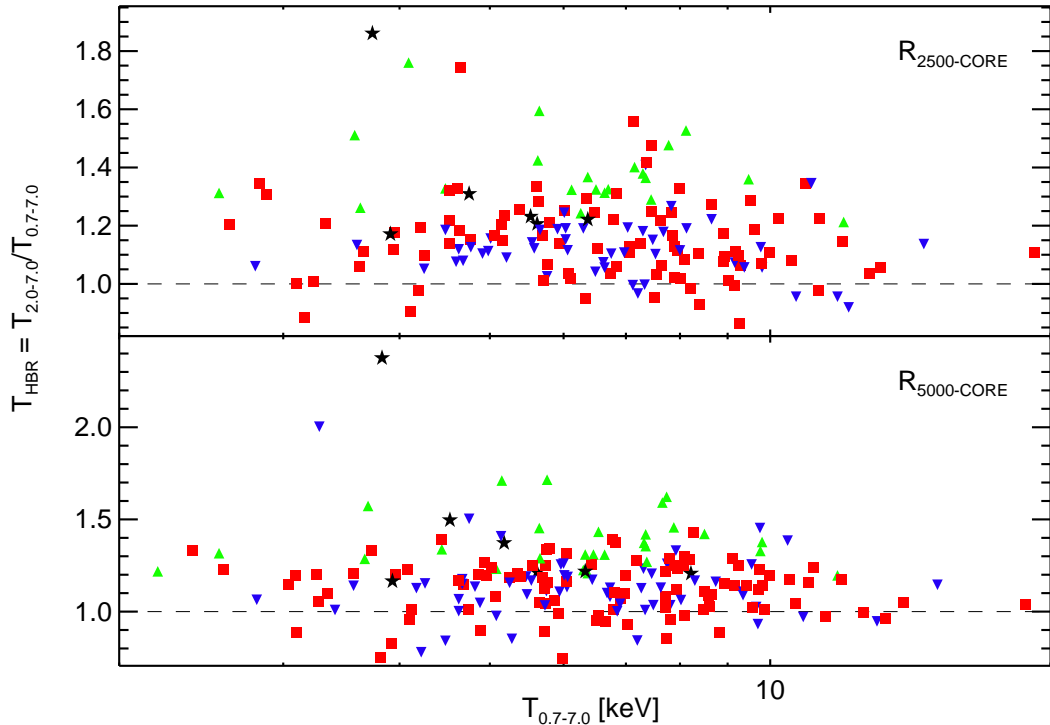


Figure 2.8 T_{HBR} plotted against $T_{0.7-7.0}$ for the $R_{2500\text{-CORE}}$ and $R_{5000\text{-CORE}}$ apertures. Note that the vertical scales for both panels are not the same. The top and bottom panels contain 192 and 166 clusters, respectively. Only two clusters – Abell 697 and MACS J2049.9-3217 – do not have a $T_{HBR} > 1.1$ in one aperture and not the other. In both cases however, it was a result of narrowly missing the cut. The dashed lines are the lines of equivalence. Symbols and color coding are based on two criteria: (1) the presence of a CC and (2) the value of T_{HBR} . Black stars (6 in the top panel; 7 in the bottom) are clusters with a CC and T_{HBR} significantly greater than 1.1. Green upright-triangles (21 in the top; 27 in the bottom) are NCC clusters with T_{HBR} significantly greater than 1.1. Blue down-facing triangles (49 top; 60 bottom) are CC clusters and red squares (90 top; 98 bottom) are NCC clusters. We have found most, if not all, of the clusters with $T_{HBR} \gtrsim 1.1$ are merger systems. Note that the cut at $T_{HBR} > 1.1$ is arbitrary and there are more merger systems in our sample than just those highlighted in this figure. However it is rather suggestive that clusters with the highest values of T_{HBR} appear to be merging systems.

seen in 1E0657-56. Abell 907 has no signs of being a merger system, but the highly compressed surface brightness contours to the west of the core are indicative of a prominent cold front, a tell-tale signature of a subcluster merger event (Markevitch & Vikhlinin, 2007). Abell 2029 presents a very interesting and curious case because of its seemingly high state of relaxation and prominent cool core. There are no complementary indications it has experienced a merger event. Yet its core hosts a wide-angle tail radio source. It has been suggested that such sources might be attributable to cluster merger activity (Sakelliou & Merrifield, 2000). Moreover, the X-ray isophotes to the west of the bright, peaked core are slightly more compressed and may be an indication of past gas sloshing resulting from the merger of a small subcluster. Both of these features have been noted previously, specifically by Clarke et al. (2004, 2005). We suggest the elevated T_{HBR} value for this cluster lends more weight to the argument that A2029 has indeed experienced a merger recently, but how long ago we do not know.

The remaining systems we could not verify as mergers – RX J0439.0+0715, MACS J2243.3-0935, MACS J0547.0-3904, Zwicky 1215, MACS J2311+0338, Abell 267, and NGC 6338 – have NCCs and X-ray morphologies consistent with an ongoing or post-merger scenario. Abell 1204 shows no signs of recent or ongoing merger activity; however, it resides at the bottom of the arbitrary T_{HBR} cut, and as evidenced by Abell 401 and Abell 1689, exceptional spherical symmetry is no guarantee of relaxation. Our analysis here is partially at the mercy of morphological assessment, and only a more stringent study of a carefully selected subsample or analysis of simulated clusters can better determine how closely correlated T_{HBR} is with the timeline of merger events.

2.7 SUMMARY AND CONCLUSIONS

We have explored the band dependence of the inferred X-ray temperature of the ICM for 166 well-observed ($N_{counts} > 1500$) clusters of galaxies selected from the *Chandra*

Data Archive.

We extracted spectra from the annulus between $R = 70$ kpc and $R = R_{2500}, R_{5000}$ for each cluster. We compared the X-ray temperatures inferred for single-component fits to global spectra when the energy range of the fit was 0.7-7.0 keV (broad) and when the energy range was $2.0/(1+z)$ -7.0 keV (hard). We found that, on average, the hard-band temperature is significantly higher than the broadband temperature. For the R_{2500} -CORE aperture we measured a weighted average of $T_{HBR} = 1.16$ with $\sigma = \pm 0.10$ and $\sigma_{mean} = \pm 0.01$ for the R_{5000} -CORE aperture, and $T_{HBR} = 1.14$ with $\sigma = \pm 0.12$ and $\sigma_{mean} = \pm 0.01$. We also found no systematic trends in the value of T_{HBR} , or the dispersion of T_{HBR} , with S/N, redshift, Galactic absorption, metallicity, observation date, or broadband temperature.

In addition, we simulated an ensemble of 12,765 spectra which contained observation-specific and idealized two-temperature component models, plus a control sample of single-temperature models. From analysis of these simulations we found the statistical fluctuations for a single temperature model are inadequate to explain the significantly different $T_{0.7-7.0}$ and $T_{2.0-7.0}$ we measure in our sample. We also found that the observed scatter, σ_{HBR} , is consistent with the presence of unresolved cool ($T_X < 2.0$ keV) gas contributing a minimum of $> 10\%$ of the total emission. The simulations also show the measured observational scatter in T_{HBR} is greater than the statistical scatter, $\sigma_{control}$. These results are consistent with the process of hierarchical cluster formation.

Upon further exploration, we found that T_{HBR} is enhanced preferentially for clusters which are known merger systems and for clusters without cool cores. Clusters with temperature decrements in their cores (known as cool-core clusters) tend to have best-fit hard-band temperatures that are consistently closer to their best-fit broadband temperatures. The correlation of T_{HBR} with the type of cluster core is insensitive to our choice of classification scheme and is robust against redshift effects.

Our results qualitatively support the finding by ME01 that the temperature ratio, T_{HBR} , might therefore be useful for statistically quantifying the degree of cluster relaxation/virialization.

An additional robust test of the ME01 finding should be made with simulations by tracking T_{HBR} during hierarchical assembly of a cluster. If T_{HBR} is tightly correlated with a cluster's degree of relaxation, then it, along with other methods of substructure measure, may provide a powerful metric for predicting (and therefore reducing) a cluster's deviation from mean mass-scaling relations. The task of reducing scatter in scaling relations will be very important if we are to reliably and accurately measure the mass of clusters.

2.8 ACKNOWLEDGMENTS

K. W. C. was supported in this work by the National Aeronautics and Space Administration through *Chandra* X-Ray Observatory Archive grants AR-6016X and AR-4017A, with additional support from a start-up grant for Megan Donahue from Michigan State University. M. D. and Michigan State University acknowledge support from the NASA LTSA program NNG-05GD82G. G. M. V. thanks NASA for support through theory grant NNG-04GI89G. The *Chandra* X-ray Observatory Center is operated by the Smithsonian Astrophysical Observatory for and on behalf of the National Aeronautics Space Administration under contract NAS8-03060. This research has made use of software provided by the *Chandra* X-ray Center (CXC) in the application packages CIAO, CHIPS, and SHERPA. We thank Alexey Vikhlinin for helpful insight and expert advice. K. W. C. also thanks attendees of the “Eight Years of Science with *Chandra* Calibration Workshop” for stimulating discussion regarding *XMM-Chandra* cross-calibration. K. W. C. especially thanks Keith Arnaud for personally providing support and advice for mastering XSPEC. This research has made use of the NASA/IPAC Extragalactic Database (NED), which is operated by the

Jet Propulsion Laboratory, California Institute of Technology, under contract with the National Aeronautics and Space Administration. This research has also made use of NASA's Astrophysics Data System. *ROSAT* data and software were obtained from the High Energy Astrophysics Science Archive Research Center (HEASARC), provided by NASA's Goddard Space Flight Center.

Chapter Three

Cavagnolo, Kenneth W., Donahue, Megan, Voit, G. Mark, Sun, Ming (2008). Chandra Archival Sample of Intraccluster Entropy Profiles. The Astrophysical Journal Supplement Series. 0:000-000.

NB: The text of this chapter has been submitted for publication, but has not been assigned a bibliographic code as of yet.

CHAPTER 3: INTRACLUSTER MEDIUM ENTROPY PROFILES FOR A CHANDRA ARCHIVAL SAMPLE OF GALAXY CLUSTERS

3.1 INTRODUCTION

The general process of galaxy cluster formation through hierarchical merging is well understood, but many details, such as the impact of feedback sources on the cluster environment and radiative cooling in the cluster core, are not. The nature of feedback operating within clusters is of great interest because of the implications for better understanding massive galaxy formation and using mass-observable scaling relations in cluster cosmological studies. Early models of structure formation which included only gravitation predicted self-similarity among the galaxy cluster population. That is to say, the physical properties of galaxy clusters, such as temperature and luminosity, scaled with cluster redshift and mass (Kaiser, 1986; Evrard & Henry, 1991; Navarro et al., 1995, 1997; Evrard et al., 1996; Evrard, 1997; Teyssier et al., 1997; Eke et al., 1998; Bryan & Norman, 1998). However, numerous observational studies have shown clusters do not follow the predicted simple, low-scatter mass-observable scaling relations (Edge & Stewart, 1991; Allen & Fabian, 1998a; Markevitch, 1998; Arnaud & Evrard, 1999; Horner et al., 1999; Nevalainen et al., 2000; Finoguenov et al., 2001). To reconcile observation with theory, it was realized non-gravitational effects, such as

heating and radiative cooling in cluster cores, could not be neglected if models were to accurately replicate the process of cluster formation, *e.g.* Loewenstein (2000) and Borgani et al. (2002).

As a consequence of radiative cooling, best-fit total cluster temperature decreases while total cluster luminosity increases. In addition, feedback sources such as active galactic nuclei (AGN) and supernovae can drive cluster cores (where most of the cluster flux originates) away from hydrostatic equilibrium. Thus, at a given mass scale, radiative cooling and feedback conspire to create dispersion in otherwise tight mass-observable correlations like mass-luminosity and mass-temperature. While considerable progress has been made both observationally and theoretically in the areas of understanding, quantifying, and reducing scatter in cluster scaling-relations (eg Buote & Tsai, 1996; Jeltema et al., 2005; Kravtsov et al., 2006; Nagai et al., 2007; Ventimiglia et al., 2008), it is still important to understand how, taken as a whole, non-gravitational processes affect cluster formation and evolution.

An appurtenant issue to the departure of clusters from self-similarity is that of cooling flows in cluster cores. The core cooling time in 50%-66% of clusters is much shorter than both the Hubble time and cluster age (Stewart et al., 1984; Edge et al., 1992; White et al., 1997; Peres et al., 1998; Bauer et al., 2005). For such clusters (and without compensatory heating), radiative cooling will result in the formation a cooling flow (see Fabian, 1994, for a review). Early estimates put the mass deposition rates from cooling flows in the range of $100 - 1000 \text{ M}_\odot \text{ yr}^{-1}$, (*e.g.* Jones & Forman, 1984). However, cooling flow mass deposition rates inferred from soft X-ray spectroscopy were found to be significantly less than predicted, with the ICM never reaching temperatures lower than $T_{virial}/3$ (Tamura et al., 2001; Peterson et al., 2001, 2003; Kaastra et al., 2004). Irrespective of system mass, the massive torrents of cool gas turned out to be more like cooling trickles.

In addition to the lack of soft X-ray line emission from cooling flows, prior method-

ical searches for the end products of cooling flows (*i.e.* molecular gas and emission line nebulae) revealed far less mass is locked-up in by-products than expected (Heckman et al., 1989; McNamara et al., 1990; O’Dea et al., 1994b; Voit & Donahue, 1995). The disconnects between observation and theory have been termed “the cooling flow problem” and raise the question, “Where has all the cool gas gone?” The substantial amount of observational evidence suggests some combination of energetic feedback sources have heated the ICM to selectively remove gas with a short cooling time and establish quasi-stable thermal balance of the ICM.

Both the breakdown of self-similarity and the cooling flow problem point toward the need for better understanding cluster feedback and radiative cooling. Recent revisions to models of how clusters form and evolve by including feedback sources has led to better agreement between observation and theory (Bower et al., 2006; Croton et al., 2006; Saro et al., 2006). The current paradigm regarding the cluster feedback process holds that AGN are the primary heat delivery mechanism and that an AGN outburst deposits the requisite energy into the ICM to retard, and in some cases quench, cooling (see McNamara & Nulsen, 2007, for a review). How the feedback loop functions is still the topic of much debate, but that AGN are interacting with the hot atmospheres of clusters is no longer in doubt as evidenced by the prevalence of bubbles in clusters (Bîrzan et al., 2004). One robust observable which has proven useful in studying the effect of non-gravitational processes is ICM entropy.

Taken individually, ICM temperature and density do not fully reveal a cluster’s thermal history because these quantities are most influenced by the underlying dark matter potential (Voit et al., 2002). Gas temperature reflects the depth of the potential well, while density reflects the capacity of the well to compress the gas. However, at constant pressure the density of a gas is determined by its specific entropy. Rewriting the expression for the adiabat, $K = P\rho^{-5/3}$, in terms of temperature and electron density, one can define a new quantity, $K = kT_X n_e^{-2/3}$, where T_X is temperature and

n_e is electron gas density (Ponman et al., 1999; Lloyd-Davies et al., 2000). This new quantity, K , captures the thermal history of the gas because only heating and cooling can change K . This quantity is commonly referred to as entropy, but in actuality the classic thermodynamic entropy is $s = \ln K^{3/2} + \text{constant}$.

One important property of gas entropy is that a gas cloud is convectively stable when $dK/dr \geq 0$. Thus, gravitational potential wells are giant entropy sorting devices: low entropy gas sinks to the bottom of the potential well, while high entropy gas buoyantly rises to a radius of equal entropy. If cluster evolution proceeded under the influence of gravitation only, then the radial entropy distribution of clusters would exhibit power-law behavior for $r > 0.1r_{200}$ with a constant, low entropy core at small radii (Voit et al., 2002). Thus, large-scale departures of the radial entropy distribution from a power-law can be used to measure the affect of processes such as AGN heating and radiative cooling. Several studies have found that the radial ICM entropy distribution in some clusters flattens outside $0.1r_{500}$ (David et al., 1996; Ponman et al., 1999; Lloyd-Davies et al., 2000; Ponman et al., 2003; Piffaretti et al., 2005; Donahue et al., 2005, 2006; Morandi & Ettori, 2007). These previous studies utilized smaller, focused samples and we have undertaken a much larger study utilizing the *Chandra* Data Archive.

In this chapter we present the data and results from a *Chandra* archival project in which we studied the ICM entropy distribution for 233 galaxy clusters. We have named this project the “Archive of *Chandra* Cluster Entropy Profile Tables,” or *ACCEPT* for short. In contrast to the sample of nine classic cooling flow clusters studied in Donahue et al. (2006, hereafter D06), *ACCEPT* covers a broader range of luminosities, temperatures, and morphologies, focusing on more than just cooling flow clusters. One of our primary objectives for this project was to provide the research community with an additional resource to study cluster evolution and confront current models with a broad range of entropy profiles.

We have found that the departure of entropy profiles from a self-similar power-law is not limited to cooling flow clusters, but is a feature of most clusters, and given high enough angular resolution, possibly all clusters. We also find that the core entropy distribution of both the full *ACCEPT* collection and the Highest X-Ray Flux Galaxy Cluster Sample (*HIFLUGCS*, Reiprich 2001; Reiprich & Böhringer 2002) are bimodal. In Chapter 4, we present results that show indicators of feedback - namely radio sources assumed to be associated with AGN and H α emission assumed to be the result of thermal instability formation - are strongly correlated with core entropy.

A key aspect of this project is the dissemination of all data and results to the public. We have created a searchable, interactive web site¹ which hosts all of our results. The *ACCEPT* web site is being continually updated as new *Chandra* cluster and group observations are archived and analyzed. The web site provides all data tables, plots, spectra, reduced *Chandra* data products (forthcoming), reduction scripts, and more. Given the large number of clusters in our sample, figures, fits, and tables showing/listing results for individual clusters have been omitted and are available at the *ACCEPT* web site.

The structure of this chapter is as follows: In §3.2 we outline initial sample selection criteria and information about the *Chandra* observations selected under these criteria. Data reduction is discussed in §3.3. Spectral extraction and analysis are discussed in §3.3.1, while our method for deriving deprojected electron density profiles is outlined in §3.3.2. A few possible sources of systematics are discussed in §3.4. Results and discussion are presented in §3.5. A brief summary is given in §3.6. For this work we have assumed a flat Λ CDM Universe with cosmology $\Omega_M = 0.3$, $\Omega_\Lambda = 0.7$, and $H_0 = 70 \text{ km s}^{-1} \text{ Mpc}^{-1}$. All quoted uncertainties are 90% confidence (1.6σ).

¹<http://www.pa.msu.edu/astro/MC2/accept>

3.2 DATA COLLECTION

Our sample was initially collected from observations publicly available in the *Chandra* Data Archive (CDA) as of June 2006. We first assembled a list of targets from multiple flux-limited surveys: the *ROSAT* Brightest Cluster Sample (Ebeling et al., 1998), RBCS Extended Sample (Ebeling et al., 2000), *ROSAT* Brightest 55 Sample (Edge et al., 1990; Peres et al., 1998), *Einstein* Extended Medium Sensitivity Survey (Gioia et al., 1990), North Ecliptic Pole Survey (Henry et al., 2006), *ROSAT* Deep Cluster Survey (Rosati et al., 1995), *ROSAT* Serendipitous Survey (Vikhlinin et al., 1998), Massive Cluster Survey (Ebeling et al., 2001), and *REFLEX* Survey (Böhringer et al., 2004). After the first round of data analysis concluded, we continued to expand our collection by adding new archival data listed under the CDA Science Categories “clusters of galaxies” or “active galaxies.” As of submission, we have inspected all CDA clusters of galaxies observations and analyzed 510 of those observations (14.16 Msec). The Coma and Fornax clusters have been intentionally left-out of our sample because they are very well studied nearby clusters which require a more intensive analysis than we undertook in this project.

The available data for some clusters limited our ability to derive an entropy profile. Calculation of entropy requires measurement of the radial gas temperature and density structure (discussed further in §3.3). To infer a temperature which is reasonably well constrained ($\Delta kT_X \approx \pm 1.0$ keV) we imposed a minimum requirement of three temperature bins containing 2500 counts each. A post-analysis check shows our T_X minimum criterion resulted in a mean $\Delta kT_X = 0.87$ keV for the final sample.

In section 3.5.4 we cull the *HIFLUGCS* primary sample (Reiprich, 2001; Reiprich & Böhringer, 2002) from our full archival collection. The groups M49, NGC 507, NGC 4636, NGC 5044, NGC 5813, and NGC 5846 are part of the *HIFLUGCS* primary sample but were not members of our initial archival sample. In order to take full advantage of the *HIFLUGCS* primary sample, we analyzed observations of these

6 groups. Note, however, that none of these 6 groups are included in the general discussion of *ACCEPT*.

We were unable to analyze some clusters for this study because of complications other than not meeting our minimum requirements for analysis. These clusters were: 2PIGG J0311.8-2655, 3C 129, A168, A514, A753, A1367, A2634, A2670, A2877, A3074, A3128, A3627, AS0463, APMCC 0421, MACS J2243.3-0935, MS J1621.5+2640, SDSS J198.070267-00.984433, RX J1109.7+2145, RX J1206.6+2811, RX J1423.8+2404, Triangulum Australis, and Zw5247.

After applying the T_X constraint, adding the 6 *HIFLUGCS* groups, and removing troublesome observations the final sample presented here contains 310 observations of 233 clusters with a total exposure time of 9.66 Msec. The sample covers the temperatures range $kT_X \sim 1 - 20$ keV, a bolometric luminosity range of $L_{bol} \sim 10^{42-46}$ ergs s $^{-1}$, and redshifts of $z \sim 0.05 - 0.89$. Table ?? lists the general properties for each cluster in *ACCEPT*.

We also report H α observations taken by M. Donahue while a Carnegie Fellow. These observations were not utilized in this chapter but are used in Chapter 4. The new [NII]/H α ratios and H α fluxes are listed in Table ???. The upper-limits listed in Table ??? are 3σ significance. The observations were taken with either the 5 m Hale Telescope at the Palomar Observatory, USA, or the DuPont 2.5 m telescope at the Las Campanas Observatory, Chile. All observations were made with a 2'' slit centered on the BCG using two position angles: one along the semi-major axis and one along the semi-minor axis of the galaxy. The overlap area was 10 pixels 2 . The red light (555-798 nm) setup on the Hale Double Spectrograph used a 316 lines/mm grating with a dispersion of 0.31 nm/pixel and an effective resolution of 0.7-0.8 nm. The DuPont Modular Spectrograph setup included a 1200 lines/mm grating with a dispersion of 0.12 nm/pixel and an effective resolution of 0.3 nm. The statistical and calibration uncertainties for the observations are both $\sim 10\%$. The statistical uncertainty arises

primarily from variability of the spectral continuum and hence imperfect background subtraction.

3.3 DATA ANALYSIS

Measuring radial ICM entropy first requires measurement of radial ICM temperature and density. The radial temperature structure of each cluster was measured by fitting a single-temperature thermal model to spectra extracted from concentric annuli centered on the cluster X-ray “center”. As discussed in Cavagnolo et al. (2008), the ICM X-ray peak of the point-source cleaned, exposure-corrected cluster image was used as the cluster center, unless the iteratively determined X-ray centroid was more than 70 kpc away from the X-ray peak, in which case the centroid was used as the radial analysis zero-point. To derive the gas density profile, we first deprojected an exposure-corrected, background-subtracted, point source clean surface brightness profile extracted in the 0.7-2.0 keV energy range to attain a volume emission density. This emission density, along with spectroscopic information (count rate and normalization in each annulus), was then used to calculate gas density. The resulting entropy profiles were then fit with two models: a simple model which has only a radial power-law component, and a model which is the sum of a constant core entropy term, K_0 and the radial power-law component.

In this chapter we cover the basics of deriving gas entropy from X-ray observables, and direct interested readers to D06 for in-depth discussion of our data reprocessing and reduction, and Cavagnolo et al. (2008) for details regarding determination of each cluster’s “center” and how the X-ray background was handled. The only difference between the analysis presented in this chapter and that of D06 and Cavagnolo et al. (2008), is that we have used newer versions of the CXC issued data reduction software (CIAO 3.4.1 and CALDB 3.4.0).

3.3.1 TEMPERATURE PROFILES

One of the two components needed to derive a gas entropy profile is the temperature as a function of radius. We therefore constructed radial temperature profiles for each cluster in our collection. To reliably constrain a temperature, and allow for the detection of temperature structure beyond isothermality, we required each temperature profile to have a minimum of three annuli containing 2500 counts each. The annuli for each cluster were generated by first extracting a background-subtracted cumulative counts profile using 1 pixel width annular bins originating from the cluster center and extending to the detector edge. Temperature profiles, however, were truncated at the radius bounded by the detector edge, or $0.5R_{180}$, whichever was smaller. Truncation occurred at $0.5R_{180}$ as we are most interested in the radial entropy behavior of cluster core regions ($r \lesssim 100$ kpc) and $0.5R_{180}$ is the approximate radius where temperature profiles begin to turnover (Vikhlinin et al., 2005). Additionally, analysis of diffuse gas temperature structure at large radii, which spectroscopically is dominated by background, requires a time consuming, observation-specific analysis of the X-ray background (see Sun et al., 2008, for a detailed discussion on this point).

Cumulative counts profiles were divided into annuli containing at least 2500 counts. For well resolved clusters, the number of counts per annulus was increased to reduce the resulting uncertainty of kT_X and, for simplicity, to keep the number of annuli less than 50. The method we use to derive entropy profiles is most sensitive to the surface brightness radial bin size and not the resolution or uncertainties of the temperature profile. Thus, the loss of resolution in the temperature profile from increasing the number of counts per bin, and thereby reducing the number of annuli, has an insignificant effect on the final entropy profiles and best-fit entropy models.

Background analysis was performed using the blank-sky datasets provided in the CALDB. Backgrounds were reprocessed and reprojected to match each observation. Off-axis chips were used to normalize for variations of the hard-particle background

by comparing blank-sky and observation 9.5-12 keV count rates. Soft residuals were also created and fitted for each observation to account for the spatially-varying soft Galactic background. This component was added as an additional, fixed background component during spectral fitting. Errors associated with the soft background are estimated and added in quadrature to the final error.

For each radial annular region, source and background spectra were extracted from the target cluster and corresponding normalized blank-sky dataset. Following standard CIAO techniques² we created weighted response files (WARF) and redistribution matrices (WRMF) for each cluster using a flux-weighted map (WMAP) across the entire extraction region. These files quantify the effective area, quantum efficiency, and imperfect resolution of the *Chandra* instrumentation as a function of chip position. Each spectrum was binned to contain a minimum of 25 counts per energy bin.

Spectra were fitted with XSPEC 11.3.2ag (Arnaud, 1996) using an absorbed, single-temperature MEKAL model (Mewe et al., 1985, 1986) over the energy range 0.7-7.0 keV. Neutral hydrogen column densities, N_{H} , were taken from Dickey & Lockman (1990). A comparison between the N_{H} values of Dickey & Lockman (1990) and the higher-resolution LAB Survey (Kalberla et al., 2005) revealed that the two surveys agree to within $\pm 20\%$ for 80% of the clusters in our sample. For the other 20% of the sample, using the LAB value, or allowing N_{H} to be free, did not result in best-fit temperatures or metallicities which differ significantly from fits using the Dickey & Lockman (1990) values.

The potentially free parameters of the absorbed thermal model are N_{H} , X-ray temperature, metal abundance normalized to solar (Anders & Grevesse, 1989, elemental ratios taken from), and a normalization proportional to the integrated emission mea-

²<http://cxc.harvard.edu/ciao/guides/esa.html>

sure within the extraction region,

$$\eta = \frac{10^{-14}}{4\pi D_A^2(1+z)^2} \int n_e n_p dV, \quad (3.1)$$

where D_A is the angular diameter distance, z is cluster redshift, n_e and n_p are the electron and proton densities respectively, and V is the volume of the emission region. In all fits the metal abundance in each annulus was a free parameter and N_{H} was fixed to the Galactic value. No systematic error is added during fitting and thus all quoted errors are statistical only. The statistic used during fitting was χ^2 (XSPEC statistics package CHI). All uncertainties were calculated using 90% confidence.

For some clusters, more than one observation was available in the archive. We utilized the combined exposure time by first extracting independent spectra, WARFs, WRMFs, normalized background spectra, and soft residuals for each observation. These independent spectra were then read into XSPEC simultaneously and fit with the same spectral model which had all parameters, except normalization, tied among the spectra.

In D06 we studied a sample of nine “classic” cooling flow clusters, all of which have steep temperature gradients. Deprojection of temperature should result in slightly lower temperatures in the central bins of only the clusters with the steepest temperature gradients. For these clusters, the end result would be a lowering of the entropy for the central-most bins. Our analysis in D06 showed that spectral deprojection did not result in significant differences between entropy profiles derived using projected or deprojected quantities. Thus, for this work, we quote projected temperatures only. We stress that spectral deprojection does not significantly change the shape of the entropy profiles nor the best-fit K_0 values.

3.3.2 DEPROJECTED ELECTRON DENSITY PROFILES

For predominantly free-free emission, emissivity strongly depends on density and only weakly on temperature, $\epsilon \propto \rho^2 T^{1/2}$. Therefore the flux measured in a narrow temperature range is a good diagnostic of ICM density. To reconstruct the relevant gas density as a function of physical radius we deprojected the cluster emission from high-resolution surface brightness profiles and converted to electron density using normalizations and count rates taken from the spectral analysis.

We extracted surface brightness profiles from the 0.7-2.0 keV energy range using concentric annular bins of size $5''$ originating from the cluster center. Each surface brightness profile was corrected with an observation specific, normalized radial exposure profile to remove the effects of vignetting and exposure time fluctuations. Following the recommendation in the CIAO guide for analyzing extended sources, exposure maps were created using the monoenergetic value associated with the observed count rate peak. The more sophisticated method of creating exposure maps using spectral weights calculated for an incident spectrum with the temperature and metallicity of the observed cluster was also tested. For the narrow energy band we consider, the chip response is relatively flat and we find no significant differences between the two methods. For all clusters the monoenergetic value used in creating exposure maps was between 0.8 – 1.7 keV.

The 0.7-2.0 keV spectroscopic count rate and spectral normalization were interpolated from the radial temperature profile grid to match the surface brightness radial grid. Utilizing the deprojection technique of Kriss et al. (1983), the interpolated spectral parameters were used to convert observed surface brightness to deprojected electron density. Radial electron density written in terms of relevant quantities is,

$$n_e(r) = \sqrt{\frac{r_{ion} 4\pi [D_A(1+z)]^2 C(r) \eta(r)}{10^{-14} f(r)}} \quad (3.2)$$

where r_{ion} is an ionization ratio ($n_e = 1.2n_p$), $C(r)$ is the radial emission density derived from eqn. A1 in Kriss et al. (1983), η is the interpolated spectral normalization from eqn. 3.1, D_A is the angular diameter distance, z is cluster redshift, and $f(r)$ is the interpolated spectroscopic count rate. Cosmic dimming of source surface brightness is accounted for by the $D_A^2(1+z)^2$ term. This method of deprojection takes into account temperature and metallicity fluctuations which affect observed gas emissivity. Errors for the gas density profile were estimated using 5000 Monte Carlo simulations of the original surface brightness profile. The Kriss et al. (1983) deprojection technique assumes spherical symmetry, but it was shown in D06 such an assumption has little effect on final entropy profiles.

3.3.3 β -MODEL FITS

Noisy surface brightness profiles, or profiles with irregularities such as inversions or extended flat cores, result in unstable, unphysical quantities when using the “onion” deprojection technique. For cases where deprojection of the raw data was problematic, we resorted to fitting the surface brightness profile with a β -model (Cavaliere & Fusco-Femiano, 1978). It is well known that the β -model is only an approximation for an isothermal gas distribution and does not precisely represent all the features of the ICM (Ettori, 2000; Loken et al., 2002; Hallman et al., 2007). However, for the profiles which required a fit, the β -model was a suitable approximation, and the models use was only a means for creating a smooth function which was easily deprojected. The single ($N = 1$) and double ($N = 2$) β -models were used in fitting,

$$S_X = \sum_{i=1}^N S_i \left[1 + \left(\frac{r}{r_{c,i}} \right)^2 \right]^{-3\beta_i + \frac{1}{2}}. \quad (3.3)$$

The models were fitted using Craig Markwardt’s robust non-linear least squares minimization IDL routines³. The data input to the fitting routines were weighted using the inverse square of the observational errors. Using this weighting scheme resulted in residuals which were near unity for, on average, the inner 80% of the radial range considered. Accuracy of errors output from the fitting routine were checked against a bootstrap Monte Carlo analysis of 1000 surface brightness realizations. Both the single- and double- β models were fit to each profile and using the F-test functionality of SHERPA⁴ we determined if the addition of extra model components was justified given the degrees of freedom and χ^2 values of each fit. If the significance was less than 0.05, the extra components were justified and the double- β model was used.

A best-fit β -model was used in place of the data when deriving electron density for the clusters listed in Table ???. These clusters are also flagged in Table ??? with the note letter ‘a’. In Section §3.8, notes discussing individual clusters are provided, and a figure of the best-fit β -models and background-subtracted, exposure-corrected surface brightness profiles are provided in Figure 3.10. The disagreement between the best-fit β -model and the surface brightness in the central regions for some clusters is also discussed in Section §3.8. In short, the discrepancy arises from the presence of compact X-ray sources, a topic which is addressed in §3.3.5. All clusters requiring a β -model fit have $K_0 > 95 \text{ keV cm}^2$ and the mean best-fit parameters are listed in Table ??.

3.3.4 ENTROPY PROFILES

Radial entropy profiles were calculated using the widely adopted formulation $K(r) = kT_x(r)n_e(r)^{-2/3}$. To create the radial entropy profiles, the temperature and density profiles must be on the same radial grid. This was accomplished by interpolating the temperature profile across the higher-resolution radial grid of the deprojected electron

³<http://cow.physics.wisc.edu/~craigm/idl/>

⁴<http://cxc.harvard.edu/ciao3.4/ahelp/ftest.html>

density profile. Because, in general, density profiles have higher radial resolution, the central bin of the temperature profile spans several of the innermost bins of the density profile. Since we are most interested in the behavior of the entropy profiles in the central regions, how the interpolation was performed for the inner regions. Thus, temperature interpolation over the region of the density profile where a single central temperature bin encompasses several density profile bins was applied in two ways: (1) as a linear gradient consistent with the slope of the temperature profile at radii larger than the central T_X bin ($\Delta T_{center} \neq 0$; ‘extr’ in Table ??), and (2) as a constant ($\Delta T_{center} = 0$; ‘flat’ in Table ??). Shown in Figure 3.1 is the ratio of best-fit core entropy, K_0 , using the above two methods. The five points lying below the line of equality are clusters which are best-fit by a power-law or have K_0 statistically consistent with zero. It is worth noting that both schemes yield statistically consistent values for K_0 except for the clusters marked by red points which have a ratio significantly different from unity.

The clusters which significantly differ from one all have steep temperature gradients with the maximum and minimum radial temperatures differing by a factor of 1.3-5.0. Extrapolation of a steep temperature gradient as $r \rightarrow 0$ results in very low central temperatures (typically $T_X \leq T_{virial}/3$) which are inconsistent with observations, most notably Peterson et al. (2003). Most important however, is that the flattening of entropy we observe in the cores of our sample (discussed in §3.5.1) is ***not*** a result of the method chosen for interpolating the temperature profile. For this chapter we therefore focus on the results derived assuming a constant temperature across the central-most bins.

Uncertainty in $K(r)$ arising from using a single-component temperature model for each annulus during spectral analysis contributes negligibly to our final fits and is discussed in detail in the Appendix of D06. Briefly summarizing D06: we have primarily measured the entropy of the lowest entropy gas because it is the most lu-

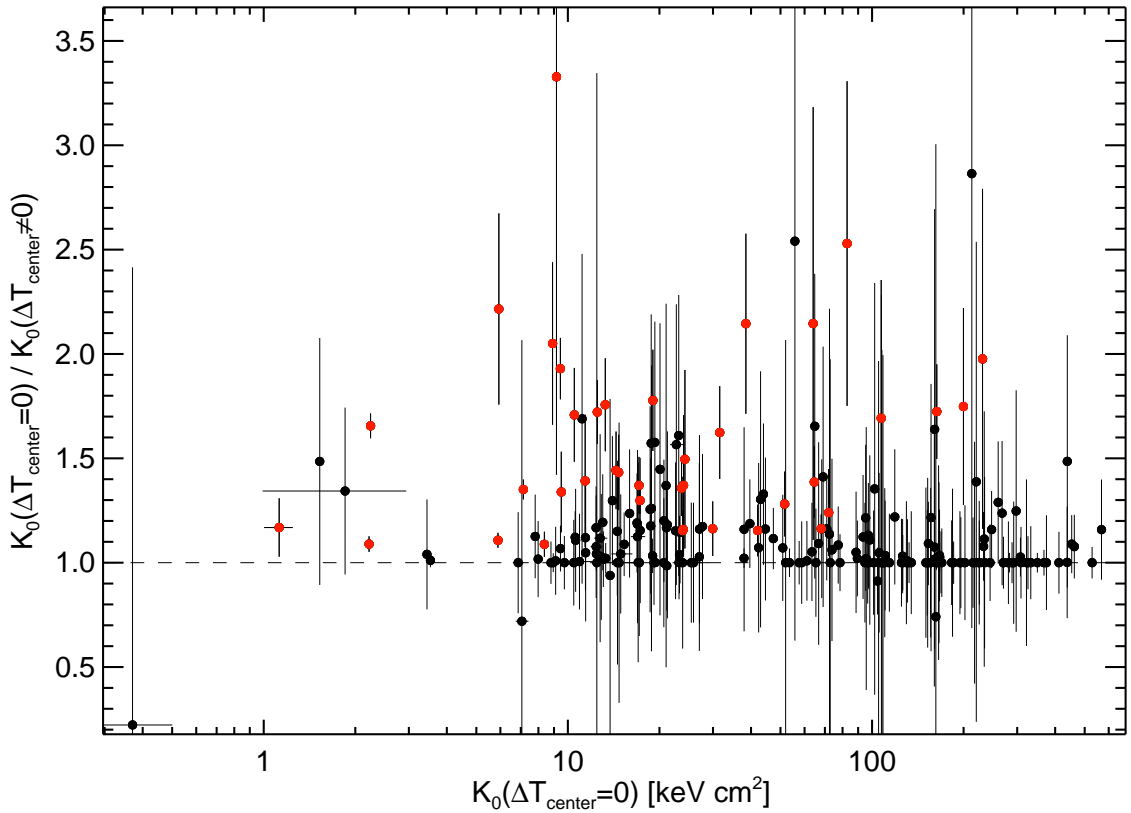


Figure 3.1 Ratio of best-fit K_0 for the two treatments of central temperature interpolation (see §3.3.1): (1) temperature is free to decline across the central density bins ($\Delta T_{\text{center}} \neq 0$), and (2) the temperature across the central density bins is isothermal ($\Delta T_{\text{center}} = 0$). Red points are clusters for which the K_0 ratio is inconsistent with unity, however, all of these clusters have steep temperature gradients which result in unsubstantiated cool temperatures in their cores when kT_X is extrapolated to small radii.

minous gas. For the best-fit entropy values to be significantly changed, the volume filling fraction of a higher-entropy component must be non-trivial ($> 50\%$). As discussed in D06, our results are robust to the presence of multiple, low luminosity gas phases and mostly insensitive to X-ray surface brightness decrements, such as X-ray cavities and bubbles, although in extreme cases their influence on an entropy profile can be detected (for an example, see the cluster A2052).

Each entropy profile was fit with two models: a simple model which is a power-law at large radii and approaches a constant value at small radii (eqn. 3.4), and a model which is a power-law only (eqn. 3.5). The models were fitted using Craig Markwardt's IDL routines in the package MPFIT. The output best-fit parameters and associated errors were checked against a bootstrap Monte Carlo analysis of 5000 entropy profile realizations to independently confirm their accuracy.

$$K(r) = K_0 + K_{100} \left(\frac{r}{100 \text{ kpc}} \right)^\alpha \quad (3.4)$$

$$K(r) = K_{100} \left(\frac{r}{100 \text{ kpc}} \right)^\alpha. \quad (3.5)$$

In our entropy models, K_0 is what we call core entropy, K_{100} is a normalization for entropy at 100 kpc, and α is the power-law index. Note, however, that K_0 does not necessarily represent the minimum core entropy or the entropy at $r = 0$. Nor does K_0 capture the gas entropy which would be measured immediately around an AGN or in a BCG X-ray corona. Instead, K_0 represents the typical excess of core entropy above the best fitting power-law at larger radii. Fits were truncated at a maximum radius (determined by-eye) to avoid the influence of noisy bins at large radii which result from instability of our deprojection method. A listing of all the best-fit parameters for each cluster are listed in Table ???. The mean best-fit parameters for the full *ACCEPT* sample are given in Table ???. Also given in Table ?? are the mean best-fit parameters for clusters below and above $K_0 = 50 \text{ keV cm}^2$. We show in §3.5.2

that the cut at $K_0 = 50 \text{ keV cm}^2$ is not completely arbitrary as it approximately demarcates the division between two distinct populations in the K_0 distribution.

Some clusters have a surface brightness profile which is comparable to a double β -model. Our models for the behavior of $K(r)$ are intentionally simplistic and are not intended to fully describe all the features of $K(r)$. Thus, for the small number of clusters with discernible double- β behavior, fitting of the entropy profiles was restricted to the innermost of the two β -like features. These clusters have been flagged in Table ?? with the note letter ‘b’. The best-fit power-law index is typically much steeper for these clusters, but the outer regions, which we do not discuss here, have power-law indices which are typical of the rest of the sample, *i.e.* $\alpha \sim 1.2$.

3.3.5 EXCLUSION OF CENTRAL SOURCES

For many clusters in our sample the ICM X-ray peak, ICM X-ray centroid, BCG optical emission, and BCG infrared emission are coincident or well within 70 kpc of one another. This made identification of the cluster center robust and trivial. However, in some clusters, there is an X-ray point source or compact X-ray source ($r \lesssim 5 \text{ kpc}$) found very near ($r < 10 \text{ kpc}$) the cluster center and always associated with a BCG. We identified 37 clusters with central sources and have flagged them in Table ?? with the note letter ‘d’ for AGN and ‘e’ for compact but resolved sources. The mean best-fit parameters for these clusters are given in Table ?? under the sample name ‘CSE’ for “central source excluded.” These clusters cover the redshift range $z = 0.0044 - 0.4641$ with mean $z = 0.1196 \pm 0.1234$, and temperature range $kT_X = 1 - 12 \text{ keV}$ with mean $kT_X = 4.43 \pm 2.53 \text{ keV}$. For some clusters – such as 3C 295, A2052, A426, Cygnus A, Hydra A, or M87 – the source is an AGN and there was no question the source must be removed.

However, determining how to handle the compact X-ray sources was not so straightforward. These compact sources are larger than the PSF, fainter than an AGN, but

typically have significantly higher surface brightness than the surrounding ICM such that the compact source’s extent was distinguishable from the ICM. These sources are most prominent, and thus the most troublesome, in non-cool core clusters (*i.e.* clusters which are approximately isothermal). They are troublesome because the compact source is typically much cooler and denser than the surrounding ICM and hence has an entropy much lower than the ambient ICM. We consider most of these compact sources are X-ray coronae associated with the BCG (Sun et al., 2007).

Without removing the compact sources, we derived radial entropy profiles and found, for all cases, that $K(r)$ abruptly changes at the outer edge of the compact source. Including the compact sources results in the central cluster region(s) appearing overdense, and at a given temperature the region will have a much lower entropy than if the source were excluded. Such a discontinuity in $K(r)$ results in our simple models of $K(r)$ not being a good description of the profiles. Aside from producing poor fits, a significantly lower entropy influences the value of best-fit parameters because the shape of $K(r)$ is drastically changed. Obviously, two solutions are available: exclude or keep the compact sources during analysis. Deciding what to do with these sources depends upon what cluster properties we are specifically interested in quantifying.

The compact X-ray sources discussed in this section are not representative of the cluster’s core entropy; these sources are representative of the entropy within and immediately surrounding peculiar BCGs. Our focus for the *ACCEPT* project was to quantify the entropy structure of the cluster core region and surrounding “pristine” ICM, not to determine the minimum entropy of cluster cores or to quantify the entropy of peculiar core objects such as BCG coronae. Thus, we concluded to exclude these compact sources during our analysis. For a few extraordinary sources, it was simpler to ignore the central bin of the surface brightness profile during analysis because of imperfect exclusion of a compact source’s extended emission. These clusters have

been flagged in Table ?? with the note letter ‘f’.

It is worth noting that when any source is excluded from the data, the empty pixels where the source once was were not included in the calculation of the surface brightness (counts and pixels are both excluded). Thus, the decrease in surface brightness of a bin where a source has been removed is not a result of the count to area ratio being artificially reduced.

3.4 SYSTEMATICS

Our models for $K(r)$ were designed so that the best-fit K_0 values are a good measure of the entropy profile flattening at small radii. This flattening could potentially be altered through the effects of systematics such as PSF smearing and surface brightness profile angular resolution. To quantify the extent to which our K_0 values are being affected by these systematics, we have analyzed mock *Chandra* observations created using the ray-tracing program MARX⁵, and also by analyzing degraded entropy profiles generated from artificially redshifting well-resolved clusters. In the analysis below we show that the lack of $K_0 \lesssim 10 \text{ keV cm}^2$ at $z \gtrsim 0.1$ is attributable to resolution effects, but that deviation of an entropy profile from a power-law, even if only in the centralmost bin, cannot be accounted for by PSF effects. We also discuss the number of profiles which are reasonably well-represented by the power-law only profile, and establish that no more than $\sim 10\%$ of the entropy profiles in *ACCEPT* are consistent with a power-law.

3.4.1 PSF EFFECTS

To assess the effect of PSF smearing on our entropy profiles, we have updated the analysis presented in §4.1 of D06 to use MARX simulations. In the D06 analysis, we assumed the density and temperature structure of the cluster core obeyed power-laws

⁵<http://space.mit.edu/CXC/MARX/>

with $n_e \propto r^{-1}$ and $T_X \propto r^{1/3}$. This results in a power-law entropy profile with $K \propto r$. Further assuming the main emission mechanism is thermal bremsstrahlung, *i.e.* $\epsilon_X \propto T_X^{1/2}$, yields a surface brightness profile which has the form $S_X \propto r^{-5/6}$. A source image consistent with these parameters was created in IDL and then input to MARX to create the mock *Chandra* observations.

The MARX simulations were performed using the spectrum of a 4.0 keV, $0.3Z_\odot$ abundance MEKAL model. We have tested using input spectra with $kT_X = 2 - 10$ keV with varying abundances and find the effect of temperature and metallicity on the distribution of photons in MARX to be insignificant for our discussion here. We have neglected the X-ray background in this analysis as it is overwhelmed by cluster emission in the core and is only important at large radii. Observations for both ACIS-S and ACIS-I instruments were simulated using an exposure time of 40 ksec. A surface brightness profile was then extracted from the mock observations using the same $5''$ bins used on the real data.

For $5''$ bins, we find the difference between the central bins of the input surface brightness and the output MARX observations to be less than the statistical uncertainty. One should expect this result, as the on-axis *Chandra* PSF is $\lesssim 1''$ and the surface brightness bins we have used on the data are five times this size. What is most interesting and important though, is that our analysis using MARX suggests any deviation of the surface brightness – and consequently the entropy profile – from a power-law, even if only in the central bin, is real and cannot be attributed to PSF effects. Even for the most poorly resolved clusters, the deviation away from a power-law we observe in so many of our entropy profiles is not a result of our deprojection technique or systematics.

3.4.2 ANGULAR RESOLUTION EFFECTS

Another possible limitation on evaluating K_0 is the effect of using fixed angular size bins for extracting surface brightness profiles. This choice may introduce a redshift-dependence into the best-fit K_0 values because as redshift increases, a fixed angular size encompasses a larger physical volume and the value of K_0 may increase if the bin includes a broad range of gas entropy. Shown in Figure 3.2 is a plot of the best-fit K_0 values for our entire sample versus redshift. At low redshift ($z < 0.02$), there are a few objects with $K_0 < 10 \text{ keV cm}^2$ and only one at higher redshift (A1991 – $K_0 = 1.53 \pm 0.32$, $z = 0.0587$ – which is a very peculiar cluster (Sharma et al., 2004)). This raises the question: can the lack of clusters with $K_0 \lesssim 10 \text{ keV cm}^2$ at $z > 0.02$ be completely explained by resolution effects?

To answer this question we tested the affect redshift has on measuring K_0 by selecting all clusters with $K_0 \leq 10 \text{ keV cm}^2$ and $z \leq 0.1$ and degrading their surface brightness profiles to mimic the effect of increasing the cluster redshift. Our test is best illustrated using an example: consider a cluster at $z = 0.1$. For this cluster, $5'' \approx 9 \text{ kpc}$. Were the cluster at $z = 0.2$, $5''$ would equal $\approx 16 \text{ kpc}$. To mimic moving this example cluster from $z = 0.1 \rightarrow 0.2$, we can extract a new surface brightness profile using a bin size of 16 kpc instead of $5''$. This will result in a new surface brightness profile which has the angular resolution for a cluster at a higher redshift.

We used the preceding procedure to degrade the profiles of our subsample. New surface brightness bin sizes were calculated for each cluster over an evenly distributed grid of redshifts in the range $z = 0.1 - 0.4$ using step sizes of 0.02. The temperature profiles for each cluster were also degraded by starting at the innermost temperature profile annulus and moving outward pairing-up neighboring annuli. New spectra were extracted for these enlarged regions and analyzed following the same procedure detailed in §3.3.1.

The ensemble of artificially redshifted clusters were analyzed using the procedure

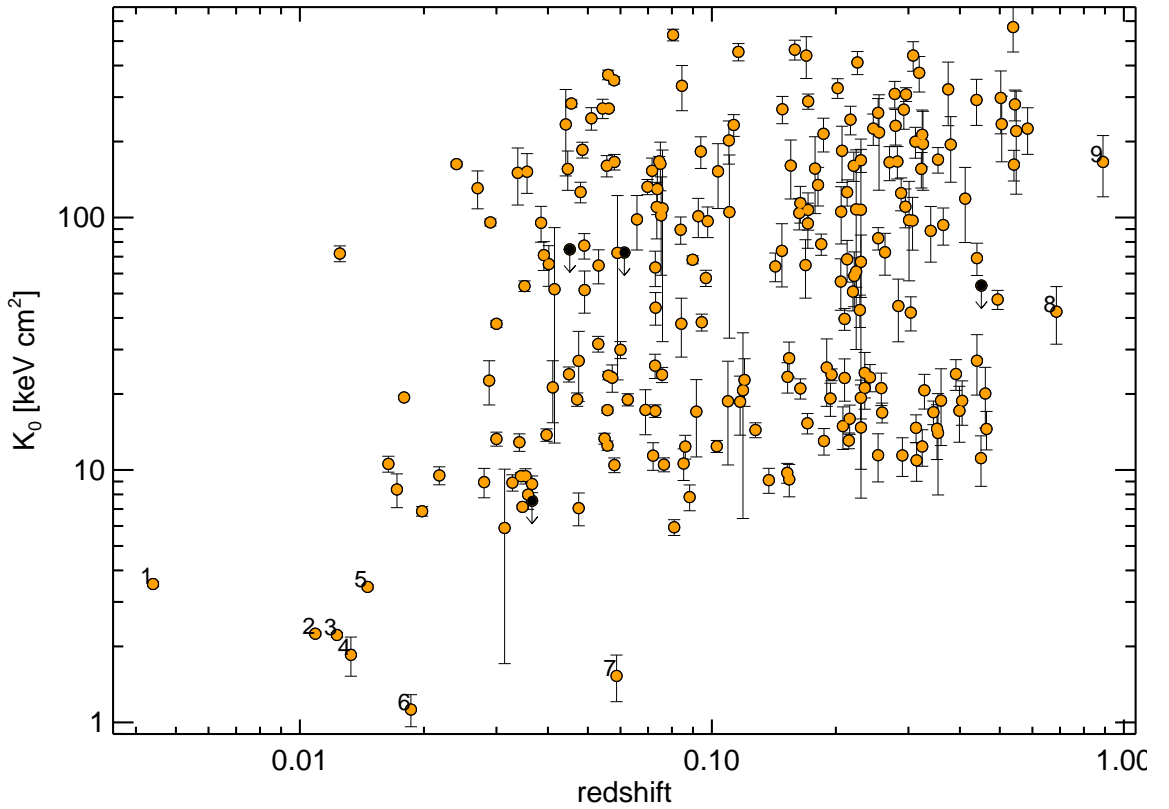


Figure 3.2 Best-fit K_0 versus redshift. Some clusters have K_0 error bars smaller than the point. The clusters with upper-limits (black points with downward arrows) are: A2151, AS0405, MS 0116.3-0115, and RX J1347.5-1145. The numerically labeled clusters are: (1) M87, (2) Centaurus Cluster, (3) RBS 533, (4) HCG 42, (5) HCG 62, (6) SS2B153, (7) A1991, (8) MACS0744.8+3927, and (9) CL J1226.9+3332. For CLJ1226, Maughan et al. (2007) found best-fit $K_0 = 132 \pm 24 \text{ keV cm}^2$ which is not significantly different from our value of $K_0 = 166 \pm 45 \text{ keV cm}^2$. The lack of $K_0 < 10 \text{ keV cm}^2$ clusters at $z > 0.1$ is most likely the result of insufficient angular resolution (see §3.4.2).

outlined in §3.3.4. The notable effects on the entropy profiles arising from lower angular resolution are: (1) less information about profile shape, and (2) increased entropy of the centralmost bins. Obviously, as redshift increases, the number of radial bins decreases. Fewer radial bins translates into less detail of an entropy profile’s curvature, *e.g.* the profiles become less “curvy.” On its own this effect should lead to lower best-fit K_0 values, but, while profile curvature is reduced, the entropy of the central-most bins is increasing because the bins encompass a broader range of entropy. From $z = 0.1 - 0.3$ this last effect dominates, resulting in an increase of $(K'_0 - K_0)/K_0 = 2.72 \pm 1.84$ where K_0 is the original best-fit value and K'_0 is the best-fit value of the degraded profiles. However, at $z > 0.3$, the loss of radial resolution dominates and the degraded profiles begin to resemble power-laws except for the innermost bin which still lies above the power-law (the uncertainty of the best-fit K_0 also increases). The result of a power-law profile with a discrepant central bin is that the degraded K_0 values are only slightly larger than the fiducial best-fit K_0 of the un-degraded data, $(K'_0 - K_0)/K_0 = 0.71 \pm 0.57$.

Our analysis of the degraded entropy profiles suggests that K_0 is more sensitive to the value of $K(r)$ in the central bins than it is to the shape of the profile or the number of radial bins (systematics we explore further in §3.4.3). Most importantly however, is that low-redshift clusters with $K_0 \leq 10 \text{ keV cm}^2$ look like $K_0 \approx 10 - 30 \text{ keV cm}^2$ clusters at $z > 0.1$. Thus we conclude that the lack of $K_0 < 10 \text{ keV cm}^2$ clusters at $z \gtrsim 0.1$ can be attributed to resolution effects.

3.4.3 PROFILE CURVATURE AND NUMBER OF BINS

From our analysis of the degraded entropy profiles in §3.4.2 we found: (1) that the best-fit K_0 is sensitive to the curvature of the entropy profile, and (2) that the number of radial bins may also affect the best-fit K_0 . This raises the possibility of two troubling systematics in our analysis. To check for a possible correlation between

best-fit K_0 and profile curvature we first calculated average profile curvatures, κ_A . For each profile, κ_A was calculated using the standard formulation for curvature of a function, $\kappa = \|y''\|/(1 + y'^2)^{3/2}$, where we set $y = K(r) = K_0 + K_{100}(r/100 \text{ kpc})^\alpha$. This derivation yields,

$$\kappa_A = \frac{\int \frac{\|100^{-\alpha}(\alpha-1)\alpha K_{100}r^{\alpha-2}\|}{[1+(100^{-\alpha}\alpha K_{100}r^{\alpha-1})^2]^{3/2}} dr}{\int dr} \quad (3.6)$$

where α and K_{100} are the best-fit parameters unique to each entropy profile. The integral over all space ensures we evaluate the curvature of each profile in the limit where the profiles have asymptotically approached a constant at small radii and the power-law at large radii. Shown in Figure 3.3 is a plot of κ_A versus K_0 . We find that at any value of K_0 , a large range of curvatures are covered and that there is no systematic trend in K_0 associated with κ_A .

In §3.4.2 we also found that profiles with fewer radial bins tend toward lower best-fit K_0 values. Shown in Figure 3.4 is a plot of K_0 versus the number of bins fit in each entropy profile. From Fig. 3.4 it is evident that that there is only scatter and no trend.

We do not find any systematic trends with profile shape or number of fit bins which would significantly affect our best-fit K_0 values. Thus we conclude that the K_0 values presented in the following sections are an adequate measure of the core entropy and any undetected dependence on profile shape or radial resolution affect our results at significance levels much smaller than the measured uncertainties.

3.4.4 POWER-LAW PROFILES

An important question regarding our entropy profiles is what fraction of the full *ACCEPT* and *HIFLUGCS* samples are well-represented by the power-law only model and/or the power-law plus constant core entropy model? The fitting routine we

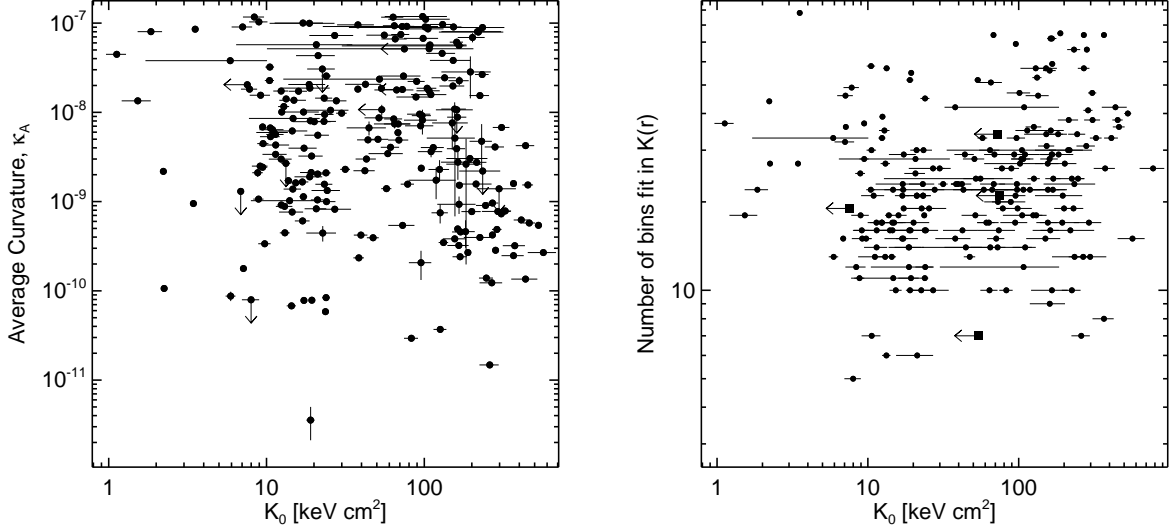


Figure 3.3 Best-fit K_0 versus average curvature. Clusters with K_0 values consistent with zero are plotted using 2σ upper-limits and downward arrows. The lack of a trend in average curvature with K_0 suggests the K_0 values we find are more sensitive to core entropy than to shape of a profile.

Figure 3.4 Best-fit K_0 versus number of bins fit in the entropy profile. The lack of a trend between N_{bins} and K_0 again suggests that our best-fit K_0 values properly represent the core entropy and not the radial resolution of the profile.

used to find the best-fit entropy models to our data is a least-squares minimizer which outputs a chi-square value. Assuming chi-square is the statistic describing the probability distribution, the number of degrees of freedom and χ^2 values can be used to calculate a p-value. For the discussion presented below, we have adopted the conventional significance criterion which says if p-value > 0.05 , then the null hypothesis cannot be rejected, assuming the null hypothesis is “the” true model. The null hypotheses in the case of our models are that $K(r)$ is best modeled as a power-law only (eqn. 3.5) or a power-law plus constant term (eqn. 3.4).

Note that p-values can only determine if the null hypothesis can be significantly rejected. We stress that p-values do not represent the probability that the null hypothesis is correct, nor do p-values measure the significance of the best-fit model compared to the null hypothesis. These are both incorrect interpretations. To judge the quality of the best-fit models, specifically in relation to one another, other quan-

tities must be brought to bear such as the significance of K_0 away from zero, the actual values of χ^2 , and the typical uncertainty associated with the data.

The fractions provided in Table ?? represent the number of clusters in the sample which are well-represented by our $K(r)$ models where “well-represented” is defined as any model which has a p-value > 0.05 . The fractions are independent of each other, hence they do not sum to unity. It may appear odd that for several sub-groups there are a large fraction of the clusters for which the power-law only model cannot be rejected. But in Table ?? we show that most clusters have best-fit K_0 values which are several σ_{K_0} greater than zero. The number and percentage of clusters with K_0 statistically consistent with zero at various confidence levels are given in Table ???. Even at 3σ significance only $\sim 10\%$ of the full *ACCEPT* sample has a best-fit K_0 value which is consistent with zero.

So while it is tempting to think the p-values are implying the power-law model is sufficient to describe $K(r)$ for $\sim 60\%$ of the *ACCEPT* sample, this is not a proper interpretation of the p-values and conflicts with the fact that at least $\sim 90\%$ of the sample have significant non-zero K_0 . Equation 3.4 is a special case of eqn. 3.5 with $K_0 = 0$, *e.g.* the models we fit to $K(r)$ are nested. In addition, the added parameter has an acceptable best-fit value, $K_0 = 0$, which lies on the boundary of the parameter space. While under these conditions χ^2 , associated p-values, and F-tests are not useful in determining which model is the “best” description of $K(r)$, comparison of the χ^2 values for each fit imply, even if only qualitatively, which model shows more agreement with the data. We have made a comparison of the models using an F-test to determine if the addition of the K_0 parameter made a significant improvement in the best-fit. For all clusters, the addition of a K_0 term was found to be warranted, although it is not obvious that an F-test yields any information given the models are nested. Moreover, that there is a systematic trend for a single power-law to be a poor fit mainly at the smallest radii suggests non-zero K_0 is not random.

Of the 233 clusters in *ACCEPT*, only four clusters have a K_0 value which is statistically consistent with zero (at 1σ), or are better fit by the power-law only model (based on comparison of reduced χ^2): A2151, AS0405, MS 0116.3-0115, and NGC 507⁶. Two additional clusters, A1991 and A4059, are better fit by the power-law model only when interpolation of the temperature profile in the core is not constant (see §3.3.1). We find that the entropy model which approaches a constant core entropy at small radii appears to be a better descriptor of the radial entropy distribution for most *ACCEPT* clusters. However, we cannot rule out the power-law only model, but do point out that $\sim 90\%$ of clusters have best-fit K_0 values greater than zero at $> 3\sigma$ significance.

3.5 RESULTS AND DISCUSSION

Presented in Figure 3.5 is a montage of *ACCEPT* entropy profiles for different temperature ranges. These figures highlight the cornerstone result of *ACCEPT*: a uniformly analyzed collection of entropy profiles covering a broad range of core entropy. Each profile is color-coded in representation of the global cluster temperature. Plotted in each panel of Fig. 3.5 are the mean profiles representing $K_0 \leq 50 \text{ keV cm}^2$ clusters (dashed-line) and $K_0 > 50 \text{ keV cm}^2$ clusters (dashed-dotted line), in addition to the pure-cooling model of Voit et al. (2002) (solid black line). The theoretical pure-cooling curve represents the entropy profile of a 5 keV cluster simulated with radiative cooling but no feedback. Thus, the pure-cooling curve represents a lower limit of possible entropy distributions and gives us a useful baseline with which to compare *ACCEPT* profiles.

In the following sections we discuss results gleaned from analysis of our library of entropy profiles. Results such as the departure of most entropy profiles from a simple radial power-law profile, the bimodal distribution of core entropy, and the

⁶NGC 507 is part of *HIFLUGCS* analysis only

asymptotic convergence of the entropy profiles to the self-similar $K(r) \propto r^{1.1}$ power-law at $r \geq 100$ kpc.

3.5.1 NON-ZERO CORE ENTROPY

Arguably the most striking feature of Figure 3.5 is the departure of most profiles from a simple power-law. Core flattening of surface brightness profiles (and consequently density profiles) is a well known feature of clusters (*e.g.* Mohr et al. 1999 and Xue & Wu 2000). What is notable in our work however is that, based on comparison of reduced χ^2 and significance of K_0 very few of the clusters in our sample have an entropy distribution which is best-fit by the power-law only model (eqn. 3.5), rather they are sufficiently well-described by the model which flattens in the core (eqn. 3.4).

For the six clusters discussed in §3.4.4 which are more consistent with a power-law, it may be the case that the ICM entropy departs from a power-law at a radial scale smaller than the 5'' bins we used for extracting surface brightness profiles. After extracting new surface brightness profiles for these six clusters using 2.5'' bins and repeating the analysis, we find that the profiles for A4059 and AS0405 do flatten. This leaves A1919, A2151, MS 0116.3-0115, and NGC 507 as the only clusters in *ACCEPT* for which the power-law model cannot be reasonably argued against.

For clusters with central cooling times shorter than the age of the cluster, non-zero core entropy is an expected consequence of episodic heating of the ICM (Voit & Donahue, 2005), with AGN as one possible heating source (Bower, 1997; Loewenstein, 2000; Voit & Bryan, 2001; Churazov et al., 2002; Brüggen & Kaiser, 2002; Brüggen et al., 2002; Nath & Roychowdhury, 2002; Ruszkowski & Begelman, 2002; Alexander, 2002; Omma et al., 2004; McCarthy et al., 2004; Roychowdhury et al., 2004; Hoeft & Brüggen, 2004; Dalla Vecchia et al., 2004; Soker & Pizzolato, 2005; Pizzolato & Soker, 2005; Brighenti & Mathews, 2006; Mathews et al., 2006). Clusters with cooling

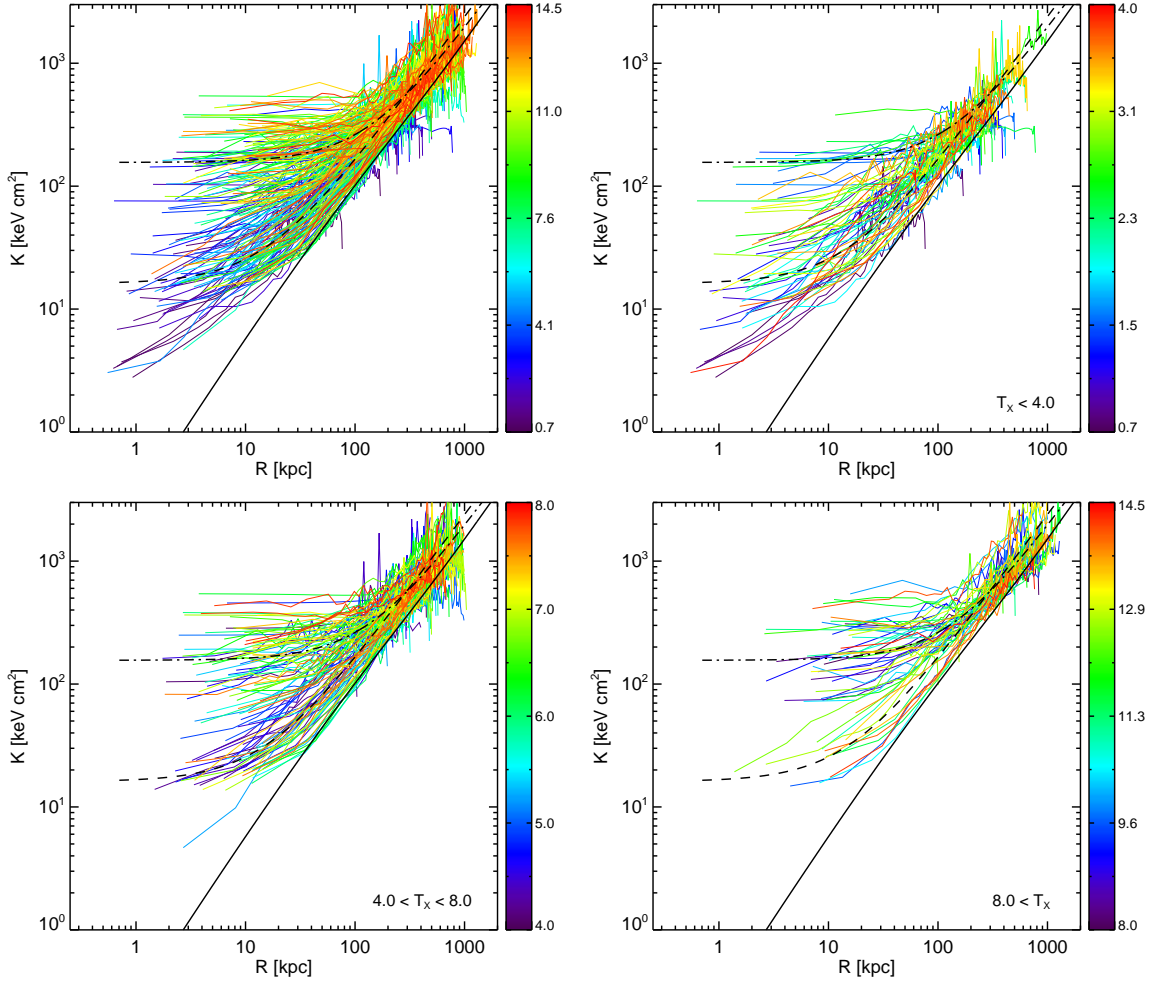


Figure 3.5 Composite plots of entropy profiles for varying cluster temperature ranges. Profiles are color-coded based on average cluster temperature. Units of the color bars are keV. The solid-line is the pure-cooling model of Voit et al. (2002), the dashed-line is the mean profile for clusters with $K_0 \leq 50 \text{ keV cm}^2$, and the dashed-dotted line is the mean profile for clusters with $K_0 > 50 \text{ keV cm}^2$. *Top left:* This panel contains all the entropy profiles in our study. *Top right:* Clusters with $kT_X < 4 \text{ keV}$. *Bottom left:* Clusters with $4 \text{ keV} < kT_X < 8 \text{ keV}$. *Bottom right:* Clusters with $kT_X > 8 \text{ keV}$. Note that while the dispersion of core entropy for each temperature range is large, as the kT_X range increases so to does the mean core entropy.

times of order the age of the Universe, however, require other mechanisms to generate their core entropy, for example via mergers or extremely energetic AGN outbursts. For the very highest K_0 values, $K_0 > 100 \text{ keV cm}^2$, the mechanism by which the core entropy came to be so large is not well understood as it is difficult to boost the entropy of a gas parcel to $> 100 \text{ keV cm}^2$ via merger shocks (McCarthy et al., 2008) and would require AGN outburst energies which have never been observed. We are providing the data and results of *ACCEPT* to the public with the hope that the research community finds it a useful new resource to further understand the processes which result in non-zero cluster core entropy.

3.5.2 BIMODALITY OF CORE ENTROPY DISTRIBUTION

The time required for a gas parcel to radiate away its thermal energy is a function of the gas entropy. Low entropy gas radiates profusely and is thus subject to rapid cooling and vice versa for high entropy gas. Hence, the distribution of K_0 is of particular interest because it is an approximate indicator of the cooling timescale in the cluster core. The K_0 distribution is also interesting because it may be useful in better understanding the physical processes operating in cluster cores. For example, if processes such as thermal conduction and AGN feedback are important in establishing the entropy state of cluster cores, then models which incorporate these processes should approximately reproduce the observed K_0 distribution.

In the top panel of Figure 3.6 is plotted the logarithmically binned distribution of K_0 . In the bottom panel of Figure 3.6 is plotted the cumulative distribution of K_0 . One can immediately see from these distributions that there are at least two distinct populations separated by a small number of clusters with $K_0 \approx 30 - 60 \text{ keV cm}^2$. If the distinct bimodality of the K_0 distribution seen in the binned histogram were an artifact of binning, then the cumulative distribution should be relatively smooth. But there are clearly plateaus in the cumulative distribution, with one of these plateaus

coincident with the division between the two populations at $K_0 \approx 30 - 60 \text{ keV cm}^2$.

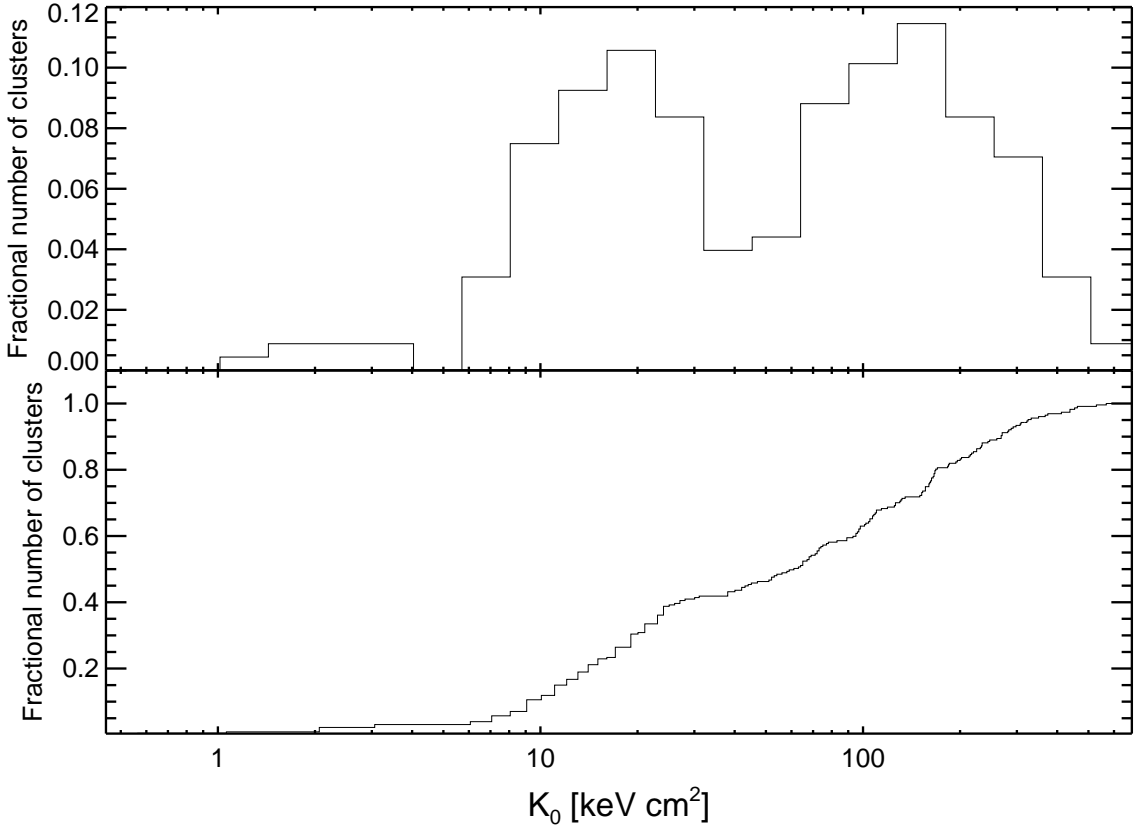


Figure 3.6 *Top panel*: Histogram of best-fit K_0 for all the clusters in *ACCEPT*. Bin widths are 0.15 in log space. *Bottom panel*: Cumulative distribution of K_0 values for the full sample. The distinct bimodality in K_0 is present in both distributions, which would not be seen if it were an artifact of the histogram binning. A KMM test finds the K_0 distribution cannot arise from a simple unimodal Gaussian.

To further test for the presence of a bimodal population we utilized the KMM test of Ashman et al. (1994). The KMM test estimates the probability that a set of data points is better described by the sum of multiple Gaussians than by a single Gaussian. We tested the unimodal case versus the bimodal case, with the assumption that the dispersion of the two Gaussian components are not the same. We have used the updated KMM code of Waters et al. (2008) which incorporates bootstrap resampling to determine uncertainties for all parameters. A post-analysis comparison of fits assuming the populations have the same and different dispersions confirms our initial

guess that the dispersions are different is a better model.

The KMM test, as with any statistical test, is very specific. At zeroth order, the KMM test simply determines if a population is unimodal or not, and finds the means of these populations. However, the dispersions of these populations are subject to the quality of sampling and the presence of outliers (*e.g.* KMM must assign all data points to a population). The outputs of the KMM test are the best-fit populations to the data, not necessarily the best-fit populations of the underlying distribution (hence no goodness of fit is output). However, the KMM test does output a P-value, p , and with the assumption that χ^2 describes the distribution of the likelihood ratio statistic, $1 - p$ is the confidence interval for the null hypothesis.

There are a small number of clusters with $K_0 \leq 4 \text{ keV cm}^2$ that when included in the KMM test significantly change the results. Thus we conducted tests including and excluding $K_0 \leq 4 \text{ keV cm}^2$ clusters and provide two sets of best-fit parameters. The results of the KMM test neglecting $K_0 \leq 4 \text{ keV cm}^2$ clusters were two statistically distinct peaks at $K_1 = 17.8 \pm 6.6 \text{ keV cm}^2$ and $K_2 = 154 \pm 52 \text{ keV cm}^2$. 121 clusters were assigned to the first distribution, while 106 were assigned to the second. Including $K_0 \leq 4 \text{ keV cm}^2$ clusters, the KMM test found populations at $K_1 = 15.0 \pm 5.0 \text{ keV cm}^2$ (89 clusters) and $K_2 = 129 \pm 45 \text{ keV cm}^2$ (131 clusters). The KMM test neglecting $K_0 \leq 4 \text{ keV cm}^2$ clusters returned $p = 1.16 \times 10^{-7}$, while the test including all clusters returned $p = 1.90 \times 10^{-13}$. These tiny p -values indicate the unimodal distribution is significantly rejected as the parent distribution of the observed K_0 distribution.

One possible explanation for a bimodal core entropy distribution is that it arises from the effects of episodic AGN feedback and electron thermal conduction in the cluster core. Voit & Donahue (2005) put forth a model of AGN feedback whereby outbursts of $\sim 10^{45} \text{ ergs s}^{-1}$ occurring every $\sim 10^8 \text{ yrs}$ can maintain a quasi-steady core entropy of $\approx 10 - 30 \text{ keV cm}^2$. In addition, very energetic and infrequent AGN

outbursts of 10^{61} ergs can increase the core entropy into the $\approx 30 - 50$ keV cm 2 range. This model satisfactorily explains the distribution of $K_0 \lesssim 50$ keV cm 2 , but depletion of the $K_0 = 30 - 60$ keV cm 2 region and populating $K_0 > 60$ keV cm 2 requires more physics. Voit et al. (2008) have recently suggested that the dramatic fall-off of clusters beginning at $K_0 \approx 30$ keV cm 2 may be the result of electron thermal conduction. After K_0 has gone beyond $K_0 \approx 30$ keV cm 2 , conduction could severely slow, if not halt, a cluster’s core from appreciably cooling and returning to a core entropy state with $K_0 < 30$ keV cm 2 . This model is supported by results presented in Chapter 4, Guo et al. (2008), and Rafferty et al. (2008) which find that the formation of thermal instabilities are extremely sensitive to the core entropy state of a cluster.

We acknowledge that *ACCEPT* is not a complete, uniformly selected sample of clusters. This raises the possibility that our sample is biased towards clusters that have historically drawn the attention of observers, such as cooling flows or mergers. If that were the case, then one reasonable explanation of the K_0 bimodality is that $K_0 = 30 - 60$ keV cm 2 clusters are “boring” and thus go unobserved. However, as we show in §3.5.4, the unbiased flux-limited *HIFLUGCS* sample is also bimodal. A sociological explanation of bimodality for both *ACCEPT* and *HIFLUGCS* is highly unlikely.

3.5.3 THE *HIFLUGCS* SUB-SAMPLE

ACCEPT is not a flux-limited or volume-limited sample. To ensure our results are not affected by an unknown selection bias, we culled the *HIFLUGCS* sample from *ACCEPT* for separate analysis. *HIFLUGCS* is a flux-limited sample ($f_X \geq 2 \times 10^{-11}$ ergs s $^{-1}$ cm $^{-2}$) selected by flux only from the *REFLEX* sample (Böhringer et al., 2004) with no consideration of morphology. Thus, at any given luminosity in *HIFLUGCS* there is a good sampling of different morphologies, *i.e.* the bias toward cool-cores or mergers has been removed. The sample also covers most of the sky

with holes near Virgo and the Large and Small Magellanic Clouds, and has no known incompleteness (Chen et al., 2007). There are a total of 106 objects in *HIFLUGCS*: 63 in the primary sample and 43 in the extended sample. Of these 106 objects, no public *Chandra* observations were available for 16 objects (A548e, A548w, A1775, A1800, A3528n, A3530, A3532, A3560, A3695, A3827, A3888, AS0636, HCG 94, IC 1365, NGC 499, RXCJ 2344.2-0422), 6 objects did not meet our minimum analysis requirements and were thus insufficient for study (3C 129, A1367, A2634, A2877, A3627, Triangulum Australis), and as discussed in §3.2, Coma and Fornax were intentionally ignored. This left a total of 82 *HIFLUGCS* objects which we analyzed, 59 from the primary sample ($\sim 94\%$ complete) and 23 from the extended sample ($\sim 50\%$ complete). The primary sample is the more complete of the two, thus we focus our following discussion on the primary sample only.

The clusters missing from the primary *HIFLUGCS* sample are A1367, A2634, Coma, and Fornax. The extent to which these 4 clusters can change our analysis of the K_0 distribution for *HIFLUGCS* is limited. To alter or wash-out bimodality, all 4 clusters would need to fall in the range $K_0 = 20 - 40 \text{ keV cm}^2$, which is certainly not the case for any of these clusters. A1367 has been studied by Donnelly et al. (1998) and Sun & Murray (2002), with both finding that two sub-clusters are merging in the cluster. The merger process, and the potential for associated shock formation, is known to create large increases of gas entropy (McCarthy et al., 2007). Given the combination of low surface brightness, moderate temperatures ($kT_X = 3.5 - 5.0 \text{ keV}$), lack of a temperature gradient, ongoing merger, and presence of a shock, it is unlikely A1367 has a core entropy $\lesssim 40 \text{ keV cm}^2$. A2634 is a very low surface brightness cluster with the bright radio source 3C 465 at the center of an X-ray coronae (Sun et al., 2007). Clusters with comparable properties to A2634 are not found to have $K_0 \lesssim 40 \text{ keV cm}^2$. Coma and Fornax are known to have core entropy $> 40 \text{ keV cm}^2$ (Rafferty et al., 2008, C. Scharf, private communication).

Shown in Figure 3.7 are the log-binned (top panel) and cumulative (bottom panel) K_0 distributions of the *HIFLUGCS* primary sample. The bimodality seen in the full *ACCEPT* collection is also present in the *HIFLUGCS* sub-sample. Mean best-fit parameters are given in Table ???. We again performed two KMM tests: one test with, and another test without, clusters having $K_0 \leq 4 \text{ keV cm}^2$. For the test including $K_0 \leq 4 \text{ keV cm}^2$ clusters we find populations at $K_1 = 9.7 \pm 3.5 \text{ keV cm}^2$ (28 clusters) and $K_2 = 131 \pm 46 \text{ keV cm}^2$ (31 clusters) with $p = 3.34 \times 10^{-3}$. Excluding clusters with $K_0 \leq 4 \text{ keV cm}^2$ we find peaks at $K_1 = 10.5 \pm 3.4 \text{ keV cm}^2$ and $K_2 = 116 \pm 42 \text{ keV cm}^2$, each having 21 and 34 clusters, respectively. The probability these populations are best described by a unimodal distribution is $p = 1.55 \times 10^{-5}$.

Hudson & Reiprich (2007) note a similar core entropy bimodality to the one we find here. Hudson & Reiprich (2007) discuss two distinct groupings of objects in a plot of average cluster temperature versus core entropy, with the dividing point being $K \approx 40 \text{ keV cm}^2$. Shown in the left panel of Figure 3.8 is a reproduction of the Hudson & Reiprich (2007) figure except using results from our analysis. Our results agree with the findings of Hudson & Reiprich (2007) with the gap in K_0 occurring at $K_0 \approx 40 \text{ keV cm}^2$. While the gaps of *ACCEPT* and *HIFLUGCS* do not cover the same K_0 range, it is interesting that both gaps are the deepest around $K_0 \approx 30 \text{ keV cm}^2$. That bimodality is present in both *ACCEPT* and the unbiased *HIFLUGCS* sub-sample suggests bimodality cannot be the result of simple archival bias.

3.5.4 DISTRIBUTION OF CORE COOLING TIMES

In the X-ray regime, cooling time and entropy are related in that decreasing gas entropy also means shorter cooling time. Thus, if the K_0 distribution is bimodal, the distribution of cooling times should also be bimodal. We have calculated cooling time

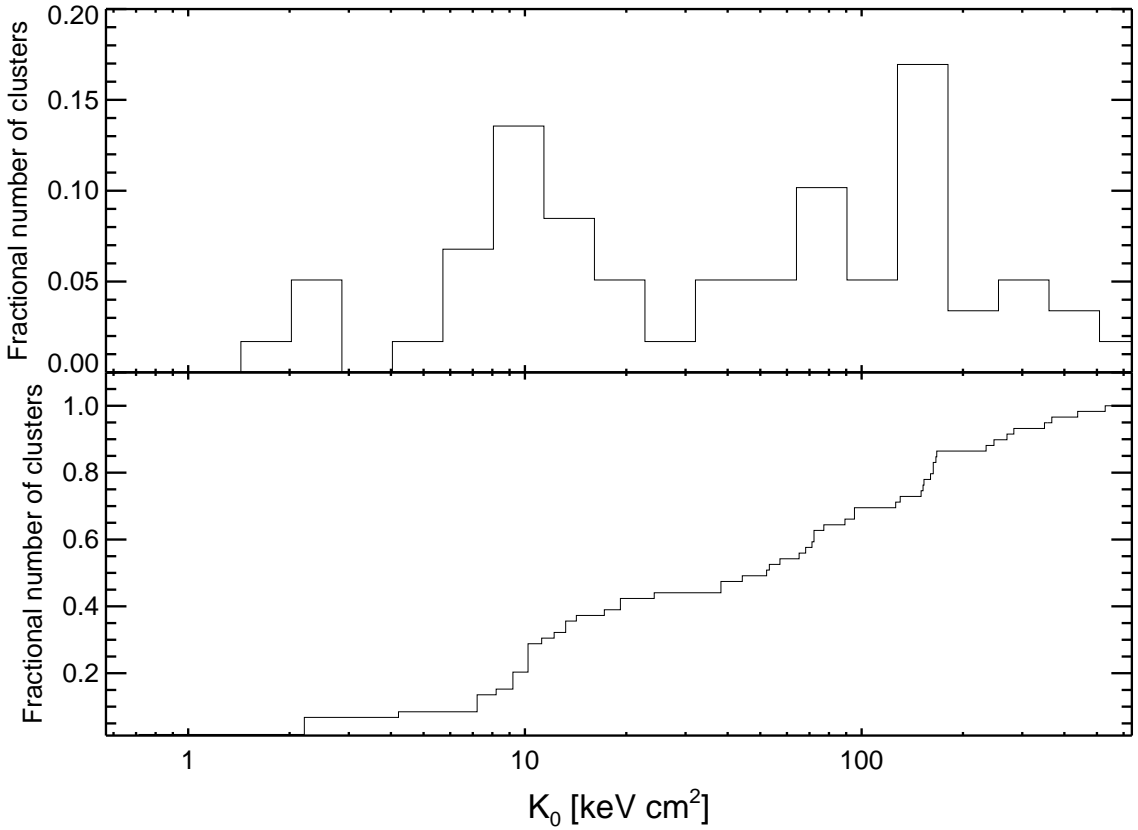


Figure 3.7 *Top panel:* Histogram of best-fit K_0 values for the primary *HIFLUGCS* sample. Bin widths are 0.15 in log space. *Bottom panel:* Cumulative distribution of best-fit K_0 values. The distinct bimodality seen in the full *ACCEPT* sample (Fig. 3.6) is also present in the *HIFLUGCS* subsample and shares the same gap starting at $K_0 \approx 30 \text{ keV cm}^2$. That bimodality is present in both samples is strong evidence it is not a result of an unknown archival bias.

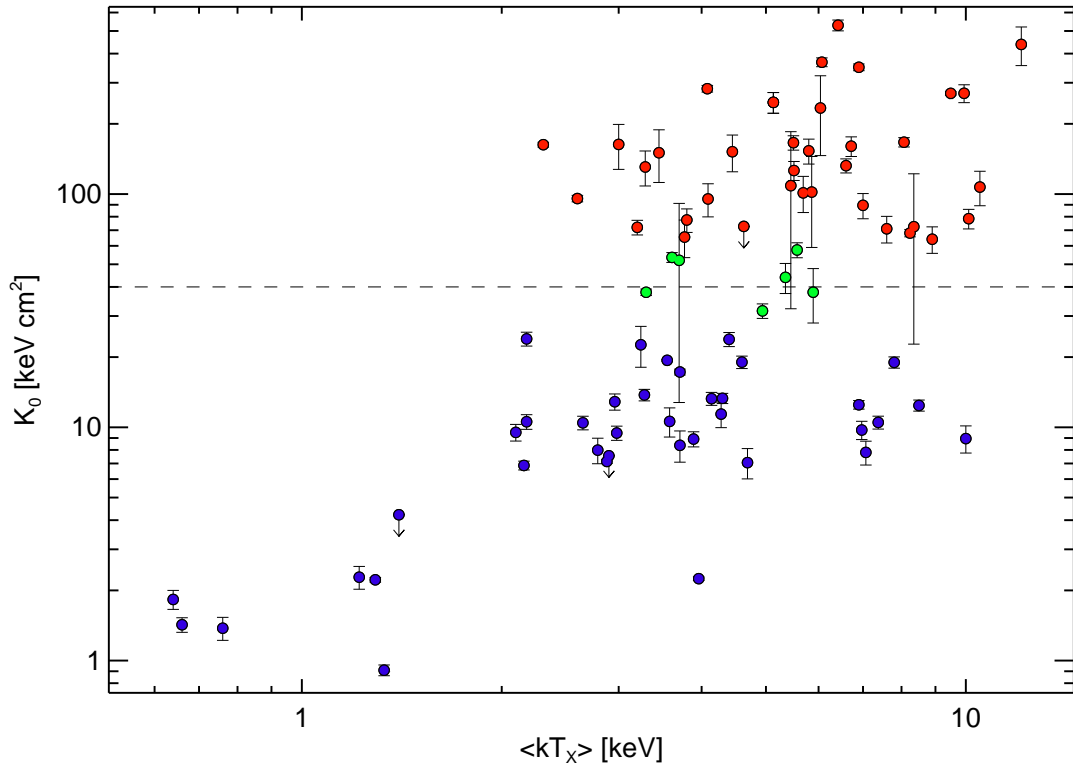


Figure 3.8 Best-fit K_0 versus average cluster temperature for all the objects in *HIFLUGCS* sample we have analyzed. This figure is a reproduction of the Hudson & Reiprich (2007) figure except using our best-fit K_0 values for the *HIFLUGCS* clusters which we analyzed. We have color-coded for the points based on the K_0 value: blue points are $K_0 \leq 30 \text{ keV cm}^2$, green points have $30 \text{ keV cm}^2 < K_0 \leq 60 \text{ keV cm}^2$, and red points have $K_0 > 60 \text{ keV cm}^2$. The dashed line marks $K_0 = 40 \text{ keV cm}^2$. In both panels the dashed lines mark $K = 40 \text{ keV cm}^2$. We do not know if the same clusters are shown in both plots, but the bimodality noted in Hudson & Reiprich (2007) is also evident in our data and occurs at approximately the same location along the entropy axis.

profiles from the spectral analysis using the relation

$$t_{\text{cool}} = \frac{3nkT_X}{2n_e n_H \Lambda(T, Z)} \quad (3.7)$$

where n is the total ion number ($\approx 2.3n_H$ for a fully ionized plasma), n_e and n_H are the electron and proton densities respectively, $\Lambda(T, Z)$ is the cooling function for a given temperature and metal abundance, and $3/2$ is a constant associated with isochoric cooling. The values of the cooling function for each temperature profile bin were calculated in XSPEC using the flux of the best-fit spectral model. Following the procedure discussed in §3.3.4, Λ and kT_X were interpolated across the radial grid of the electron density profile. The cooling time profiles were then fit with a simple model analogous to that used for fitting $K(r)$:

$$t_{\text{cool}}(r) = t_{c0} + t_{100} \left(\frac{r}{100 \text{ kpc}} \right)^\alpha \quad (3.8)$$

where t_{c0} is core cooling time and t_{100} is a normalization at 100 kpc.

The K_0 distribution can also be used to explore the distribution of core cooling times. Assuming free-free interactions are the dominant gas cooling mechanism (*i.e.* $\epsilon \propto T^{1/2}$), Donahue et al. (2005) show that entropy is related to cooling time via the formulation:

$$t_{c0}(K_0) \approx 10^8 \text{ yrs} \left(\frac{K_0}{10 \text{ keV cm}^2} \right)^{3/2} \left(\frac{kT_X}{5 \text{ keV}} \right)^{-1}. \quad (3.9)$$

Shown in Figure 3.9 is the logarithmically binned and cumulative distributions of best-fit core cooling times from eqn. 3.8 (top panel) and core cooling times calculated using eqn. 3.9 (bottom panel). The bin widths in both histograms are 0.20 in log-space. The pile-up of cluster core cooling times below 1 Gyr is well known, *e.g.* Hu et al. (1985) and more recently Dunn & Fabian (2008), and the cooling times we

calculate are consistent with the results of other cooling time studies, *e.g.* Peres et al. (1998) and Rafferty et al. (2008).

Most important about Fig. 3.9 is that the distinct bimodality of the K_0 distribution is also present in best-fit core cooling time, t_{c0} . A KMM bimodality test of t_{c0} found peaks at $t_{c1} = 0.60 \pm 0.24$ Gyr and $t_{c2} = 6.23 \pm 2.19$ Gyr with 130 and 97 in each respective population. The probability that the unimodal distribution is a better fit is once again exceedingly small, $p = 8.77 \times 10^{-7}$.

But while t_{c0} is bimodal, the gaps in the t_{c0} and $t_{c0}(K_0)$ are offset from each other. The gap in t_{c0} occurs in the range $\sim 1 - 2$ Gyrs, while the gap in $t_{c0}(K_0)$ occurs in the range $\sim 0.7 - 1.0$. It is also interesting that the bimodality in $t_{c0}(K_0)$ is more abrupt and deeper than it is in t_{c0} . The offset gaps and differing sharpness of the two distributions suggests that while bimodality occurs only below a particular cooling time scale ($t_{c0} \lesssim 1$ Gyr), a short core cooling time may not be the fundamental property responsible for bimodality. If entropy is more closely related to the physical processes which cause bimodality than is cooling time, then that the cooling time distribution does not present with the sharp, deep bimodality seen in K_0 suggests entropy is the fundamental quantity related to bimodality.

But, since cooling time profiles are more sensitive to the resolution of the temperature profiles than are the entropy profiles, it may be that resolution effects are limiting the quantification of the true cooling time of the core. For example, if our temperature interpolation scheme is too coarse, or averaging over many small-scale temperature fluctuations significantly increases t_{c0} , then t_{c0} would not be the best approximation of true core cooling time. In which case, the core cooling times might be lower and the sharpness and offsets of the distributions gaps may significantly change.

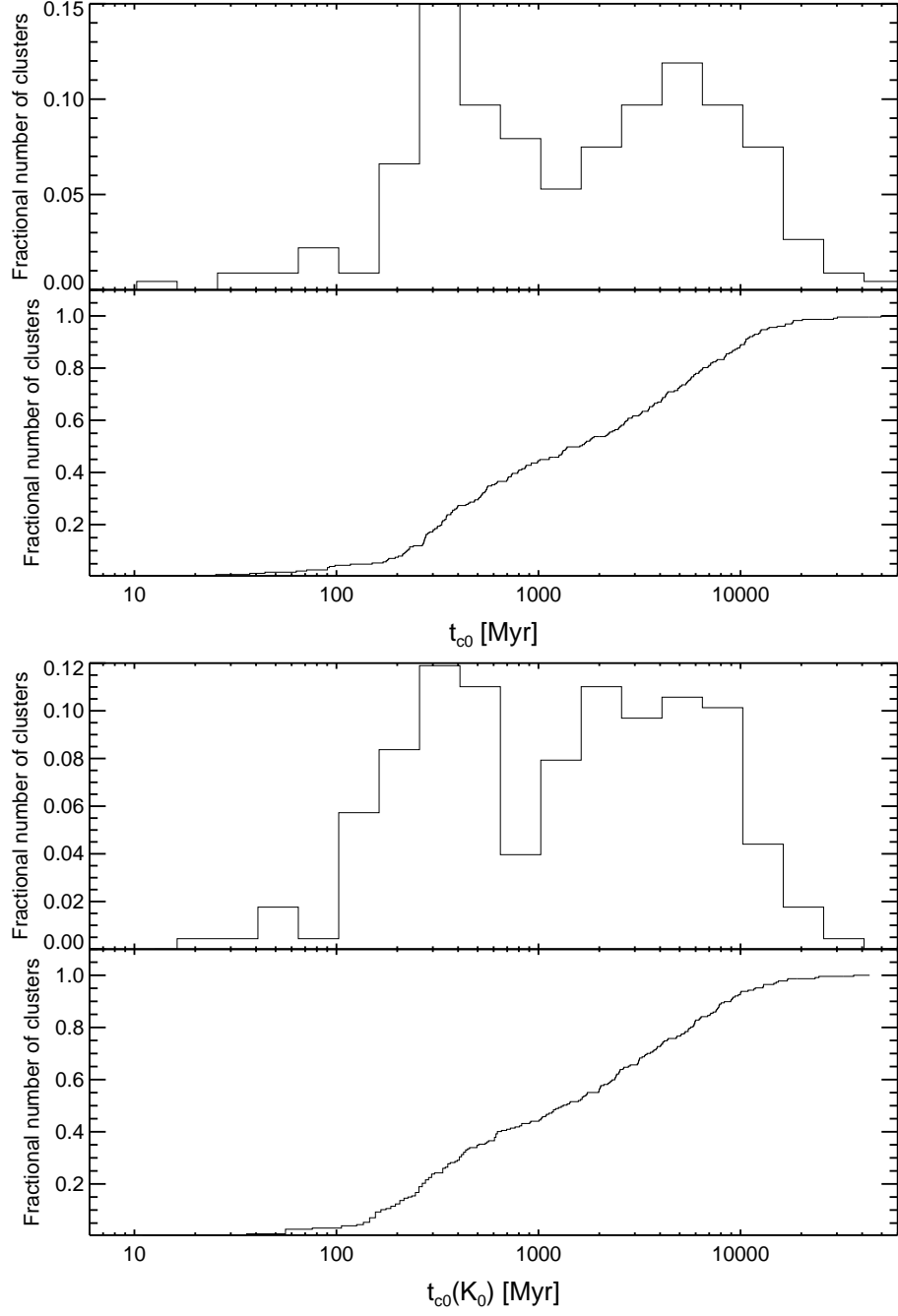


Figure 3.9 (

Top panel:) Log-binned histogram and cumulative distribution of best-fit core cooling times, t_{c0} (eqn. 3.8), for all the clusters in ACCEPT. Histogram bin widths are 0.2 in log space. (**Bottom panel:**) Log-binned histogram and cumulative distribution of core cooling times calculated from best-fit K_0 values, $t_{c0}(K_0)$ (eqn. 3.9), for all the clusters in ACCEPT. Histogram bin widths are 0.2 in log space. The bimodality we observe in the K_0 distribution is also present in best-fit t_{c0} . However, the gaps between the two populations of t_{c0} and $t_{c0}(K_0)$ differ by ~ 0.3 Gyrs with scaled-entropy having the more pronounced gap with a shorter cooling time.

3.5.5 SLOPE AND NORMALIZATION OF POWER-LAW COMPONENTS

Beyond $r \approx 100$ kpc the entropy profiles show a striking similarity in the slope of the power-law component which is independent of K_0 . For the full sample, the mean value of $\alpha = 1.21 \pm 0.39$. For clusters with $K_0 < 50$ keV cm 2 , the mean $\alpha = 1.20 \pm 0.38$, and for clusters with $K_0 \geq 50$ keV cm 2 , the mean $\alpha = 1.23 \pm 0.40$. Our mean slope of $\alpha \approx 1.2$ is not statistically different from the theoretical value of 1.1 found by Tozzi & Norman (2001). For the full sample, the mean value of $K_{100} = 126 \pm 45$ keV cm 2 . Again distinguishing between clusters below and above $K_0 = 50$ keV cm 2 , we find $K_{100} = 150 \pm 50$ keV cm 2 and $K_{100} = 107 \pm 39$ keV cm 2 , respectively. Scaling each entropy profile by the cluster virial temperature and virial radius considerably reduces the dispersion in K_{100} , but we reserve detailed discussion of scaling relations for future work.

3.6 SUMMARY AND CONCLUSIONS

We have presented intracluster medium entropy profiles for a sample of 233 galaxy clusters (9.66 Msec) taken from the *Chandra* Data Archive. We have named this project *ACCEPT* for “Archive of Chandra Cluster Entropy Profile Tables.” Our analysis software, reduced data products, data tables, figures, cluster images, and results of our analysis for all clusters and observations are freely available at the *ACCEPT* web site: <http://www.pa.msu.edu/astro/MC2/accept>. We encourage observers and theorists to utilize this library of entropy profiles in their own work.

We created radial temperature profiles using spectra extracted from a minimum of three concentric annuli containing 2500 counts each and extending to either the chip edge or $0.5R_{180}$, whichever was smaller. We deprojected surface brightness profiles extracted from 5'' bins over the energy range 0.7-2.0 keV to obtain the electron gas density as a function of radius. Entropy profiles were calculated from the density

and temperature profiles as $K(r) = T(r)n(r)^{-2/3}$. Two models for the entropy distribution were then fit to each profile: a power-law only model (eqn. 3.5) and a power-law which approaches a constant value at small radii (eqn. 3.4).

We have demonstrated that the entropy profiles for the majority of *ACCEPT* clusters are well-represented by the model which approaches a constant entropy, K_0 , in the core. The entropy profiles of *ACCEPT* are also remarkably similar at radii greater than 100 kpc, and asymptotically approach the self-similar pure-cooling curve ($r \propto 1.1$) with a slope of $\alpha = 1.21 \pm 0.39$ (the dispersion here is in the sample, not in the uncertainty of the measurement). We also find that the distribution of K_0 for the full archival sample is bimodal with the two populations separated by a poorly populated region at $K_0 \approx 30 - 60$ keV cm². After culling out the primary *HIFLUGCS* sub-sample of Reiprich (2001), we find the K_0 distribution of this complete sub-sample to be bimodal, refuting the possibility of archival bias.

Two core cooling times were derived for each cluster: (1) cooling time profiles were calculated using eqn. 3.7 and each cooling time profile was then fit with eqn. 3.8 returning a best-fit core cooling time, t_{c0} ; (2) Using best-fit K_0 values, entropy was converted to a core cooling time, $t_{c0}(K_0)$ using eqn. 3.9. We find the distributions of both core cooling times to be bimodal. Comparison of the core cooling times from method (1) and (2) reveals that the gap in the bimodal cooling time distributions occur over different timescales, $\sim 2 - 3$ Gyrs for t_{c0} , and $\sim 0.7 - 1$ for $t_{c0}(K_0)$, and that the bimodality of $t_{c0}(K_0)$ is more abrupt. We speculate these two results indicate ICM entropy, and not ICM cooling time, is the fundamental quantity related to bimodality.

After analyzing an ensemble of artificially redshifted entropy profiles, we find the lack of $K_0 \lesssim 10$ keV cm² clusters at $z > 0.1$ is most likely a result of resolution effects. Investigation of possible systematics affecting best-fit K_0 values, such as profile curvature and number of profile bins, revealed no trends which would significantly

affect our results. We come to the conclusion that K_0 is an acceptable measure of average core entropy and is not overly influenced by profile shape or radial resolution. We also find that $\sim 90\%$ of the sample clusters have a best-fit K_0 more than 3σ away from zero.

Our results regarding non-zero core entropy and K_0 bimodality fit nicely into the sharpening picture of how feedback and radiative cooling in clusters alter global cluster properties and affect massive galaxy formation. Among the many models of AGN feedback, Voit & Donahue (2005) put forth a model which specifically addresses how AGN outbursts generate and sustain non-zero core entropy in the regime of $K_0 \lesssim 70 \text{ keV cm}^2$. In addition, if electron thermal conduction is an important process in clusters, Donahue et al. (2005), Voit & Donahue (2005), and Voit et al. (2008) propose there exists a critical entropy threshold below which conduction is no longer efficient at wiping out thermal instabilities. The consequences of which should be a bimodal core entropy distribution and a sensitivity of cooling by-product formation (like star formation and AGN activity) to this entropy threshold. We show in Chapter 4 that indicators of feedback like H α and radio emission are extremely sensitive to the lower-bound of the bimodal gap at $K_0 \approx 30 \text{ keV cm}^2$. If mergers and some other unknown mechanism are capable of producing cluster cores with $K_0 > 70 \text{ keV cm}^2$ and $> 100 \text{ keV cm}^2$, then taking all of these processes in concert, a closed-loop picture of the ICM's entropy life-cycle is starting to emerge.

However, the details are still missing and there are many open questions regarding the evolution of the ICM and formation of thermal instabilities in cluster cores: How are clusters with $K_0 > 100 \text{ keV cm}^2$ produced, is fine-tuned pre-heating still the answer? What are the role of MHD instabilities, *e.g.* MTI (Balbus, 2000; Quataert, 2008) and HBI (Parrish & Quataert, 2008), in shaping the ICM? Are the compact X-ray sources we find at the cores of some BCGs truly coronae? If so, how did they form and survive in the harsh ICM? And can their properties be used to constrain

the effects of conduction? We hope *ACCEPT* will be a useful resource in answering these questions.

3.7 ACKNOWLEDGEMENTS

K. W. C. thanks Chris Waters for supplying and supporting his new KMM bimodality code. K. W. C. was supported in this work through *Chandra* X-ray Observatory Archive grants AR-6016X and AR-4017A. M. D. acknowledges support from the NASA LTSA program NNG-05GD82G. The *Chandra* X-ray Observatory Center is operated by the Smithsonian Astrophysical Observatory for and on behalf of NASA under contract NAS8-03060. This research has made use of software provided by the Chandra X-ray Center in the application packages CIAO, CHIPS, and SHERPA. This research has made use of the NASA/IPAC Extragalactic Database which is operated by the Jet Propulsion Laboratory, California Institute of Technology, under contract with NASA. This research has also made use of NASA's Astrophysics Data System. Some software was obtained from the High Energy Astrophysics Science Archive Research Center, provided by NASA's Goddard Space Flight Center.

3.8 SUPPLEMENTAL CLUSTER NOTES

NB: In this section we abbreviate surface brightness as SB.

Abell 119 ($z = 0.0442$): This is a highly diffuse cluster without a prominent cool core. The large core region and slowly varying SB made deprojection highly unstable. We have excluded a small source at the very center of the BCG. The exclusion region for the source is $\approx 2.2''$ in radius which at the redshift of the cluster is ~ 2 kpc. This cluster required a double β -model.

Abell 160 ($z = 0.0447$): The highly asymmetric, low SB of this cluster resulted in a noisy surface brightness profile that could not be deprojected. This cluster

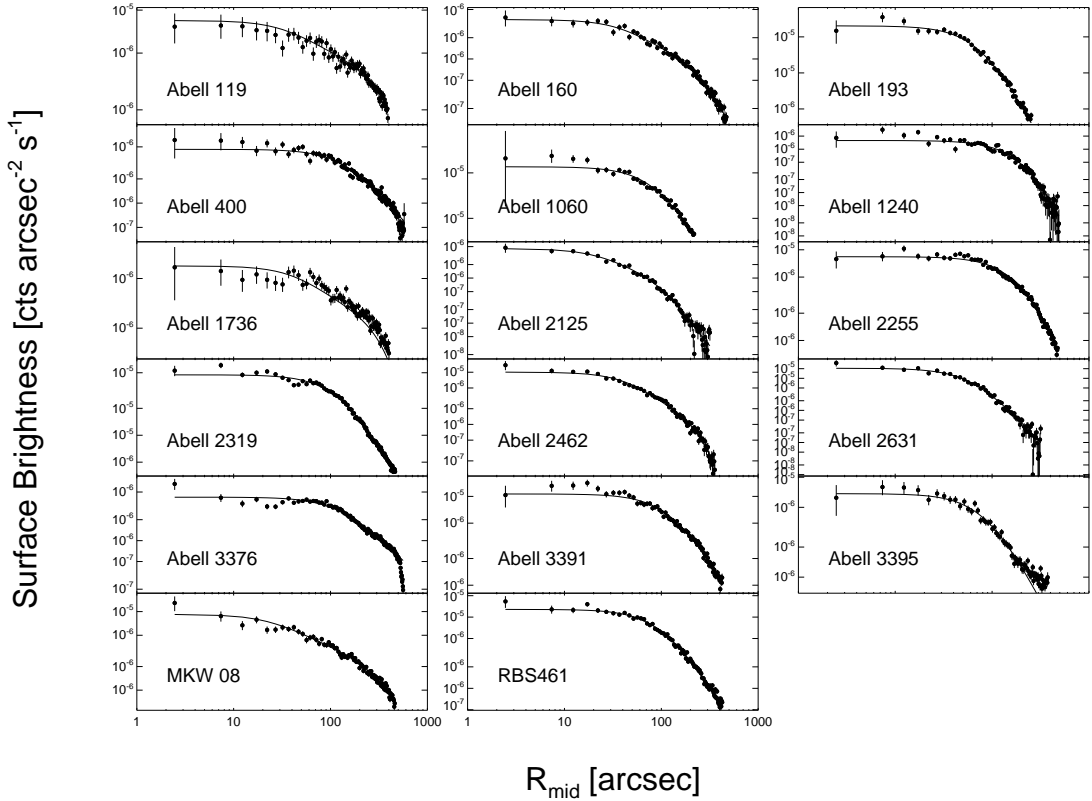


Figure 3.10 Surface brightness profiles for clusters requiring a β -model fit. The best-fit β -model for each cluster is overplotted as a dashed line. The discrepancy between the data and best-fit model for some clusters results from the presence of a compact X-ray source at the center of the cluster. These cases are discussed below.

required a double β -model. The BCG hosts a compact X-ray source. The exclusion region for the compact source has a radius of $\sim 5''$ or ~ 4.3 kpc. The BCG for this cluster is not coincident with the X-ray centroid and hence is not at the zero-point of our radial analysis.

Abell 193 ($z = 0.0485$): This cluster has an azimuthally symmetric and a very diffuse ICM centered on a BCG which is interacting with a companion galaxy. In Fig. 3.10 one can see that the central three bins of this cluster's SB profile are highly discrepant from the best-fit β -model. This is a result of the BCG being coincident with a bright, compact X-ray source. As we have concluded in 3.3.5, compact X-ray sources are excluded from our analysis as they are not the focus of our study here. Hence we have used the best-fit β -model in deriving $K(r)$ instead of the raw SB.

Abell 400 ($z = 0.0240$): The two ellipticals at the center of this cluster have compact X-ray sources which are excluded during analysis. The core entropy we derive for this cluster is in agreement with that found by Hudson et al. (2006) which supports the accuracy of the β -model we have used.

Abell 1060 ($z = 0.0125$): There is a distinct compact source associated with the BCG in this cluster. The ICM is also very faint and uniform in surface brightness making the compact source that much more obvious. Deprojection was unstable because of imperfect exclusion of the source.

Abell 1240 ($z = 0.1590$): The SB of this cluster is well-modeled by a β -model. There is nothing peculiar worth noting about the BCG or the core of this cluster.

Abell 1736 ($z = 0.0338$): Another “boring” cluster with a very diffuse low SB ICM, no peaky core, and no signs of merger activity in the X-ray. The noisy SB profile

necessitated the use of a double β -model. The BCG is coincident with a very compact X-ray source, but the BCG is offset from the X-ray centroid and thus the central bins are not adversely affected. The radius of the exclusion region for the compact source is $\approx 2.3''$ or 1.5 kpc.

Abell 2125 ($z = 0.2465$): Although the ICM of this cluster is very similar to the other clusters listed here (*i.e.* diffuse, large cores), A2125 is one of the more compact clusters. The presence of several merging sub-clusters (Wang et al., 1997, 2004a) to the NW of the main cluster form a diffuse mass which cannot rightly be excluded. This complication yields inversions of the deprojected SB profile if a double β -model is not used.

Abell 2255 ($z = 0.0805$): This is a very well studied merger cluster (Burns et al., 1995; Feretti et al., 1997a). The core of this cluster is very large ($r > 200$ kpc). Such large extended cores cannot be deprojected using our methods because if too many neighboring bins have approximately the same SB, deprojection results in bins with negative or zero value. The SB for this cluster is well modeled as a β function.

Abell 2319 ($z = 0.0562$): A2319 is another well studied merger cluster (Feretti et al., 1997b; Molendi et al., 1999) with a very large core region ($r > 100$ kpc) and a prominent cold front (O’Hara et al., 2004). Once again, the SB profile is well-fit by a β -model.

Abell 2462 ($z = 0.0737$): This cluster is very similar in appearance to A193: highly symmetric ICM with a bright, compact X-ray source embedded at the center of an extended diffuse ICM. The central compact source has been excluded from our analysis with a region of radius $\approx 1.5''$ or ~ 3 kpc. The central bin of the SB profile is most likely boosted above the best-fit double β -model because of faint extended emission from the compact source which cannot be discerned

from the ambient ICM.

Abell 2631 ($z = 0.2779$): The SB profile for this cluster is rather regular, but because the cluster has a large core it suffers from the same unstable deprojection as A2255 and A2319. The ICM is symmetric about the BCG and is incredibly uniform in the core region. We did not detect or exclude a source at the center of this cluster, but under heavy binning the cluster image appears to have a source coincident with the BCG, and the slightly higher flux in central bin of the SB profile may be a result of an unresolved source.

Abell 3376 ($z = 0.0456$): The large core of this cluster ($r > 120$ kpc) makes deprojection unstable and a β -model must be used.

Abell 3391 ($z = 0.0560$): The BCG is coincident with a compact X-ray source. The source is excluded using a region with radius $\approx 2''$ or ~ 2 kpc. The large uniform core region made deprojection unstable and thus required a β -model fit.

Abell 3395 ($z = 0.0510$): The SB profile for this cluster is noisy resulting in deprojection inversions and requiring a β -model fit. The BCG of this cluster has a compact X-ray source and this source was excluded using a region with radius $\approx 1.9''$ or ~ 2 kpc.

MKW 08 ($z = 0.0270$): MKW 08 is a nearby large group/poor cluster with a pair of interacting elliptical galaxies in the core. The BCG falls directly in the middle of the ACIS-I detector gap. However, despite the lack of proper exposure, CCD dithering reveals that a very bright X-ray source is associated with the BCG. A double β -model was necessary for this cluster because the low SB of the ICM is noisy and deprojection is unstable.

RBS 461 ($z = 0.0290$): This is another nearby large group/poor cluster with an extended, diffuse, axisymmetric, featureless ICM centered on the BCG. The

BCG is coincident with a compact source with size $r \approx 1.7$ kpc. This source was excluded during reduction. The β -model is a good fit to the SB profile.

Chapter Four

Cavagnolo, Kenneth W., Donahue, Megan, Voit, G. Mark, Sun, Ming (2008). An Entropy Threshold for Strong H α and Radio Emission in the Cores of Galaxy Clusters. The Astrophysical Journal Letters. 0:000-000.

NB: This chapter is an accepted publication which has not yet been assigned a journal bibliographic code.

CHAPTER 4:

AN ENTROPY THRESHOLD FOR

STRONG H α AND RADIO

EMISSION IN THE CORES OF

GALAXY CLUSTERS

4.1 INTRODUCTION

In recent years the “cooling flow problem” has been the focus of intense scrutiny as the solutions have broad impact on our theories of galaxy formation (see Peterson & Fabian, 2006, for a review). Current models predict that the most massive galaxies in the Universe – brightest cluster galaxies (BCGs) – should be bluer and more massive than observations find, unless AGN feedback intervenes to stop late-time star formation (Bower et al., 2006; Croton et al., 2006; Saro et al., 2006). X-ray observations of galaxy clusters have given this hypothesis considerable traction. From the properties of X-ray cavities in the intracluster medium (ICM), Bîrzan et al. (2004) concluded that AGN feedback provides the necessary energy to retard cooling in the cores of clusters (see McNamara & Nulsen, 2007, for a review). This result suggests that, under the right conditions, AGN are capable of quenching star formation by heating the surrounding ICM.

If AGN feedback is indeed responsible for regulating star formation in cluster cores, then the radio and star-forming properties of galaxy clusters should be related to the distribution of ICM specific entropy. In previous observational work (see Donahue

et al., 2005, 2006, and Chapter 3), we have focused on ICM entropy as a means for understanding the cooling and heating processes in clusters because it is a more fundamental property of the ICM than temperature or density alone (Voit et al., 2002; Voit, 2005). ICM temperature mainly reflects the depth and shape of the dark matter potential well, while entropy depends more directly on the history of heating and cooling within the cluster and determines the density distribution of gas within that potential.

We have therefore undertaken a large *Chandra* archival project to study how the entropy structure of clusters correlates with other cluster properties. Chapter 3 presents the radial entropy profiles we have measured for a sample of 233 clusters taken from the *Chandra* Data Archive. We have named this project the Archive of Chandra Cluster Entropy Profile Tables, or *ACCEPT* for short. To characterize the ICM entropy distributions of the clusters, we fit the equation $K(r) = K_0 + K_{100}(r/100 \text{ kpc})^\alpha$ to each entropy profile. In this equation, K_{100} is the normalization of the power-law component at 100 kpc and we refer to K_0 as the central entropy. Bear in mind, however, that K_0 is not necessarily the minimum core entropy or the entropy at $r = 0$, nor is it the gas entropy which would be measured immediately around the AGN or in a BCG X-ray coronae. Instead, K_0 represents the typical excess of core entropy above the best fitting power-law found at larger radii. Chapter 3 shows that K_0 is non-zero for almost all clusters in our sample.

In this chapter we present the results of exploring the relationship between the expected by-products of cooling, *e.g.* H α emission, star formation, and AGN activity, and the K_0 values of clusters in our survey. To determine the activity level of feedback in cluster cores, we selected two readily available observables: H α and radio emission. We have found that there is a critical entropy level below which H α and radio emission are often present, while above this threshold these emission sources are much fainter and in most cases undetected. Our results suggest that the formation of thermal

instabilities in the ICM and initiation of processes such as star formation and AGN activity are closely connected to core entropy, and we suspect that the sharp entropy threshold we have found arises from thermal conduction (Voit et al., 2008).

This chapter proceeds in the following manner: In §4.2 we cover the basics of our data analysis. The entropy-H α relationship is discussed in §4.3, while the entropy-radio relationship is discussed in §4.4. A brief summary is provided in §4.5. For this chapter we have assumed a flat Λ CDM Universe with cosmogony $\Omega_M = 0.3$, $\Omega_\Lambda = 0.7$, and $H_0 = 70 \text{ km s}^{-1} \text{ Mpc}^{-1}$. All uncertainties are 90% confidence.

4.2 DATA ANALYSIS

This section briefly describes our data reduction and methods for producing entropy profiles. More thorough explanations are given in Donahue et al. (2006), Chapter 2, and Chapter 3.

4.2.1 X-RAY

X-ray data was taken from publicly available observations in the *Chandra* Data Archive. Following standard CIAO reduction techniques¹, data was reprocessed using CIAO 3.4.1 and CALDB 3.4.0, resulting in point source and flare clean events files at level-2. Entropy profiles were derived from the radial ICM temperature and electron density profiles.

Radial temperature profiles were created by dividing each cluster into concentric annuli with the requirement of at least three annuli containing a minimum of 2500 counts each. Source spectra were extracted from these annuli, while corresponding background spectra were extracted from blank-sky backgrounds tailored to match each observation. Each blank-sky background was corrected to account for variation of the hard-particle background, while spatial variation of the soft-galactic back-

¹<http://cxc.harvard.edu/ciao/guides/>

ground was accounted for through addition of a fixed background component during spectral fitting. Weighted responses which account for spatial variations of the CCD calibration were also created for each observation. Spectra were then fit over the energy range 0.7-7.0 keV in XSPEC 11.3.2ag (Arnaud, 1996) using a single-component absorbed thermal model.

Radial electron density profiles were created using surface brightness profiles and spectroscopic information. Exposure-corrected, background-subtracted, point-source-clean surface brightness profiles were extracted from 5'' concentric annular bins over the energy range 0.7-2.0 keV. In conjunction with the spectroscopic normalization and 0.7-2.0 keV count rate, surface brightness was converted to electron density using the deprojection technique of Kriss et al. (1983). Errors were estimated using 5000 Monte Carlo realizations of the surface brightness profile.

A radial entropy profile for each cluster was then produced from the temperature and electron density profiles. The entropy profiles were fit with a simple model which is a power-law at large radii and approaches a constant value, K_0 , at small radii (see §4.1 for the equation). We define central entropy as K_0 from the best-fit model.

4.2.2 H α

One goal of our project was to determine if ICM entropy is connected to processes like star formation. Here we do not directly measure star formation but instead use H α , which is usually a strong indicator of ongoing star formation in galaxies (Kennicutt, 1983). It is possible that some of the H α emission from BCGs is not produced by star formation (Begelman & Fabian, 1990; Sparks et al., 2004; Ruszkowski et al., 2008; Ferland et al., 2008). Nevertheless, H α emission unambiguously indicates the presence of $\sim 10^4$ K gas in the cluster core and therefore the presence of a multiphase intracluster medium that could potentially form stars.

Our H α values have been gathered from several sources, most notably Crawford

et al. (1999). Additional sources of data are M. Donahue's observations taken at Las Campanas and Palomar (see Table ??), Heckman et al. (1989), Donahue et al. (1992), Lawrence et al. (1996), Valluri & Anupama (1996), White et al. (1997), Crawford et al. (2005), and Quillen et al. (2008). We have recalculated the H α luminosities from these sources using our assumed Λ CDM cosmological model. However, the observations were made with a variety of apertures and in many cases may not reflect the full H α luminosity of the BCG. The exact levels of $L_{\text{H}\alpha}$ are not important for the purposes of this chapter and we use the $L_{\text{H}\alpha}$ values here as a binary indicator of multiphase gas: either H α emission and cool gas are present or they are not.

4.2.3 RADIO

Another goal of this work was to explore the relationship between ICM entropy and AGN activity. It has long been known that BCGs are more likely to host radio-loud AGN than other cluster galaxies (Burns et al., 1981; Valentijn & Bijleveld, 1983; Burns, 1990). Thus, we chose to interpret radio emission from the BCG of each *ACCEPT* cluster as a sign of AGN activity.

To make the radio measurements, we have taken advantage of the nearly all-sky flux-limited coverage of the NRAO VLA Sky Survey (NVSS Condon et al., 1998) and Sydney University Molonglo Sky Survey (SUMSS Bock et al., 1999; Mauch et al., 2003). NVSS is a continuum survey at 1.4 GHz of the entire sky north of $\delta = -40^\circ$, while SUMSS is a continuum survey at 843 MHz of the entire sky south of $\delta = -30^\circ$. The completeness limit of NVSS is ≈ 2.5 mJy and for SUMSS it is ≈ 10 mJy when $\delta > -50^\circ$ or ≈ 6 mJy when $\delta \leq -50^\circ$. The NVSS positional uncertainty for both right ascension and declination is $\lesssim 1''$ for sources brighter than 15 mJy, and $\approx 7''$ at the survey detection limit (Condon et al., 1998). At $z = 0.2$, these uncertainties represent distances on the sky of $\sim 3 - 20$ kpc. For SUMSS, the positional uncertainty is $\lesssim 2''$ for sources brighter than 20 mJy, and is always less than $10''$ (Bock et al., 1999;

Mauch et al., 2003). The distance at $z = 0.2$ associated with these uncertainties is $\sim 6 - 30$ kpc. We calculate the radio power for each radio source using the standard relation $\nu L_\nu = 4\pi D_L^2 S_\nu f_0$ where S_ν is the 1.4 GHz or 843 MHz flux from NVSS or SUMSS, D_L is the luminosity distance, and f_0 is the central beam frequency of the observations. Our calculated radio powers are simply an approximation of the bolometric radio luminosity.

Radio sources were found using two methods. The first method was to search for sources within a fixed angular distance of $20''$ around the cluster X-ray peak. The probability of randomly finding a radio source within an aperture of $20''$ is exceedingly low (< 0.004 for NVSS). Thus, in 233 total field searches, we expect to find no more than one spurious source. The second method involved searching for sources within 20 projected kpc of the cluster X-ray peak. At $z \approx 0.051$, $1''$ equals 1 kpc, thus for clusters at $z \gtrsim 0.05$, the 20 kpc aperture is smaller than the $20''$ aperture, and the likelihood of finding a spurious source gets smaller. Both methods produce nearly identical lists of radio sources with the differences arising from the very large, extended lobes of low-redshift radio sources such as Hydra A.

To make a spatial and morphological assessment of the radio emission's origins, *i.e.* determining if the radio emission is associated with the BCG, high angular resolution is necessary. However, NVSS and SUMSS are low-resolution surveys with FWHM of $\approx 45''$. We therefore cannot distinguish between ghost cavities/relics, extended lobes, point sources, re-accelerated regions, or if the emission is coming from a galaxy very near the BCG. We have handled this complication by visually inspecting each radio source in relation to the optical (using DSS I/II²) and infrared (using 2MASS³) emission of the BCG. We have used this method to establish that the radio emission is most likely coming from the BCG. When available, high resolution data from

²<http://archive.stsci.edu/dss/>

³<http://www.ipac.caltech.edu/2mass/>

VLA FIRST⁴ was added to the visual inspection. VLA FIRST is a 10,000 \square° high-resolution (5'') survey at 20 cm of the North and South Galactic caps (Becker et al., 1995). FIRST is also more sensitive than either NVSS or SUMSS with a detection threshold of 1 mJy.

4.3 H α EMISSION AND CENTRAL ENTROPY

Of the 233 clusters in *ACCEPT*, we located H α observations from the literature for 110 clusters. Of those 110, H α was detected in 46, while the remaining 64 have upper limits. The mean central entropy for clusters with detections is $K_0 = 13.9 \pm 4.9$ keV cm 2 , and for clusters with only upper-limits $K_0 = 130 \pm 55$ keV cm 2 .

In Figure 4.1 central entropy is plotted versus H α luminosity. One can immediately see the dichotomy between clusters with and without H α emission. If a cluster has a central entropy $\lesssim 30$ keV cm 2 then H α emission is usually “on”, while above this threshold the emission is predominantly “off”. For brevity we refer to this threshold as K_{thresh} hereafter. The cluster above K_{thresh} which has H α emission (blue square with inset orange circle) is Zwicky 2701 ($K_0 = 39.7 \pm 3.9$ keV cm 2). There are also clusters below K_{thresh} without H α emission (blue squares with red stars): A2029, A2107, EXO 0422-086, and RBS 533. A2151 also lies below K_{thresh} and has no detected H α emission, but the best-fit K_0 for A2151 is statistically consistent with zero and this cluster is plotted using the 2σ upper-limit of K_0 (green triangle in Fig. 4.1). These five clusters are clearly exceptions to the much larger trend. The mean and dispersion of the redshifts for clusters with and without H α are not significantly different, $z = 0.124 \pm 0.106$ and $z = 0.132 \pm 0.084$ respectively, and applying a redshift cut (*i.e.* $z = 0 - 0.15$ or $z = 0.15 - 0.3$) does not change the K_0 -H α dichotomy. Most important to note is that changes in the H α luminosities because of aperture effects will move points up or down in Figure 4.1, while mobility along the K_0 axis is

⁴<http://sundog.stsci.edu>

minimal. Qualitatively, the correlation between low central entropy and presence of H α emission is very robust.

The clusters with H α detections are typically between 10–30 keV cm 2 , have short central cooling times (< 1 Gyr), and under older nomenclature would be classified as “cooling flow” clusters. It has long been known that star formation and associated H α nebulosity appear only in cluster cores with cooling times less than a Hubble time (Hu et al., 1985; Johnstone et al., 1987; McNamara & O’Connell, 1989; Voit & Donahue, 1997; Cardiel et al., 1998). However, our results suggest that the central cooling time must be at least a factor of 10 smaller than a Hubble time for these manifestations of cooling and star formation to appear. It is also very interesting that the characteristic entropy threshold for strong H α emission is so sharp. Voit et al. (2008) have recently proposed electron thermal conduction may be responsible for setting this threshold. This hypothesis has received further support from the theoretical work of Guo et al. (2008) showing that thermal conduction can stabilize non-cool core clusters against the formation of thermal instabilities, and that AGN feedback may be required to limit star formation when conduction is insufficient.

4.4 RADIO SOURCES AND CENTRAL ENTROPY

Of the 233 clusters in *ACCEPT*, 100 have radio-source detections with a mean K_0 of 23.3 ± 9.4 keV cm 2 , while the other 122 clusters with only upper limits have a mean K_0 of 134 ± 52 keV cm 2 . NVSS and SUMSS are low resolution surveys with FWHM at $\approx 45''$ which at $z = 0.2$ is ≈ 150 kpc. This scale is larger than the size of a typical cluster cooling region and makes it difficult to determine absolutely that the radio emission is associated with the BCG. We therefore focus only on clusters at $z < 0.2$. After the redshift cut, 135 clusters remain – 64 with radio detections (mean $K_0 = 18.3 \pm 7.7$ keV cm 2) and 71 without (mean $K_0 = 112 \pm 45$ keV cm 2).

In Figure 4.2 we have plotted radio power versus K_0 . The obvious dichotomy

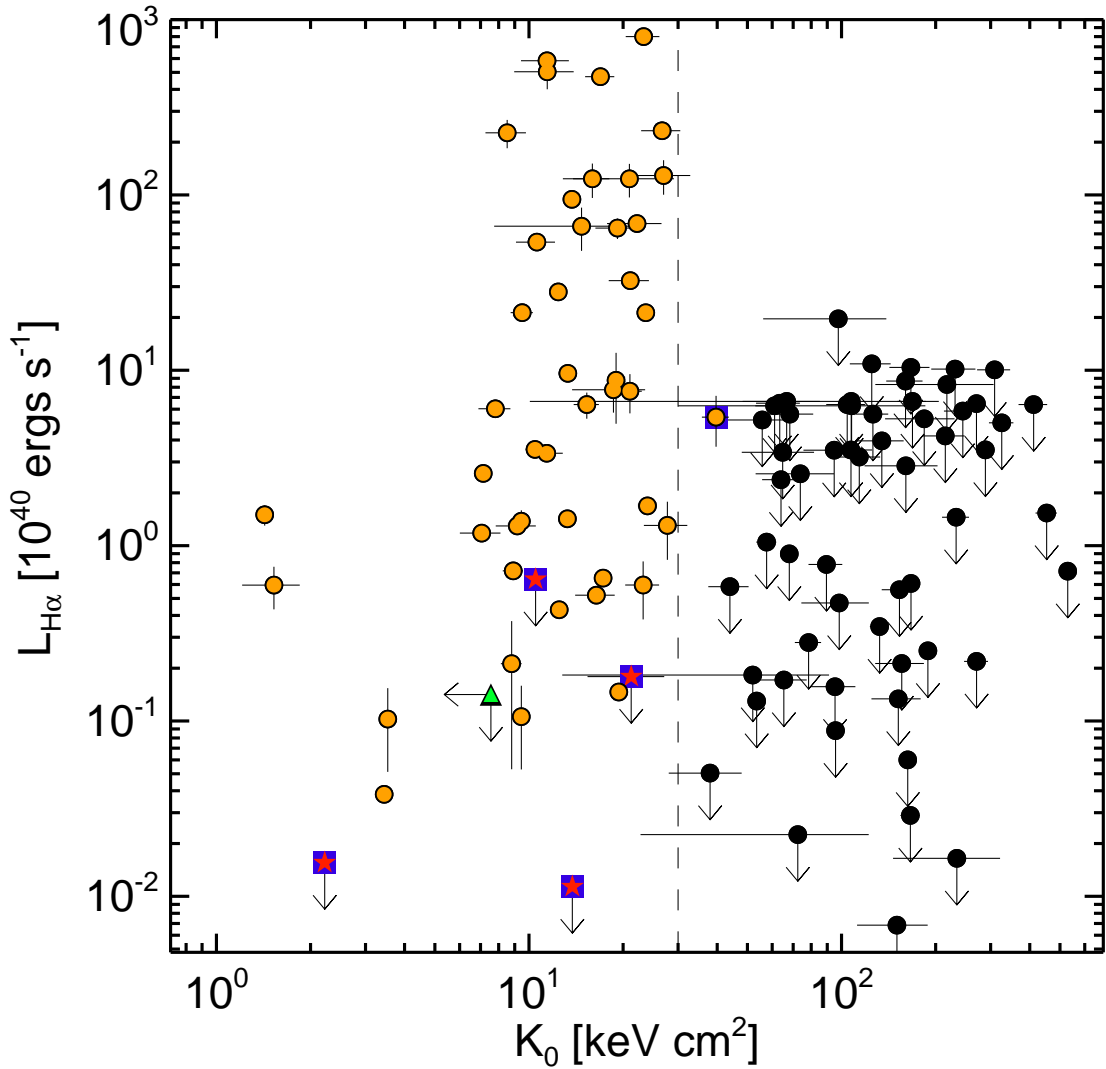


Figure 4.1 Central entropy vs. H α luminosity. Orange circles represent H α detections, black circles are non-detection upper limits, and blue squares with inset red stars or orange circles are peculiar clusters which do not adhere to the observed trend (see text). A2151 is plotted using the 2σ upper-limit of the best-fit K_0 and is denoted by a green triangle. The vertical dashed line marks $K_0 = 30 \text{ keV cm}^2$. Note the presence of a sharp H α detection dichotomy beginning at $K_0 \lesssim 30 \text{ keV cm}^2$.

seen in the H α measures and characterized by K_{thresh} , is also present in the radio. Clusters with $\nu L_\nu \gtrsim 10^{40}$ ergs s $^{-1}$ generally have $K_0 \lesssim K_{\text{thresh}}$. This trend was first evident in Donahue et al. (2005) and suggests that AGN activity in BCGs, while not exclusively limited to clusters with low core entropy, is much more likely to be found in clusters which have a core entropy less than K_{thresh} . That star formation and AGN activity are subject to the same entropy threshold suggests the mechanism which promotes or initiates one is also involved in the activation of the other. If the entropy of the hot gas in the vicinity of the AGN is correlated with K_0 , then the lack of correlation between radio power and K_0 below the 30 keV cm 2 threshold suggests that cold-mode accretion (Pizzolato & Soker, 2005; Hardcastle et al., 2007) may be the dominant method of fueling AGN in BCGs.

We have again highlighted exceptions to the general trend seen in Figure 4.2: clusters below K_{thresh} without a radio source (blue squares with inset red stars) and clusters above K_{thresh} with a radio source (blue squares with inset orange circles). The peculiar clusters below K_{thresh} are A133, A539, A1204, A2107, A2556, AWM7, ESO 5520200, MKW4, MS J0440.5+0204, and MS J1157.3+5531. The peculiar clusters above K_{thresh} are 2PIGG J0011.5-2850, A193, A586, A2063, A2147, A2244, A3558, A4038, and RBS 461. In addition, there are three clusters, A2151, AS405, MS 0116.3-0115, which have best-fit K_0 statistically consistent with zero and are plotted in Fig. 4.2 using the 2σ upper-limit of K_0 (green triangles). All three of these clusters have detected radio sources.

Finding a few clusters in our sample without radio sources where we expect to find them is not surprising given that AGN feedback could be episodic. However, the clusters above K_{thresh} with a central radio source are interesting, and may be special cases of BCGs with embedded coronae. Sun et al. (2007) extensively studied coronae and found they are like “mini-cooling cores” with low temperatures and high densities. Coronae are a low-entropy environment isolated from the high-entropy ICM and may

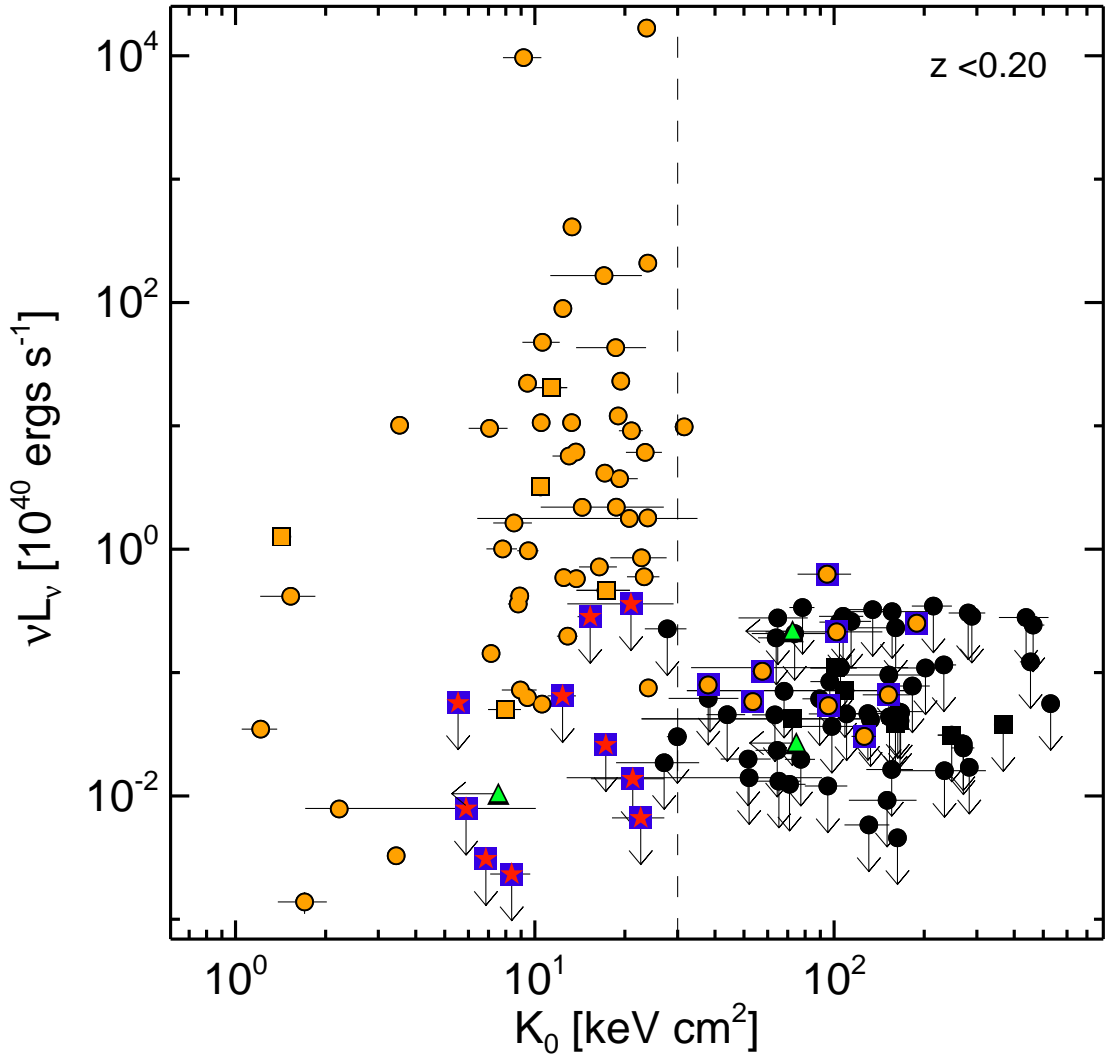


Figure 4.2 BCG radio power vs. K_0 for clusters with $z < 0.2$. Orange symbols represent radio detections and black symbols are non-detection upper-limits. Circles are for NVSS observations and squares are for SUMSS observations. The blue squares with inset red stars or orange circles are peculiar clusters which do not adhere to the observed trend (see text). Green triangles denote clusters plotted using the 2σ upper-limit of the best-fit K_0 . The vertical dashed line marks $K_0 = 30 \text{ keV cm}^2$. The radio sources show the same trend as H α : bright radio emission is preferentially “on” for $K_0 \lesssim 30 \text{ keV cm}^2$.

provide the conditions necessary for gas cooling to proceed. And indeed, 2PIGG 0011, A193, A2151, A2244, A3558, A4038, and RBS 461 show indications that a very compact ($r \lesssim 5$ kpc) X-ray source is associated with the BCG (see Section 3.3.5).

4.5 SUMMARY

We have presented a comparison of ICM central entropy values and measures of BCG H α and radio emission for a *Chandra* archival sample of galaxy clusters. We find that below a characteristic central entropy threshold of $K_0 \approx 30$ keV cm 2 , H α and bright radio emission are more likely to be detected, while above this threshold H α is not detected and radio emission, if detected at all, is significantly fainter. The mean K_0 for clusters with and without H α detections are $K_0 = 13.9 \pm 4.9$ keV cm 2 and $K_0 = 130 \pm 55$ keV cm 2 , respectively. For clusters at $z < 0.2$ with BCG radio emission the mean $K_0 = 18.3 \pm 7.7$ keV cm 2 , while for BCGs with only upper limits, the mean $K_0 = 112 \pm 45$ keV cm 2 . While other mechanisms can produce H α or radio emission besides star formation and AGN, if one assumes the H α and radio emission are coming from these two feedback sources, then our results suggest the development of multiphase gas in cluster cores (which can fuel both star formation and AGN) is strongly coupled to ICM entropy.

4.6 ACKNOWLEDGEMENTS

We were supported in this work through Chandra SAO grants AR-4017A, AR-6016X, G05-6131X and NASA/LTSA grant NNG-05GD82G. The CXC is operated by the SAO for and on behalf of NASA under contract NAS8-03060.

CHAPTER 5: SUMMARY

5.1 ENERGY BAND DEPENDENCE OF X-RAY TEMPERATURES

Using a sample of 192 galaxy clusters we explored the band dependence of inferred X-ray temperatures for the ICM. Utilizing core-excised global cluster spectra extracted from the regions encircled by R_{2500} and R_{5000} , we inferred X-ray temperatures for a single-component absorbed thermal model in a broadband (0.7-7.0 keV) and a hard-band (2.0-7.0 keV). On average, we found that the hard-band temperatures were greater, with the ratio of the temperatures, T_{HBR} , having a mean value 1.16 ± 0.01 (where the error is of the mean) for the R_{2500} apertures, and 1.14 ± 0.01 for the R_{5000} apertures. No systematic trends were found, in either the values or dispersions, with S/N, redshift, Galactic absorption, metallicity, observation date, or broadband temperature. Analysis of a simulated ensemble of 12,765 observation-specific two-component spectra revealed statistical fluctuations could not account for the skewing measured in T_{HBR} . The simulations also helped establish a lower-limit on the flux contribution from a cooler gas component ($T_X < 2.0$ keV) necessary to generate T_{HBR} as large as those found in the data. A second cool gas phase must be contributing $\gtrsim 10\%$ of the total emission. The simulations also reveal the observational scatter is larger than the statistical scatter, a result one should expect if an underlying physical process is responsible for creating dispersion in T_{HBR} .

The *a priori* motivation for studying temperature inhomogeneity comes from the prediction of Mathiesen & Evrard (2001) that T_{HBR} may be related to the process of hierarchical structure formation. After assuming that the establishment and prominence of a cool core in a cluster is an indicator of relaxation, we compared T_{HBR} values with the “strength” of the cool core based on the temperature decrement between the core and the cluster atmosphere. The result was a significant correlation between clusters having higher values of T_{HBR} being less likely to host a cool core. A search of the scientific literature involving the clusters with the highest significant values of T_{HBR} ($T_{HBR} > 1.1$) revealed that most, if not all, of these clusters are undergoing, or have recently undergone, a merger event. With two strong connections between T_{HBR} and cluster dynamical state established, we conclude that temperature inhomogeneity is most likely related to the process of cluster relaxation, and that it may be useful as a metric to further quantify the degree to which a cluster is relaxed, thus addressing point (1) brought up in Section §1.3.1.

5.2 CHANDRA ARCHIVAL SAMPLE OF INTRACLUSTER ENTROPY PROFILES

A library of ICM entropy profiles for 233 galaxy clusters taken from the *Chandra* Data Archive were created to better understand the role of feedback and cooling in shaping global cluster properties. Radial gas density, $n_e(r)$, and gas temperature, $kT_x(r)$, profiles were created for each cluster. Radial entropy was calculated from the relation $K(r) = kT_X(r)n_e(r)^{-2/3}$. The uncertainties for each profile were calculated using 5000 Monte Carlo realizations of the observed surface brightness profile. Each profile was then fit with two models: one which is a power-law at all radii (3.5), and another (eqn. 3.5) which is a power-law at large radii but approaches a constant K_0 value at small radii. The K_0 term is defined as the core entropy.

Comparison of p-values, χ^2 , and the significance of K_0 above zero for the best-fit models revealed that for 90% of the 233 sample, the model with a constant core entropy is a better description of the data. Systematics such as PSF smearing, angular resolution, profile curvature, and number of radial bins proved not to be important in setting or changing best-fit K_0 . The slope of the power-law component was also found to be remarkably similar among the profiles with a mean value of 1.21 ± 0.39 which is not significantly different from the value of ~ 1.1 expected from hierarchical structure formation.

The distribution of K_0 for both the *ACCEPT* and *HIFLUGCS* samples was found to be bimodal. The populations comprising the bimodality are strikingly similar between the two samples with peaks at $K_0 \sim 15 \text{ keV cm}^2$ and $K_0 \sim 150 \text{ keV cm}^2$. The KMM test (Ashman et al., 1994; Waters et al., 2008) was applied and it determined, for both *ACCEPT* and *HIFLUGCS*, that the populations were statistically distinct and that a unimodal distribution was ruled out. The poorly populated region between the populations for both samples occurred at $K_0 \approx 30 - 60 \text{ keV cm}^2$ with a distinct jump at $K_0 \approx 30 \text{ keV cm}^2$. The measured entropy profile shapes and distribution of K_0 were consistent with existing models of AGN feedback which predict non-zero core entropy. All of the results and data for *ACCEPT* were made available to the public with the intent that theorists and observers might find utility for *ACCEPT* in their own work. The work presented in Chapter 3 directly addressed point (2) of Section §1.3.2.

5.3 AN ENTROPY THRESHOLD FOR STRONG H α AND RADIO EMISSION IN THE CORES OF GALAXY CLUS- TERS

To study a suspected connection between low entropy gas in cluster cores and the by-products of cooling, namely AGN activity and formation of thermal instabilities, the best-fit K_0 values from clusters in *ACCEPT* were compared against radio power and H α luminosity, both strong indicators of run-away cooling. A search of the research literature turned-up H α observations for 110 clusters in *ACCEPT*. The NVSS and SUMSS all-sky radio surveys were queried for each cluster to attain νL_ν , either detections or upper-limits. New luminosities were then calculated using the preferred cosmology assumed in this dissertation to place all observations on equal footing.

A comparison of H α luminosities and best-fit K_0 values showed a strong relation between when H α emission is detected and when it is not. Below an entropy threshold of $K_0 \lesssim 30$ keV cm 2 H α emission is predominantly on, while above this threshold it is always off sans the exception of one cluster very near the $K_0 = 30$ keV cm 2 boundary. A very similar correlation was found between νL_ν and K_0 for clusters at $z < 0.2$. A redshift cut was applied because of the low resolution of NVSS and SUMSS. The entropy threshold for νL_ν also occurs at $K_0 \approx 30$ keV cm 2 but with a larger fraction of low power radio sources above $K_0 \approx 30$ keV cm 2 than the fraction which was found in H α . However, it was found that powerful radio sources ($\nu L_\nu > 10^{40}$ ergs s $^{-1}$ cm $^{-2}$) were only found in clusters with $K_0 \lesssim 30$ keV cm 2 adding strength to the argument that entropy sets a scale for development of a multiphase medium in cluster cores. While the discussion is not presented in this dissertation, Voit et al. (2008) propose that it is electron thermal conduction that sets the entropy threshold observed in so many clusters. The work presented in Chapter 4 is an extension of point (2) in §1.3.2.

To conserve paper, 81 pages of data tables and the 17 page ‘CORP’ manual have been omitted from this hardcopy. Tables and manual can be found in the electronic version of this dissertation available at:

<http://www.pa.msu.edu/people/cavagnolo/thesis.pdf>

BIBLIOGRAPHY

REFERENCES

- Akritas, M. G., & Bershady, M. A. 1996, *ApJ*, 470, 706
- Alexander, P. 2002, *MNRAS*, 335, 610
- Allen, S. W., & Fabian, A. C. 1998a, *MNRAS*, 297, L57
- . 1998b, *MNRAS*, 297, L63
- Allen, S. W., Fabian, A. C., Johnstone, R. M., White, D. A., Daines, S. J., Edge, A. C., & Stewart, G. C. 1993, *MNRAS*, 262, 901
- Anders, E., & Grevesse, N. 1989, *Geochim. Cosmochim. Acta*, 53, 197
- Antonucci, R., & Barvainis, R. 1994, *AJ*, 107, 448
- Arnaud, K. A. 1996, in *ASP Conf. Ser.* 101: *Astronomical Data Analysis Software and Systems V*, ed. G. H. Jacoby & J. Barnes, 17–+
- Arnaud, M., Aghanim, N., & Neumann, D. M. 2002, *A&A*, 389, 1
- Arnaud, M., & Evrard, A. E. 1999, *MNRAS*, 305, 631
- Ashman, K. M., Bird, C. M., & Zepf, S. E. 1994, *AJ*, 108, 2348
- Balbus, S. A. 2000, *ApJ*, 534, 420
- Balestra, I., Tozzi, P., Ettori, S., Rosati, P., Borgani, S., Mainieri, V., Norman, C., & Viola, M. 2007, *A&A*, 462, 429
- Bauer, F. E., Fabian, A. C., Sanders, J. S., Allen, S. W., & Johnstone, R. M. 2005, *MNRAS*, 359, 1481
- Becker, R. H., White, R. L., & Helfand, D. J. 1995, *ApJ*, 450, 559
- Begelman, M. C., & Fabian, A. C. 1990, *MNRAS*, 244, 26P
- Bialek, J. J., Evrard, A. E., & Mohr, J. J. 2001, *ApJ*, 555, 597
- Binney, J., & Tabor, G. 1995, *MNRAS*, 276, 663
- Bîrzan, L., Rafferty, D. A., McNamara, B. R., Wise, M. W., & Nulsen, P. E. J. 2004, *ApJ*, 607, 800
- Blumenthal, G. R., Faber, S. M., Primack, J. R., & Rees, M. J. 1984, *Nature*, 311, 517
- Bock, D. C.-J., Large, M. I., & Sadler, E. M. 1999, *AJ*, 117, 1578

- Böhringer, H., Schuecker, P., Guzzo, L., Collins, C. A., Voges, W., Cruddace, R. G., Ortiz-Gil, A., Chincarini, G., De Grandi, S., Edge, A. C., MacGillivray, H. T., Neumann, D. M., Schindler, S., & Shaver, P. 2004, *A&A*, 425, 367
- Böhringer, H., Schuecker, P., Pratt, G. W., Arnaud, M., Ponman, T. J., Croston, J. H., Borgani, S., Bower, R. G., Briel, U. G., Collins, C. A., Donahue, M., Forman, W. R., Finoguenov, A., Geller, M. J., Guzzo, L., Henry, J. P., Kneissl, R., Mohr, J. J., Matsushita, K., Mullis, C. R., Ohashi, T., Pedersen, K., Pierini, D., Quintana, H., Raychaudhury, S., Reiprich, T. H., Romer, A. K., Rosati, P., Sabirli, K., Temple, R. F., Viana, P. T. P., Vikhlinin, A., Voit, G. M., & Zhang, Y.-Y. 2007, *A&A*, 469, 363
- Borgani, S., Governato, F., Wadsley, J., Menci, N., Tozzi, P., Quinn, T., Stadel, J., & Lake, G. 2002, *MNRAS*, 336, 409
- Borgani, S., Rosati, P., Tozzi, P., Stanford, S. A., Eisenhardt, P. R., Lidman, C., Holden, B., Della Ceca, R., Norman, C., & Squires, G. 2001, *ApJ*, 561, 13
- Bower, R. G. 1997, *MNRAS*, 288, 355
- Bower, R. G., Benson, A. J., Lacey, C. G., Baugh, C. M., Cole, S., & Frenk, C. S. 2001, *MNRAS*, 325, 497
- Bower, R. G., Benson, A. J., Malbon, R., Helly, J. C., Frenk, C. S., Baugh, C. M., Cole, S., & Lacey, C. G. 2006, *MNRAS*, 370, 645
- Brightenti, F., & Mathews, W. G. 2006, *ApJ*, 643, 120
- Brüggen, M., & Kaiser, C. R. 2002, *Nature*, 418, 301
- Brüggen, M., Kaiser, C. R., Churazov, E., & Enßlin, T. A. 2002, *MNRAS*, 331, 545
- Bryan, G. L., & Norman, M. L. 1998, *ApJ*, 495, 80
- Bucher, S. 2007, Prospects and Issues for a Fifteen Year Chandra Lifetime
—. 2008, *Chandra News*, 15, 21
- Buote, D. A., & Tsai, J. C. 1995, *ApJ*, 452, 522
—. 1996, *ApJ*, 458, 27
- Burns, J. O. 1990, *AJ*, 99, 14
- Burns, J. O., Hallman, E. J., Gantner, B., Motl, P. M., & Norman, M. L. 2008, *ApJ*, 675, 1125
- Burns, J. O., Roettiger, K., Pinkney, J., Perley, R. A., Owen, F. N., & Voges, W. 1995, *ApJ*, 446, 583
- Burns, J. O., White, R. A., & Hough, D. H. 1981, *AJ*, 86, 1

- Canizares, C. R., Clark, G. W., Jernigan, J. G., & Markert, T. H. 1982, ApJ, 262, 33
- Cardiel, N., Gorgas, J., & Aragon-Salamanca, A. 1998, MNRAS, 298, 977
- Cash, W. 1979, ApJ, 228, 939
- Cavagnolo, K. W., Donahue, M., Voit, G. M., & Sun, M. 2008, ApJ, 682, 821
- Cavaliere, A., & Fusco-Femiano, R. 1978, A&A, 70, 677
- Cavaliere, A., Menci, N., & Tozzi, P. 1999, MNRAS, 308, 599
- Chen, Y., Reiprich, T. H., Böhringer, H., Ikebe, Y., & Zhang, Y.-Y. 2007, A&A, 466, 805
- Churazov, E., Sunyaev, R., Forman, W., & Böhringer, H. 2002, MNRAS, 332, 729
- Clarke, T. E., Blanton, E. L., & Sarazin, C. L. 2004, ApJ, 616, 178
- Clarke, T. E., Blanton, E. L., & Sarazin, C. L. 2005, in X-Ray and Radio Connections (eds. L.O. Sjouwerman and K.K Dyer) Published electronically by NRAO, <http://www.aoc.nrao.edu/events/xrayradio> Held 3-6 February 2004 in Santa Fe, New Mexico, USA, (E7.08) 7 pages, ed. L. O. Sjouwerman & K. K. Dyer
- Clowe, D., Bradač, M., Gonzalez, A. H., Markevitch, M., Randall, S. W., Jones, C., & Zaritsky, D. 2006, ApJ, 648, L109
- Condon, J. J., Cotton, W. D., Greisen, E. W., Yin, Q. F., Perley, R. A., Taylor, G. B., & Broderick, J. J. 1998, AJ, 115, 1693
- Cowie, L. L., & Binney, J. 1977, ApJ, 215, 723
- Cowie, L. L., Songaila, A., Hu, E. M., & Cohen, J. G. 1996, AJ, 112, 839
- Crawford, C. S., Allen, S. W., Ebeling, H., Edge, A. C., & Fabian, A. C. 1999, MNRAS, 306, 857
- Crawford, C. S., Hatch, N. A., Fabian, A. C., & Sanders, J. S. 2005, MNRAS, 363, 216
- Croton, D. J., Springel, V., White, S. D. M., De Lucia, G., Frenk, C. S., Gao, L., Jenkins, A., Kauffmann, G., Navarro, J. F., & Yoshida, N. 2006, MNRAS, 365, 11
- Dalla Vecchia, C., Bower, R. G., Theuns, T., Balogh, M. L., Mazzotta, P., & Frenk, C. S. 2004, MNRAS, 355, 995
- David, L. P., Arnaud, K. A., Forman, W., & Jones, C. 1990, ApJ, 356, 32
- David, L. P., Jones, C., & Forman, W. 1996, ApJ, 473, 692
- David, L. P., & Kempner, J. 2004, ApJ, 613, 831

- Dickey, J. M., & Lockman, F. J. 1990, ARA&A, 28, 215
- Donahue, M., Horner, D. J., Cavagnolo, K. W., & Voit, G. M. 2006, ApJ, 643, 730
- Donahue, M., Mack, J., Voit, G. M., Sparks, W., Elston, R., & Maloney, P. R. 2000, ApJ, 545, 670
- Donahue, M., Stocke, J. T., & Gioia, I. M. 1992, ApJ, 385, 49
- Donahue, M., & Voit, G. M. 2004, in Clusters of Galaxies: Probes of Cosmological Structure and Galaxy Evolution, ed. J. S. Mulchaey, A. Dressler, & A. Oemler, 143–+
- Donahue, M., Voit, G. M., O'Dea, C. P., Baum, S. A., & Sparks, W. B. 2005, ApJ, 630, L13
- Donnelly, R. H., Markevitch, M., Forman, W., Jones, C., David, L. P., Churazov, E., & Gilfanov, M. 1998, ApJ, 500, 138
- Dunn, R. J. H., & Fabian, A. C. 2008, MNRAS, 385, 757
- Ebeling, H., Edge, A. C., Allen, S. W., Crawford, C. S., Fabian, A. C., & Huchra, J. P. 2000, MNRAS, 318, 333
- Ebeling, H., Edge, A. C., Boehringer, H., Allen, S. W., Crawford, C. S., Fabian, A. C., Voges, W., & Huchra, J. P. 1998, MNRAS, 301, 881
- Ebeling, H., Edge, A. C., & Henry, J. P. 2001, ApJ, 553, 668
- Edge, A. C., & Frayer, D. T. 2003, ApJ, 594, L13
- Edge, A. C., & Stewart, G. C. 1991, MNRAS, 252, 414
- Edge, A. C., Stewart, G. C., & Fabian, A. C. 1992, MNRAS, 258, 177
- Edge, A. C., Stewart, G. C., Fabian, A. C., & Arnaud, K. A. 1990, MNRAS, 245, 559
- Eisenstein, D. J., Zehavi, I., Hogg, D. W., Scoccimarro, R., Blanton, M. R., Nichol, R. C., Scranton, R., Seo, H.-J., Tegmark, M., Zheng, Z., Anderson, S. F., Annis, J., Bahcall, N., Brinkmann, J., Burles, S., Castander, F. J., Connolly, A., Csabai, I., Doi, M., Fukugita, M., Frieman, J. A., Glazebrook, K., Gunn, J. E., Hendry, J. S., Hennessy, G., Ivezić, Z., Kent, S., Knapp, G. R., Lin, H., Loh, Y.-S., Lupton, R. H., Margon, B., McKay, T. A., Meiksin, A., Munn, J. A., Pope, A., Richmond, M. W., Schlegel, D., Schneider, D. P., Shimasaku, K., Stoughton, C., Strauss, M. A., SubbaRao, M., Szalay, A. S., Szapudi, I., Tucker, D. L., Yanny, B., & York, D. G. 2005, ApJ, 633, 560
- Eke, V. R., Navarro, J. F., & Frenk, C. S. 1998, ApJ, 503, 569
- Ettori, S. 2000, MNRAS, 311, 313

- Evraud, A. E. 1989, ApJ, 341, L71
- . 1990, ApJ, 363, 349
- . 1997, MNRAS, 292, 289
- Evraud, A. E., & Henry, J. P. 1991, ApJ, 383, 95
- Evraud, A. E., Metzler, C. A., & Navarro, J. F. 1996, ApJ, 469, 494
- Fabian, A. C. 1994, ARA&A, 32, 277
- Fabian, A. C., Allen, S. W., Crawford, C. S., Johnstone, R. M., Morris, R. G., Sanders, J. S., & Schmidt, R. W. 2002, MNRAS, 332, L50
- Fabian, A. C., & Nulsen, P. E. J. 1977, MNRAS, 180, 479
- Fabian, A. C., Nulsen, P. E. J., & Canizares, C. R. 1984, Nature, 310, 733
- Falcke, H., Rieke, M. J., Rieke, G. H., Simpson, C., & Wilson, A. S. 1998, ApJ, 494, L155+
- Feretti, L., Boehringer, H., Giovannini, G., & Neumann, D. 1997a, A&A, 317, 432
- Feretti, L., Giovannini, G., & Boehringer, H. 1997b, New Astronomy, 2, 501
- Ferland, G. J., Fabian, A. C., Hatch, N. A., Johnstone, R. M., Porter, R. L., van Hoof, P. A. M., & Williams, R. J. R. 2008, MNRAS, 386, L72
- Finoguenov, A., Reiprich, T. H., & Böhringer, H. 2001, A&A, 368, 749
- Freeman, P. E., Kashyap, V., Rosner, R., & Lamb, D. Q. 2002, ApJS, 138, 185
- Frenk, C. S., White, S. D. M., Bode, P., Bond, J. R., Bryan, G. L., Cen, R., Couchman, H. M. P., Evrard, A. E., Gnedin, N., Jenkins, A., Khokhlov, A. M., Klypin, A., Navarro, J. F., Norman, M. L., Ostriker, J. P., Owen, J. M., Pearce, F. R., Pen, U.-L., Steinmetz, M., Thomas, P. A., Villumsen, J. V., Wadsley, J. W., Warren, M. S., Xu, G., & Yepes, G. 1999, ApJ, 525, 554
- Fukazawa, Y., Makishima, K., Tamura, T., Ezawa, H., Xu, H., Ikebe, Y., Kikuchi, K., & Ohashi, T. 1998, PASJ, 50, 187
- Gioia, I. M., Maccacaro, T., Schild, R. E., Wolter, A., Stocke, J. T., Morris, S. L., & Henry, J. P. 1990, ApJS, 72, 567
- Guo, F., Oh, S. P., & Ruszkowski, M. 2008, ArXiv e-prints, arxiv:0804.3823
- Gursky, H., Kellogg, E., Murray, S., Leong, C., Tananbaum, H., & Giacconi, R. 1971, ApJ, 167, L81+
- Haiman, Z., Mohr, J. J., & Holder, G. P. 2001, ApJ, 553, 545

- Hallman, E. J., Burns, J. O., Motl, P. M., & Norman, M. L. 2007, ApJ, 665, 911
- Hardcastle, M. J., Evans, D. A., & Croston, J. H. 2007, MNRAS, 376, 1849
- Heckman, T. M., Baum, S. A., van Breugel, W. J. M., & McCarthy, P. 1989, ApJ, 338, 48
- Henry, J. P., Mullis, C. R., Voges, W., Böhringer, H., Briel, U. G., Gioia, I. M., & Huchra, J. P. 2006, ApJS, 162, 304
- Hoeft, M., & Brüggen, M. 2004, ApJ, 617, 896
- Horner, D. J. 2001, PhD thesis, University of Maryland College Park
- Horner, D. J., Mushotzky, R. F., & Scharf, C. A. 1999, ApJ, 520, 78
- Hu, E. M., Cowie, L. L., & Wang, Z. 1985, ApJS, 59, 447
- Hudson, D. S., & Reiprich, T. H. 2007, in Heating versus Cooling in Galaxies and Clusters of Galaxies, ed. H. Böhringer, G. W. Pratt, A. Finoguenov, & P. Schuecker, 42–
- Hudson, D. S., Reiprich, T. H., Clarke, T. E., & Sarazin, C. L. 2006, A&A, 453, 433
- Jaffe, W., & Bremer, M. N. 1997, MNRAS, 284, L1
- Jeltema, T. E., Canizares, C. R., Bautz, M. W., & Buote, D. A. 2005, ApJ, 624, 606
- Jeltema, T. E., Hallman, E. J., Burns, J. O., & Motl, P. M. 2007, ArXiv e-prints, 708
- Johnstone, R. M., Fabian, A. C., & Nulsen, P. E. J. 1987, MNRAS, 224, 75
- Jones, C., & Forman, W. 1984, ApJ, 276, 38
- Kaastra, J. S., Tamura, T., Peterson, J. R., Bleeker, J. A. M., Ferrigno, C., Kahn, S. M., Paerels, F. B. S., Piffaretti, R., Branduardi-Raymont, G., & Böhringer, H. 2004, A&A, 413, 415
- Kaiser, N. 1986, MNRAS, 222, 323
- . 1991, ApJ, 383, 104
- Kalberla, P. M. W., Burton, W. B., Hartmann, D., Arnal, E. M., Bajaja, E., Morras, R., & Pöppel, W. G. L. 2005, A&A, 440, 775
- Kennicutt, Jr., R. C. 1983, ApJ, 272, 54
- Kravtsov, A. V., Vikhlinin, A., & Nagai, D. 2006, ApJ, 650, 128
- Kriss, G. A., Cioffi, D. F., & Canizares, C. R. 1983, ApJ, 272, 439

- Lawrence, C. R., Zucker, J. R., Readhead, A. C. S., Unwin, S. C., Pearson, T. J., & Xu, W. 1996, ApJS, 107, 541
- Liedahl, D. A., Osterheld, A. L., & Goldstein, W. H. 1995, ApJ, 438, L115
- Lloyd-Davies, E. J., Ponman, T. J., & Cannon, D. B. 2000, MNRAS, 315, 689
- Loewenstein, M. 2000, ApJ, 532, 17
- Looken, C., Norman, M. L., Nelson, E., Burns, J., Bryan, G. L., & Motl, P. 2002, ApJ, 579, 571
- Madau, P., Ferguson, H. C., Dickinson, M. E., Giavalisco, M., Steidel, C. C., & Fruchter, A. 1996, MNRAS, 283, 1388
- Markevitch, M. 1998, ApJ, 504, 27
- Markevitch, M., Forman, W. R., Sarazin, C. L., & Vikhlinin, A. 1998, ApJ, 503, 77
- Markevitch, M., Gonzalez, A. H., David, L., Vikhlinin, A., Murray, S., Forman, W., Jones, C., & Tucker, W. 2002, ApJ, 567, L27
- Markevitch, M., & Vikhlinin, A. 2007, Phys. Rep., 443, 1
- Markevitch, M., Vikhlinin, A., & Mazzotta, P. 2001, ApJ, 562, L153
- Marshall, H. L., Tennant, A., Grant, C. E., Hitchcock, A. P., O'Dell, S. L., & Plucinsky, P. P. 2004, in Presented at the Society of Photo-Optical Instrumentation Engineers (SPIE) Conference, Vol. 5165, X-Ray and Gamma-Ray Instrumentation for Astronomy XIII. Edited by Flanagan, Kathryn A.; Siegmund, Oswald H. W. Proceedings of the SPIE, Volume 5165, pp. 497-508 (2004)., ed. K. A. Flanagan & O. H. W. Siegmund, 497–508
- Martini, P., Kelson, D. D., Mulchaey, J. S., & Athey, A. 2004, in Clusters of Galaxies: Probes of Cosmological Structure and Galaxy Evolution, ed. J. S. Mulchaey, A. Dressler, & A. Oemler
- Mathews, W. G., & Bregman, J. N. 1978, ApJ, 224, 308
- Mathews, W. G., Faltenbacher, A., & Brighenti, F. 2006, ApJ, 638, 659
- Mathiesen, B. F., & Evrard, A. E. 2001, ApJ, 546, 100
- Mauch, T., Murphy, T., Buttery, H. J., Curran, J., Hunstead, R. W., Piestrzynski, B., Robertson, J. G., & Sadler, E. M. 2003, MNRAS, 342, 1117
- Maughan, B. J. 2007, ApJ, 668, 772
- Maughan, B. J., Jones, C., Forman, W., & Van Speybroeck, L. 2008, ApJS, 174, 117
- Maughan, B. J., Jones, C., Jones, L. R., & Van Speybroeck, L. 2007, ApJ, 659, 1125

- Mazzotta, P., Rasia, E., Moscardini, L., & Tormen, G. 2004, MNRAS, 354, 10
- McCarthy, I. G., Babul, A., Bower, R. G., & Balogh, M. L. 2008, MNRAS, 386, 1309
- McCarthy, I. G., Balogh, M. L., Babul, A., Poole, G. B., & Horner, D. J. 2004, ApJ, 613, 811
- McCarthy, I. G., Bower, R. G., Balogh, M. L., Voit, G. M., Pearce, F. R., Theuns, T., Babul, A., Lacey, C. G., & Frenk, C. S. 2007, MNRAS, 376, 497
- McDonough, W., & Braungart, M. 2002, Cradle to Cradle: Remaking the Way We Make Things (New York: North Point Press)
- McNamara, B. R., & Jaffe, W. 1994, A&A, 281, 673
- McNamara, B. R., & Nulsen, P. E. J. 2007, ARA&A, 45, 117
- McNamara, B. R., & O'Connell, R. W. 1989, AJ, 98, 2018
- McNamara, B. R., O'Connell, R. W., & Bregman, J. N. 1990, ApJ, 360, 20
- Mewe, R., Gronenschild, E. H. B. M., & van den Oord, G. H. J. 1985, A&AS, 62, 197
- Mewe, R., Lemen, J. R., & van den Oord, G. H. J. 1986, A&AS, 65, 511
- Mitchell, R. J., Culhane, J. L., Davison, P. J. N., & Ives, J. C. 1976, MNRAS, 175, 29P
- Mohr, J. J., & Evrard, A. E. 1997, ApJ, 491, 38
- Mohr, J. J., Mathiesen, B., & Evrard, A. E. 1999, ApJ, 517, 627
- Molendi, S., de Grandi, S., Fusco-Femiano, R., Colafrancesco, S., Fiore, F., Nesci, R., & Tamburelli, F. 1999, ApJ, 525, L73
- Morandi, A., & Ettori, S. 2007, MNRAS, 380, 1521
- Morrison, R., & McCammon, D. 1983, ApJ, 270, 119
- Mushotzky, R. F. 1984, Physica Scripta Volume T, 7, 157
- Mushotzky, R. F., & Loewenstein, M. 1997, ApJ, 481, L63+
- Nagai, D., Kravtsov, A. V., & Vikhlinin, A. 2007, ApJ, 668, 1
- Nath, B. B., & Roychowdhury, S. 2002, MNRAS, 333, 145
- Navarro, J. F., Frenk, C. S., & White, S. D. M. 1995, MNRAS, 275, 720
- . 1997, ApJ, 490, 493
- Nevalainen, J., Markevitch, M., & Forman, W. 2000, ApJ, 536, 73

- Nousek, J. A., & Shue, D. R. 1989, ApJ, 342, 1207
- O'Dea, C. P., Baum, S. A., & Gallimore, J. F. 1994a, ApJ, 436, 669
- O'Dea, C. P., Baum, S. A., Maloney, P. R., Tacconi, L. J., & Sparks, W. B. 1994b, ApJ, 422, 467
- O'Hara, T. B., Mohr, J. J., Bialek, J. J., & Evrard, A. E. 2006, ApJ, 639, 64
- O'Hara, T. B., Mohr, J. J., & Guerrero, M. A. 2004, ApJ, 604, 604
- Omma, H., Binney, J., Bryan, G., & Slyz, A. 2004, MNRAS, 348, 1105
- Ota, N., Kitayama, T., Masai, K., & Mitsuda, K. 2006, ApJ, 640, 673
- Parrish, I. J., & Quataert, E. 2008, ApJ, 677, L9
- Peres, C. B., Fabian, A. C., Edge, A. C., Allen, S. W., Johnstone, R. M., & White, D. A. 1998, MNRAS, 298, 416
- Perlmutter, S., Aldering, G., Goldhaber, G., Knop, R. A., Nugent, P., Castro, P. G., Deustua, S., Fabbro, S., Goobar, A., Groom, D. E., Hook, I. M., Kim, A. G., Kim, M. Y., Lee, J. C., Nunes, N. J., Pain, R., Pennypacker, C. R., Quimby, R., Lidman, C., Ellis, R. S., Irwin, M., McMahon, R. G., Ruiz-Lapuente, P., Walton, N., Schaefer, B., Boyle, B. J., Filippenko, A. V., Matheson, T., Fruchter, A. S., Panagia, N., Newberg, H. J. M., Couch, W. J., & The Supernova Cosmology Project. 1999, ApJ, 517, 565
- Peterson, J. R., & Fabian, A. C. 2006, Phys. Rep., 427, 1
- Peterson, J. R., Kahn, S. M., Paerels, F. B. S., Kaastra, J. S., Tamura, T., Bleeker, J. A. M., Ferrigno, C., & Jernigan, J. G. 2003, ApJ, 590, 207
- Peterson, J. R., Paerels, F. B. S., Kaastra, J. S., Arnaud, M., Reiprich, T. H., Fabian, A. C., Mushotzky, R. F., Jernigan, J. G., & Sakelliou, I. 2001, A&A, 365, L104
- Piffaretti, R., Jetzer, P., Kaastra, J. S., & Tamura, T. 2005, A&A, 433, 101
- Pizzolato, F., & Soker, N. 2005, ApJ, 632, 821
- Ponman, T. J., Cannon, D. B., & Navarro, J. F. 1999, Nature, 397, 135
- Ponman, T. J., Sanderson, A. J. R., & Finoguenov, A. 2003, MNRAS, 343, 331
- Poole, G. B., Fardal, M. A., Babul, A., McCarthy, I. G., Quinn, T., & Wadsley, J. 2006, MNRAS, 373, 881
- Pratt, G. W., Arnaud, M., & Pointecouteau, E. 2006, A&A, 446, 429
- Prestwich, A. H., & Joy, M. 1991, ApJ, 369, L1
- Quataert, E. 2008, ApJ, 673, 758

- Quillen, A. C., Zufelt, N., Park, J., O'Dea, C. P., Baum, S. A., Privon, G., Noel-Storr, J., Edge, A., Russell, H., Fabian, A., Donahue, M., Bregman, J. N., McNamara, B. R., & Sarazin, C. L. 2008, ApJS, 176, 39
- Rafferty, D., McNamara, B., & Nulsen, P. 2008, ArXiv e-prints, arxiv:0802.1864
- Randall, S. W., Sarazin, C. L., & Ricker, P. M. 2002, ApJ, 577, 579
- Reiprich, T. H. 2001, PhD thesis, AA(Max-Planck-Institut für extraterrestrische Physik, P.O. Box 1312, 85741 Garching, Germany)
- Reiprich, T. H., & Böhringer, H. 2002, ApJ, 567, 716
- Riess, A. G., Filippenko, A. V., Challis, P., Clocchiatti, A., Diercks, A., Garnavich, P. M., Gilliland, R. L., Hogan, C. J., Jha, S., Kirshner, R. P., Leibundgut, B., Phillips, M. M., Reiss, D., Schmidt, B. P., Schommer, R. A., Smith, R. C., Spyromilio, J., Stubbs, C., Suntzeff, N. B., & Tonry, J. 1998, AJ, 116, 1009
- Riess, A. G., Strolger, L.-G., Casertano, S., Ferguson, H. C., Mobasher, B., Gold, B., Challis, P. J., Filippenko, A. V., Jha, S., Li, W., Tonry, J., Foley, R., Kirshner, R. P., Dickinson, M., MacDonald, E., Eisenstein, D., Livio, M., Younger, J., Xu, C., Dahlén, T., & Stern, D. 2007, ApJ, 659, 98
- Rosati, P., della Ceca, R., Burg, R., Norman, C., & Giacconi, R. 1995, ApJ, 445, L11
- Roychowdhury, S., Ruszkowski, M., Nath, B. B., & Begelman, M. C. 2004, ApJ, 615, 681
- Ruszkowski, M., & Begelman, M. C. 2002, ApJ, 581, 223
- Ruszkowski, M., Enßlin, T. A., Brüggen, M., Begelman, M. C., & Churazov, E. 2008, MNRAS, 383, 1359
- Rybicki, G. B., & Lightman, A. P. 1986, Radiative Processes in Astrophysics (Radiative Processes in Astrophysics, by George B. Rybicki, Alan P. Lightman, pp. 400. ISBN 0-471-82759-2. Wiley-VCH, June 1986.)
- Sakelliou, I., & Merrifield, M. R. 2000, MNRAS, 311, 649
- Sakelliou, I., & Ponman, T. J. 2004, MNRAS, 351, 1439
- Sanderson, A. J. R., Ponman, T. J., & O'Sullivan, E. 2006, MNRAS, 372, 1496
- Sarazin, C. L. 1986, Reviews of Modern Physics, 58, 1
- Sarazin, C. L. 2003, Physics of Plasmas, 10, 1992
- Saro, A., Borgani, S., Tornatore, L., Dolag, K., Murante, G., Biviano, A., Calura, F., & Charlot, S. 2006, MNRAS, 373, 397

- Serlemitsos, P. J., Smith, B. W., Boldt, E. A., Holt, S. S., & Swank, J. H. 1977, ApJ, 211, L63
- Sharma, M., McNamara, B. R., Nulsen, P. E. J., Owers, M., Wise, M. W., Blanton, E. L., Sarazin, C. L., Owen, F. N., & David, L. P. 2004, ApJ, 613, 180
- Shaver, P. A., Wall, J. V., Kellermann, K. I., Jackson, C. A., & Hawkins, M. R. S. 1996, Nature, 384, 439
- Snowden, S. L. 2004, in Astrophysics and Space Science Library, Vol. 309, Soft X-ray Emission from Clusters of Galaxies and Related Phenomena, ed. R. M. J. Lieu, 103–+
- Snowden, S. L., Mushotzky, R. F., Kuntz, K. D., & Davis, D. S. 2008, A&A, 478, 615
- Soker, N., & Pizzolato, F. 2005, ApJ, 622, 847
- Sparks, W. B., Donahue, M., Jordán, A., Ferrarese, L., & Côté, P. 2004, ApJ, 607, 294
- Spergel, D. N., Bean, R., Doré, O., Nolta, M. R., Bennett, C. L., Dunkley, J., Hinshaw, G., Jarosik, N., Komatsu, E., Page, L., Peiris, H. V., Verde, L., Halpern, M., Hill, R. S., Kogut, A., Limon, M., Meyer, S. S., Odegard, N., Tucker, G. S., Weiland, J. L., Wollack, E., & Wright, E. L. 2007, ApJS, 170, 377
- Stewart, G. C., Fabian, A. C., Jones, C., & Forman, W. 1984, ApJ, 285, 1
- Sun, M., Jones, C., Forman, W., Vikhlinin, A., Donahue, M., & Voit, M. 2007, ApJ, 657, 197
- Sun, M., & Murray, S. S. 2002, ApJ, 576, 708
- Sun, M., Voit, G. M., Donahue, M., Jones, C., & Forman, W. 2008, ArXiv e-prints, arxiv:0805.2320
- Tamura, T., Kaastra, J. S., Peterson, J. R., Paerels, F. B. S., Mittaz, J. P. D., Trudolyubov, S. P., Stewart, G., Fabian, A. C., Mushotzky, R. F., Lumb, D. H., & Ikebe, Y. 2001, A&A, 365, L87
- Teyssier, R., Chieze, J.-P., & Alimi, J.-M. 1997, ApJ, 480, 36
- Townsley, L. K., Broos, P. S., Garmire, G. P., & Nousek, J. A. 2000, ApJ, 534, L139
- Tozzi, P., & Norman, C. 2001, ApJ, 546, 63
- Valentijn, E. A., & Bijleveld, W. 1983, A&A, 125, 223
- Valluri, M., & Anupama, G. C. 1996, AJ, 112, 1390

- Ventimiglia, D. A., Voit, G. M., Donahue, M., & Ameglio, S. 2008, ArXiv e-prints, arxiv:0806.0850
- Vikhlinin, A. 2006, ApJ, 640, 710
- Vikhlinin, A., Markevitch, M., Murray, S. S., Jones, C., Forman, W., & Van Speybroeck, L. 2005, ApJ, 628, 655
- Vikhlinin, A., McNamara, B. R., Forman, W., Jones, C., Quintana, H., & Hornstrup, A. 1998, ApJ, 502, 558
- Voit, G. M. 2005, Reviews of Modern Physics, 77, 207
- Voit, G. M., & Bryan, G. L. 2001, Nature, 414, 425
- Voit, G. M., Bryan, G. L., Balogh, M. L., & Bower, R. G. 2002, ApJ, 576, 601
- Voit, G. M., Cavagnolo, K. W., Donahue, M., Rafferty, D. A., McNamara, B. R., & Nulsen, P. E. J. 2008, ApJ, 681, L5
- Voit, G. M., & Donahue, M. 1995, ApJ, 452, 164
- . 1997, ApJ, 486, 242
- . 2005, ApJ, 634, 955
- Wang, L., & Steinhardt, P. J. 1998, ApJ, 508, 483
- Wang, Q. D., Connolly, A., & Brunner, R. 1997, ApJ, 487, L13+
- Wang, Q. D., Owen, F., & Ledlow, M. 2004a, ApJ, 611, 821
- Wang, S., Khouri, J., Haiman, Z., & May, M. 2004b, Phys. Rev. D, 70, 123008
- Wargelin, B. J., Markevitch, M., Juda, M., Kharchenko, V., Edgar, R., & Dalgarno, A. 2004, ApJ, 607, 596
- Waters, C. Z., Zepf, S. E., Lauer, T. R., & Baltz, E. A. 2008, Submitted to ApJ
- Weisskopf, M. C., Tananbaum, H. D., Van Speybroeck, L. P., & O'Dell, S. L. 2000, in Presented at the Society of Photo-Optical Instrumentation Engineers (SPIE) Conference, Vol. 4012, Proc. SPIE Vol. 4012, p. 2-16, X-Ray Optics, Instruments, and Missions III, Joachim E. Truemper; Bernd Aschenbach; Eds., ed. J. E. Truemper & B. Aschenbach, 2–16
- White, D. A., Jones, C., & Forman, W. 1997, MNRAS, 292, 419
- White, S. D. M., Efstathiou, G., & Frenk, C. S. 1993, MNRAS, 262, 1023
- White, S. D. M., & Rees, M. J. 1978, MNRAS, 183, 341
- Xue, Y.-J., & Wu, X.-P. 2000, MNRAS, 318, 715